UNIVERSITY OF CALIFORNIA SAN DIEGO

Strain Engineering of two dimensional materials by Scanning Tunneling Microscopy

A dissertation submitted in partial satisfaction of the
requirements for the degree
Doctor of Philosophy

in

Engineering Sciences (Mechanical Engineering)

by

Nirjhar Sarkar

Committee in charge:

Professor Prabhakar R. Bandaru, Chair
Professor Robert C. Dynes, Co-Chair
Professor Shane Cybart
Professor Javier Garay
Professor Vitali Nesterenko

2021

The dissertation of Nirjhar Sarkar is approved, and it is acceptable in quality and form for publication on microfilm and electronically.

University of California San Diego

2021

DEDICATION

In loving memory of Diya and Eva

who wanted me to be a geologist/archaeologist

which I did but on nanoscopic landforms.

EPIGRAPH

Anyone who thinks my story is anywhere near over is sadly mistaken.

— Donald Trump

TABLE OF CONTENTS

LIST OF ABBREVIATIONS

2D Two dimensional.

CNTs Carbon Nanotubes.

dI/dV Differential Conductance.

DW Domain Wall.

FWHM Full Width Half Maximum.

GB Grain Boundary.

HoPG Highly Oriented Pyrolitic Graphite.

LDoS Local Density of States.

MoS_2 Molybdenum diselenide.

mV milli volts.

$NbSe_2$ Niobium diselenide.

SLG Single Layer Graphene.

STM Scanning Tunneling Microscopy.

TEM Transmission electron microscopy.

VDW Van der Waals.

LIST OF SYMBOLS

θ	Twist angle of the graphene grains
I_{tip}	Tunneling current
V_{sample}	Sample bias

LIST OF FIGURES

ACKNOWLEDGEMENTS

I would like to express my gratitude to the tunneling current equation that makes Scanning Tunneling Microscopy (STM) an eye of god. One can develop skills to setup noiseless experiments but the talent lies in choosing a scientific idea worth pursuing (which in this case is the use of exponential tunneling current equation to image atoms).

I would like to acknowledge my advisor Prof. Prabhakar R. Bandaru who took a leap of faith in picking my profile for the graduate research program and identified my talent in experimental science (like graphene synthesis and device electronics) before even I knew about it. It is through his ability of forming positive social connections that I got to work with Prof. Robert C. Dynes on experimental condensed matter physics and low temperature STM.

I would like to acknowledge Bob for all the work he taught me starting from plumbing, wire-bonding, electrical measurements, scientific criticism, car repairs, etc to name a few. I appreciate every laugh and tear we shared everyday along with the scientific interactions which is when I learned the most and gained confidence during my PhD.

I am specially grateful with the funding awarded throughout my PhD program from the funding agencies like Air force and Multi-campus UC research from Prof.Shane Cybart and Prof. Robert C. Dynes who recognized the need of financial relief in form of Graduate Student Researcher (GSR) necessary for better research performance. In other words, I never had to do Teaching assistantship (TA).

I would like to acknowledge Erick Martinez Loran and my postdoc Uday Goteti for being restless mind, always open to discuss and do research; Michael Rezin from physics electronic shop, whose contribution in STM electronics repair has been catalytic to the project; all Bandaru

Lab members: Hidenori Yamada, Anna Alexander, Serdar Yavuz, Fatih Canbazoglu, Abhishek Sathisha, Peng Chen, Bei Fan, Yun Zhao, Zichen Zhang, Shreyam Natani, Yongliang Dong, Kassra Eshraghi, Li Cheng, Raivat, Alex, Kesong, Sanjana, Raghuram for their thoughtful insights during group meeting presentations.

I would also like to thank all my PhD colleagues: Priyank, Achal, Ishita, Shivam, Abhijit, Vicky, Sridip, Ahanjit, Brato, Shouvik, Rourav, Soumen that has made this enterprise possible and joyful. Thank you Ian, Nitin, Sarthak, Abhishek, Chetan, Aamodh, Lorraine and Louie.

Finally, I would like to thank my parents who have supported me through all the stages of this journey. I was exposed to the world of research through Daniel and BVR Chowdhuri from NUS with the blessings of my grand uncle Kamal and help of my father and his colleagues: Jay and Sudarshan.

Chapter 3, in part is currently being prepared for submission for publication of the material, under the title "Atomic scale strain engineering of layered sheets on the surfaces of two-dimensional materials" by Sarkar, Nirjhar; Bandaru, Prabhakar R. and Dynes, Robert C.. The dissertation author was the primary investigator and author of this paper.

Chapter 4, in part is currently being prepared for submission for publication of the material, under the title "Coherent Zigazag Grain Boundary in graphite" by Sarkar, Nirjhar; Bandaru, Prabhakar R. and Dynes, Robert C.. The dissertation author was the primary investigator and author of this paper.

VITA

2016	B. Tech in Mechanical Engineering, National Institute of Technology Durgapur
2021	Ph. D. in Engineering Sciences (Mechanical Engineering), University of California San Diego

PUBLICATIONS

1. **Sarkar, Nirjhar**, Dynes, Robert C., Prabhakar, Bandaru R.. "Atomic scale strain engineering of layered sheets on the surfaces of two-dimensional materials". (In preparation, 2021).
2. **Sarkar, Nirjhar**, Dynes, Robert C., Prabhakar, Bandaru R.. "Coherent Zigazag Grain Boundary in graphite". (In preparation, 2021).

ABSTRACT OF THE DISSERTATION

Strain Engineering of two dimensional materials by Scanning Tunneling Microscopy

by

Nirjhar Sarkar

Doctor of Philosophy in Engineering Sciences (Mechanical Engineering)

University of California San Diego, 2021

Professor Prabhakar R. Bandaru, Chair
Professor Robert C. Dynes, Co-Chair

Strain engineering on layered two dimensional materials has gained some interest for modulating device electronics. This is done by twisting layered materials, stretching flexible substrates or applying hydro-static pressures. Our work offers to the straintronics and twistronics community, a new pathway of deforming individual atoms on surface controllably by tip-induced forces and probe in-situ the mechanical and electronic properties on surface under strain which can be exploited for innumerable applications.

Tunneling gaps of interatomic distances can induce strain by individual atomic deformation

controllably and elastically with an STM tip and while under strain probe in-situ their mechanical VDW strength or elasticity and electronic band structure. Such capabilities can be exploited in force microscopy studies of soft matter, biological, chemical and physical sensors or 2D materials based semiconductor nanoelectronics. We demonstrate that various weak forces only at small tip-surface gaps become strong enough to deform surfaces of graphite, monolayer graphene, Niobium diselenide and their step heights that reveals their dependence on their structural anisotropy. Additionally we provide an application to our tip-induced deformative approach by locally deforming moiré patterns (partly shown in following figure) which not only reveals their mechanical properties like interlayer VDWs strength of different moiré domains (including the domain walls) but also exhibits flattening of moire flat bands under strain.

The flat bands aspect have helped understand the imaging issues of topologically protected grain boundaries. We reveal various experimental challenges and solutions to probing grain boundaries that have distinct spectroscopic states on their surfaces. They play a role in charging or discharging effects on the grain boundary sensed by the STM. The origin of the flat band states around zero bias has been shown to be caused by the zigzag edges and the other VHS states could be caused the distinct topological arrangement of non-hexagons.

Flat bands or VHS peaks also can be observed on moire patterns. We observe how mechanically the moire domains can be deformed and in-situ observe the deformation of electronic bands. Such band modulating approach by tip-induced forces have not been explored. We approach the strained moire patterns from the point of view of domain walls. Domain walls are confined 1D structures on 2D moire surfaces.

Chapter 1

Introduction

Our research contributes to the straintronics and twistronics community, a new pathway of deforming individual atoms on surface controllably by tip-induced forces and probe in-situ the mechanical and electronic properties on surface under strain which can be exploited for innumerable applications.

Recent years have observed unique properties emerge out of strain-induced nano materials like superconductivity or ferromagnetism in bilayer graphene by twisting or band-gap tunability in 2D heterostructures by lattice mismatch or high pressure superconductivity in sulphides under hydrostatic pressure or magnetoresistance in MoS_2 by substrate engineering. Our paper exhibits another way to induce strain by individual atomic deformation controllably and elastically with an STM tip and while under strain probe in-situ their mechanical VDW strength or elasticity and electronic band structure. Such capabilities can be exploited in force microscopy studies of soft matter, biological, chemical and physical sensors or 2D materials based semiconductor nanoelectronics. We demonstrate that various weak forces only at small tip-surface gaps become strong enough to deform surfaces of graphite, monolayer graphene, Niobium diselenide and their step heights that

reveals their dependence on their structural anisotropy in chapter 3.

In chapter 2, graphene synthesis and characterization is briefly discussed along with device electronics. The electronic mobility of the grown graphene samples is shown as well as the metal-insulator transition.

In chapter 3, our study also resolved a long standing debate on anomalous behaviour with STM tip-surface interaction noticed by H. Rohrer (co-inventor of STM) in 1986. Given the wide range of material surface properties characterized using nano probes in many laboratories and industrial settings, our experimental work uses atomically resolved topographic imaging to outline the need of a discerning eye when probing any 'soft' surface which can lead to anomalous results.

In chapter 4, the tip deformative approach is applied to the most common grain boundary naturally formed on graphene and graphite surface. These grain boundaries are not messy unbroken bonded edges but rather topologically protected by pentagons, septagons and octagons. They are coherent and periodic. The formation of such grain boundaries under high temperature environment implies they are designed to provide dispersion-less thermal and electron transport.

In chapter 5, we provide an application to our tip-induced deformative approach by locally deforming moiré patterns which reveals their mechanical properties like interlayer VDWs strength of different moiré domains (including the domain walls). It also exhibits flattening of moire flat electronic bands under strain.

1.1 What is tip-induced deformation?

Highly oriented pyrolytic graphite (HoPG) has been extensively used in STM related work as a calibration standard [1–3] for height determination over steps arising from a presumed atomic

flatness and surface cleanliness [4–6]. The observed steps, e.g., are presumed to arise from a difference in the elevation of graphene sheets on either side and would be distinguished ideally by multiples of 3.4 Å, corresponding to the layer-by-layer spacing of the sheets. However, previous STM measurements have indicated some confusion on the deduced step heights, arising from the possible lack of flatness of the graphene sheet. Such an attribute may arise from atomic corrugation yielding an enhancement of the measured amplitudes [7–9]. For instance, while the measured atomic amplitudes on graphite surface are expected to be 0.2A from Local Density of States (LDOS) calculations [10–13], abnormally high atomic amplitudes, of the order of up to 4Å were indicated[7–9]. Such anomalies have been attributed to the tip-surface interactions which may induce local elastic deformation of graphite surfaces particularly at small distances [7, 14]. While the oscillations follow the modeled LDOS based contours[13], extant models[10, 11, 13] of tip-sample interaction involving localized elastic deformation – based on a particular inter-atomic potential interaction model[7, 9, 11, 15–17] involving variable tip geometry, are inadequate to quantitatively account for the large magnitude.

However, large atomic corrugations could not be well explained through models related to electronic state variations[10–13] on graphitic surfaces but were attributed[7] to mechanical tip-induced surface deformations. Such local deformations could be conflated would be opposed[14] by sliding/shear between basal planes in the 2-D layered materials. To seek better understanding of such dual forces[14], we compare atomic topographies on surfaces of distinct materials and observe that the anomaly related to large atomic amplitudes exists only on graphite surface but is suppressed on single-layer graphene (SLG) and $NbSe_2$. This happens predominantly at small tip-sample gaps. Consequently, the graphite surface may be deformed more easily compared to surfaces of $NbSe_2$ and SLG and leads towards an explanation involving vdW bonding dictating

their surface properties. Most scanning microscopy techniques require the need of a calibration material having a constant atomic periodicity in all crystallographic direction. However, we show that one should be careful in using graphite or any other material for calibration in z scale. This has been showed in figure 1.2 that a same topographic height across the monatomic step height can be different as a function of tunneling current or gap distance. Various weak forces become stronger when the tip comes closer to the surface by gap distances close to bond lengths. This shows that at small gap distances, one can pull atoms out of plane as shown in figure 1.2 inset.

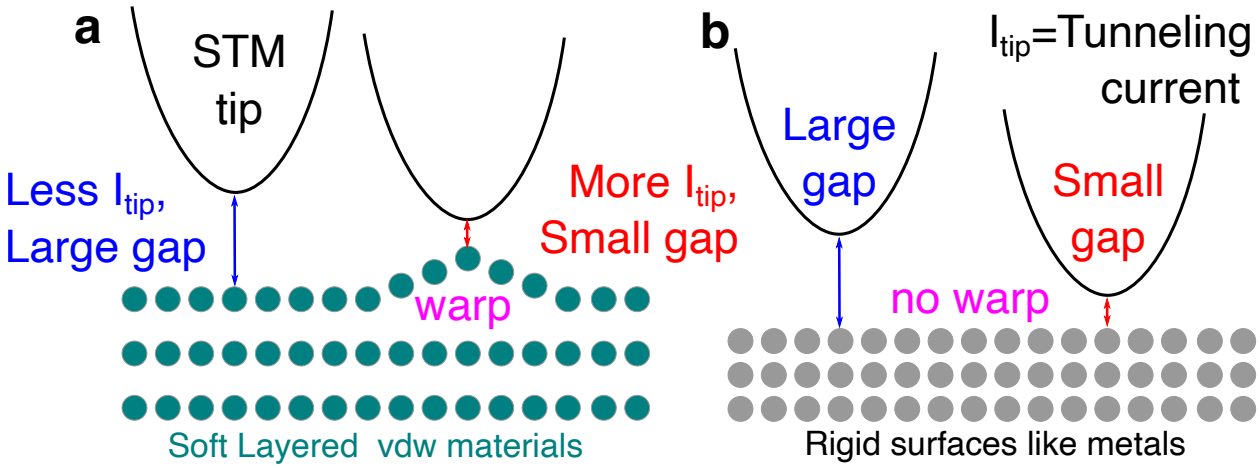

Figure 1.1: Schematic showing responses of rigid and soft materials to tip induced deformations only at smaller gaps (or higher tunneling currents).

We further comment on the elastic interactions of the tip on 'soft' vDW layered surfaces in contrast to rigid metal surfaces. Ideally in a standard constant current STM mode[18], the tip traces the potential contours over the rigid atomic surface without deforming it. However, as the graphite surface is soft, its surface may be more easily deformed. This is shown by expanding on the experimental atomic topography across the graphite monatomic step through the models in figure 1.2. In spite of the amplitude enhancement from 3 na to 30 nA, the difference of the baseline of the corrugated layers on either side of the step differs by a fixed and constant step height. The

topographic waveform at 30 nA appears as large as the step height.

Such large atomic corrugations cannot be explained purely based on electronic considerations alone but seem to imply considerable pulling outwards of the atoms. Such deformations (in fig. 1.2) occur predominantly at smaller gap distances with the hills (/valleys) corresponding to outward (/inward) atomic deformations.

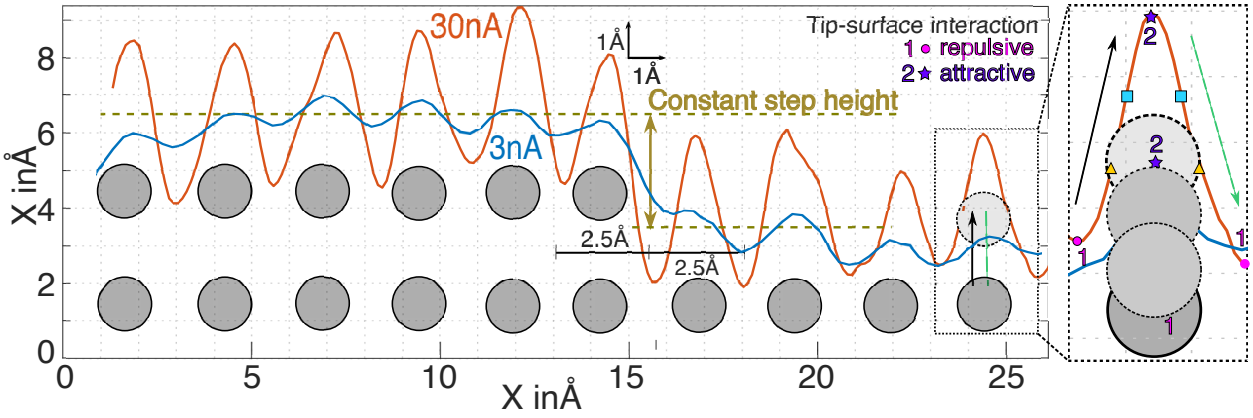

Figure 1.2: Schematic of plausible atomic topography across a monatomic step height (measured by the difference in mean of the two waveforms on either side of the step) enhanced at tunneling currents of 30 nA (red line) than at 3 nA (blue line), indicating anomalously high atomic corrugation amplitude. It is noted that the wavelength of 2.5Å and step height remains consistent at both currents. The right inset indicates the rationale for the anomaly through tip induced local deformation at an atom outwards and inwards related to attractive and repulsive tip-sample interactions. This allows for the indicated placement of the carbon atoms.

Following Soler's elastic theory [7], there is expected an attractive force interaction when the tip pulls the atom outwards (labeled 2 in fig. 1.2 inset) and a repulsive force interaction when the tip pushes the atom inwards into the bulk (at position 1). It has been suggested [7] that the inward atomic deformation into the bulk by the tip would be opposed by a stronger restoring repulsive force compared to the case of outward atomic deformation. The related difference was observed14 in terms of a preference towards stronger minima in the atomic topography of graphite

1.2 Edge states - Steps and Grain boundary

It's interesting to point out that studying 1-dimensional edges of a two dimensional surface reveals more information about the material. More information can be learned from the looking at these mono-atomic step edges closely.

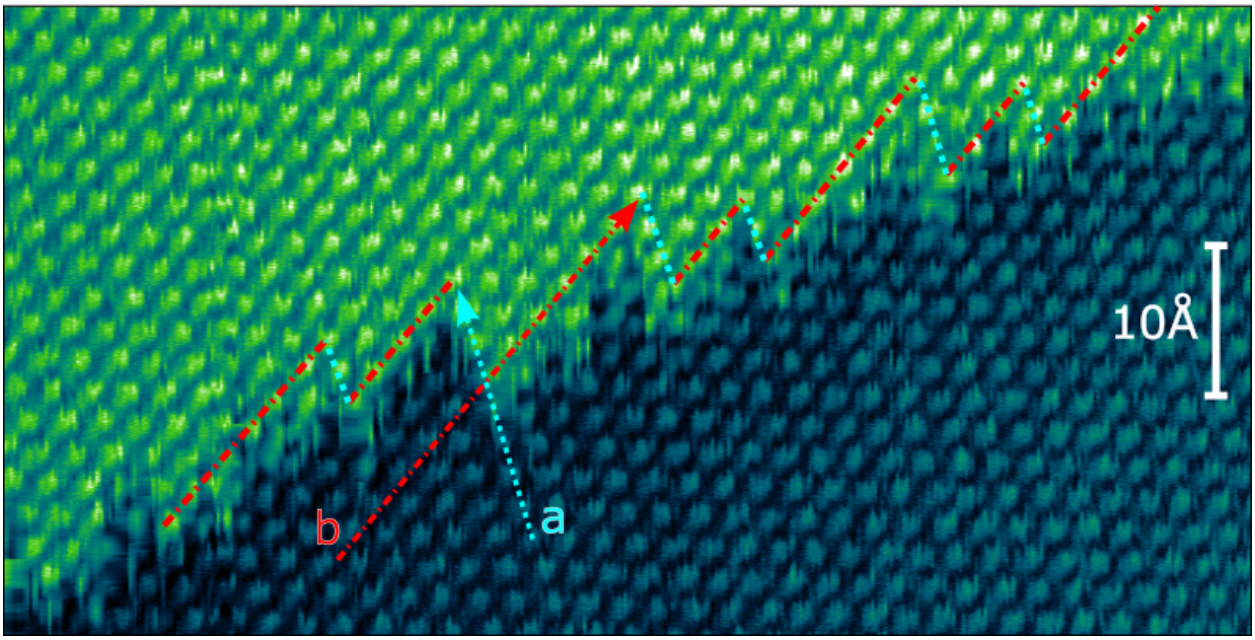

Figure 1.3: Atomically resolved topographic 2D image of the graphite monatomic step edge. Exfoliated graphite edges tear along crystal axes direction a (in blue) and b (in red) to create a sawtooth-like step edge of height 10Å or less.

On a micron scale, defects on exfoliated graphite surfaces (by STM or AFM observations) tend to follow straight lines for microns of lengths depending on grain size. However, on a nano scale monatomic graphite step edge (in fig. 1.3) looks torn up in a pattern resembling a sawtooth waveform. The sawtooth triangular edges follow the crystal axes direction b and a (shown by red and blue) but the step edge direction is along the vector sum of a and b which is the exfoliation direction labeled. Thin monatomic sheet of carbon with weak VDW under each sheet allows tearing of covalent bonds in a and/or b direction during exfoliation. When the exfoliation direction

is not along the crystal axis directions, more the number of bonds are broken along b than along a since the b vector is more closely aligned with the exfoliation direction.

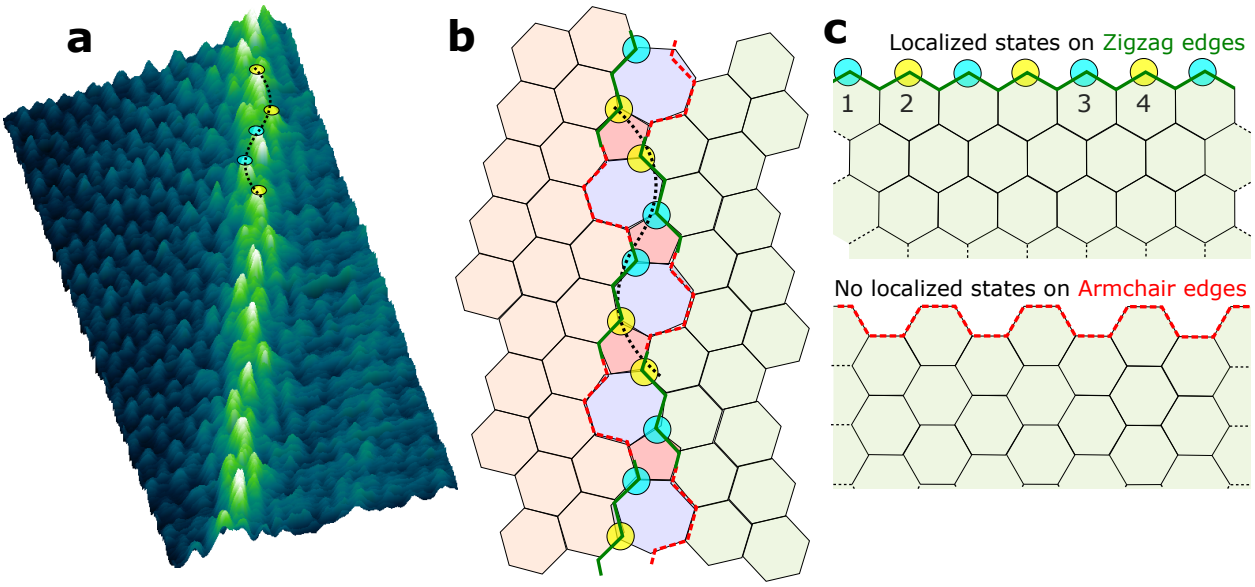

Figure 1.4: Stretching or compressing of domain walls on moire patterns with twist angles

Another approach towards understanding the localization of states on the grain boundary is by edge states. Previous experimentally verified[19] theoretical studies have shown the existence of denser localized states on zigzag edges than armchair edges as schematized in figure 1.4. The edges contributing to the (1,3) GB can be revealed by de-stitching the GB and it would exhibit that the left and right edges of every pentagon-heptagon pair is made up of alternating zigzag edges shown by green line (with localized states) and armchair edges shown by red line (with no localized states). On restitching the GB, the same zigzag pattern of localized states are obtained (that matches with LDoS simulated maps[19]).

1.3 Moiré

These weak forces between tip-surfaces that become strong enough at small gap distances to warp 'soft' graphite surfaces compared to rigid metal surfaces. Atomic corrugations can be explained by tip interaction with the surface interatomic potential[7] but the bulging of the nano-sized moiré domains could be caused partly by VDW interaction [20] between neutral bodies and partly by high electric fields pulling the surfaces out of plane to maintain a constant current.

Once the idea of tip-induced deformations is established, we can apply it to study the behaviour of several features on graphite surface. Since the deformations have a dependence on VDW bonding, the influence of vDW bonds in these layered anisotropic 2D materials in determining their atomic deformation amplitudes and distinct exfoliation patterns can be extended to the case where the layers are slightly out of registry with respect to each other.

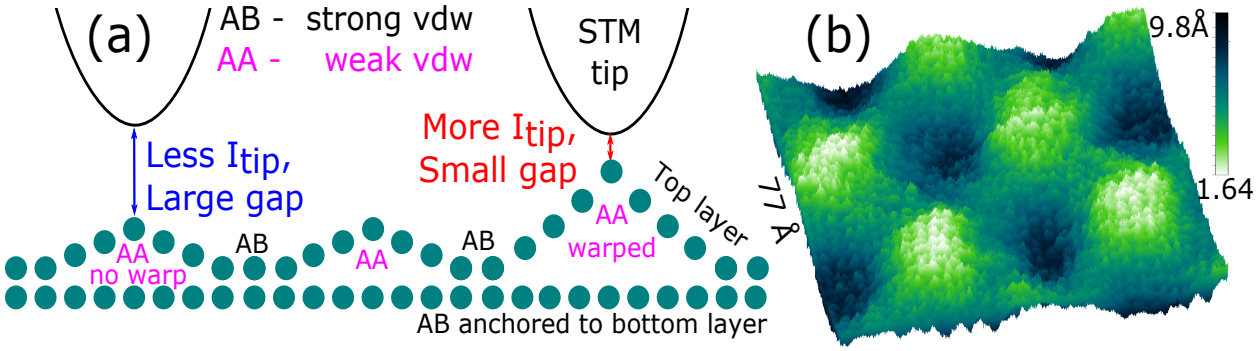

Figure 1.5: Deformation of moire patterns schematically and experimentally

We study how moire patterns commonly found on graphite surfaces respond to tip-induced deformations topographically and electronically. Moire patterns are an ideal platform for this study because a twist of the top monolayer with the underlying graphite creates a periodic pattern of

different domains with different inter-layer VDW/coupling strengths. This tests our VDW theory and allows us to deformations of other graphite features like steps, grain boundaries and moire patterns of different twist angles.

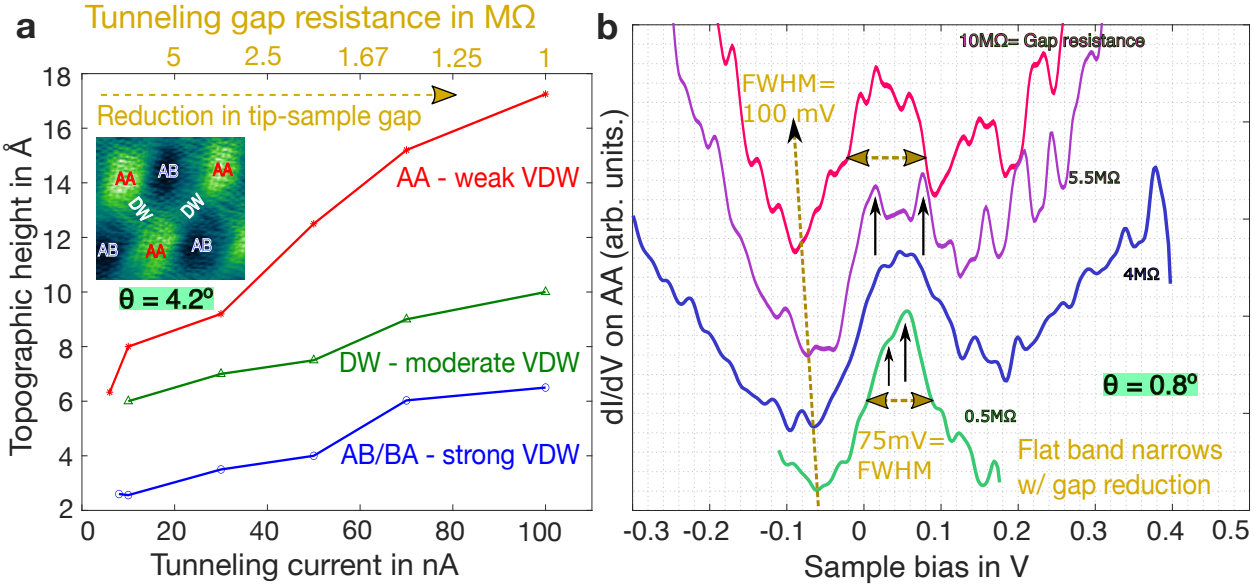

Figure 1.6: Deformation of moire domains mechanically and electronically

Deformation amplitudes of moire domains calculated in figure 1.6 shows that the weakly vDW-bonded AA domains get deformed easily than AB that is strongly anchored to its underlying layer while DW shows intermediate response as a function of tunneling current or gap resistance(from 1MΩ to 10 MΩ). dI/dV spectroscopy on AA domains of small 0.8 degree twist angle shows how the flat bands corresponding to zero bias peak become narrower as shown by their full width half maximum (FWHM) with the reduction in gap distance or gap resistance (from 0.5MΩ to 10 MΩ). Measurements are described in supplementary info. 3). Flatter bands corresponding to higher density of states induce stronger correlation effects which could be desirable in twistronics.

1.4 Domain walls

Moire patterns are created by putting the tip graphite layer on bottom bulk with different lattice orientations. When the two lattices are in orientational registry, there are still a number of ways in which the two layers can be arranged corresponding to different translations of the lattices. experimentation.

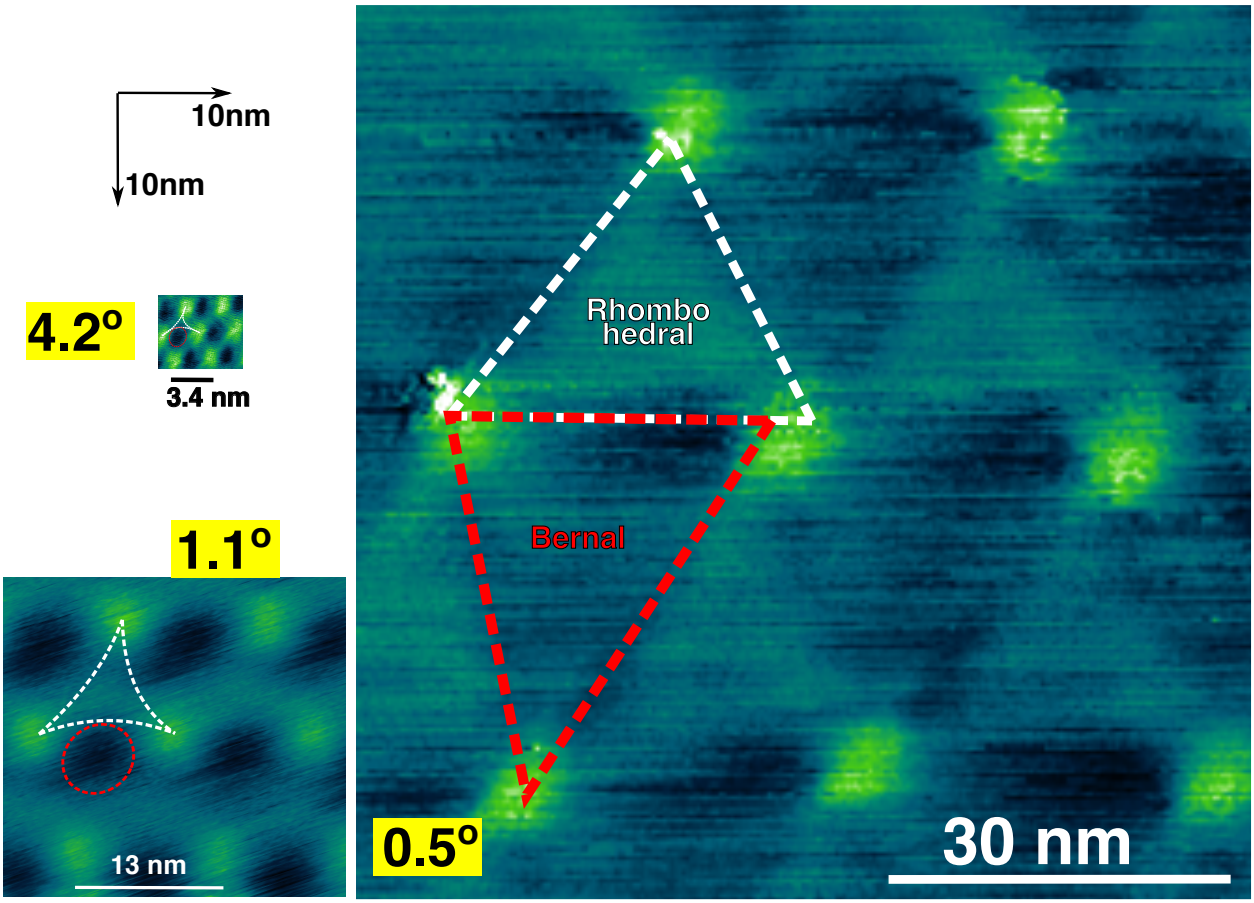

Figure 1.7: Relaxation and unrelaxation of domain walls with twist angle

The most energetically costly configuration is 'AA' stacking. 'Bernal' or 'AB/BA' stacking (Fig. 1.5) is the energetically preferred arrangement. Another intermediate favourable stacking

arrangement is rhomohedral stacking or 'CAB'. The interface of two Bernal regions is 'saddle point' stacking. The rotational misalignment of layers enforces the creation of a moiré super-lattice that necessarily contains each of the stacking domains in proportions that are related to the twist angle. Below a critical angle there is an energetic drive to form a moiré pattern that maximizes the energetically favourable Bernal stacking at the expense of AA sites through lattice reconstruction that leads to the creation of discrete stacking domains and domain walls. Being able to visualize the details of rotation angle, stacking domains and domain walls in a simple way would open up these structures to reproducible

1.5 Summary

We demonstrate that various weak forces only at small tip-surface gaps become strong enough to deform surfaces of graphite, mono-layer graphene, Niobium diselenide and their step heights that reveals their dependence on their structural anisotropy. Additionally we provide an application to our tip-induced deformative approach by locally deforming moiré patterns which not only reveals their mechanical properties like inter-layer vDWs strength of different moiré domains (including the domain walls) but also exhibits flattening of moire flat bands under strain.

All images in this dissertation has been taken at room temperature and ambient conditions. Multiple noise sources has been elminated like parasitic coupling between tip and high voltage piezo, better insulation and coaxial cable replacement, cutting off a ground loop connection from the pulley, cleaning of oxides or old solder connections in pre-amplifier, removal of pumping lines because of being identified as the major source of low frequency noises, etc. To showcase the sensitivity of the home built STM to external noises, an image map of the graphite sheet has been

taken with noisy scans arising from me and Bob talking about Donald Trump.

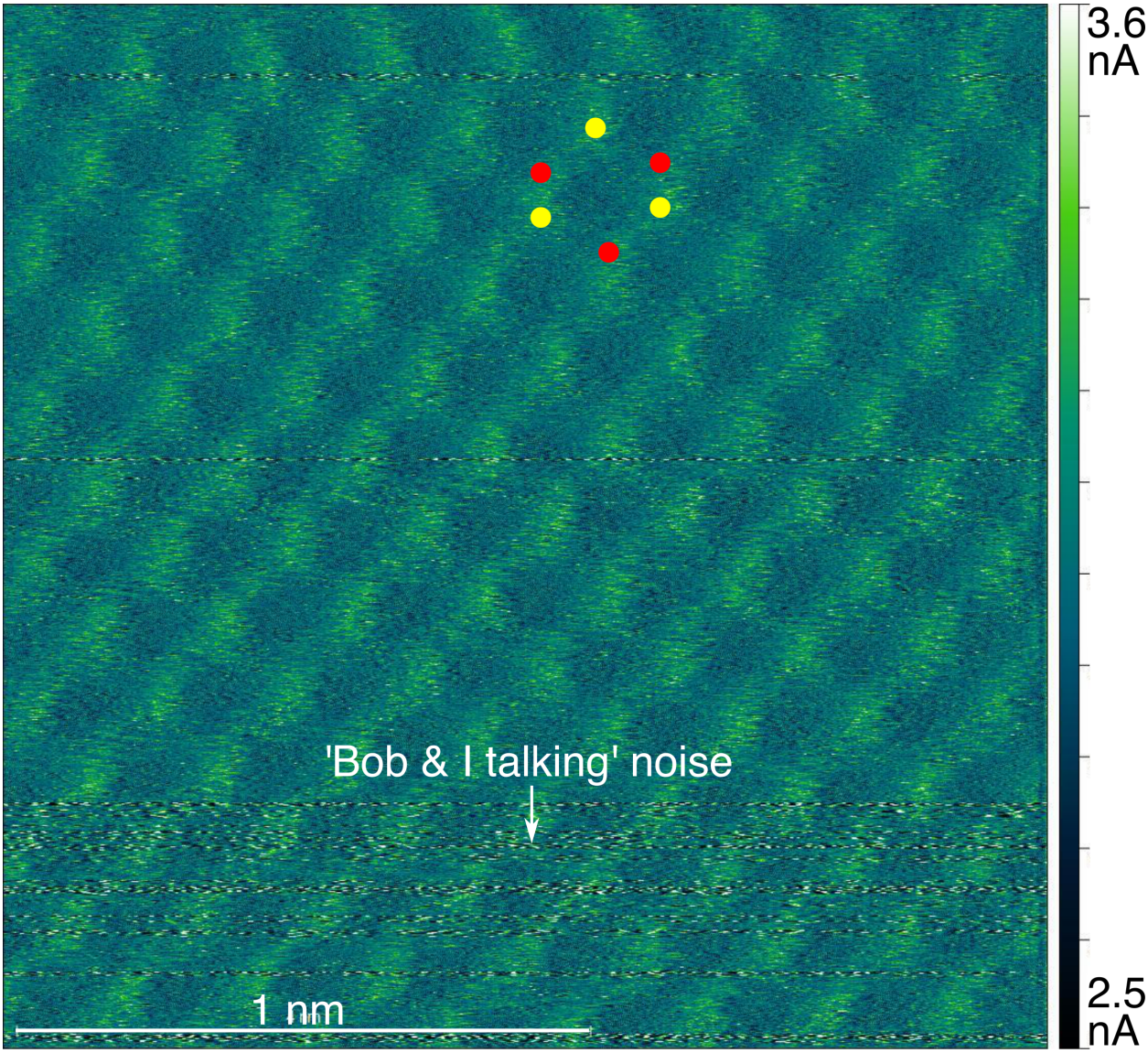

Figure 1.8: STM noise arising from external talking in the room. This noise can be eliminated by removing the pumping lines.

Chapter 2

Graphene

Graphene as a one layer thick material can be difficult to synthesize. Initial success came from exfoliation of highly oriented pyrolitic graphite by Novoselov and Geim with a scotch tape and transferring it to an oxide wafer. Exfoliation method is complicated because controlling the number of layers is probabilistic. The type of tapes with different adhesiveness like blue tape in contrast to scotch tape also play a role in getting thinner films. Such probabilistic method can only be improved but is not efficient. The only advantage of exfoliation method is that the atomic sheets are single crystal and defect free. Such exfoliated graphene have been measured to have mobility upto 10,000 cm^2/Vs. The choice of substrate also plays a role in these measurements. Graphene on a hexagonal boron nitride substrate can give ultra high mobility of 100,000 cm^2/Vs in contrast to silicon dioxide substrate.

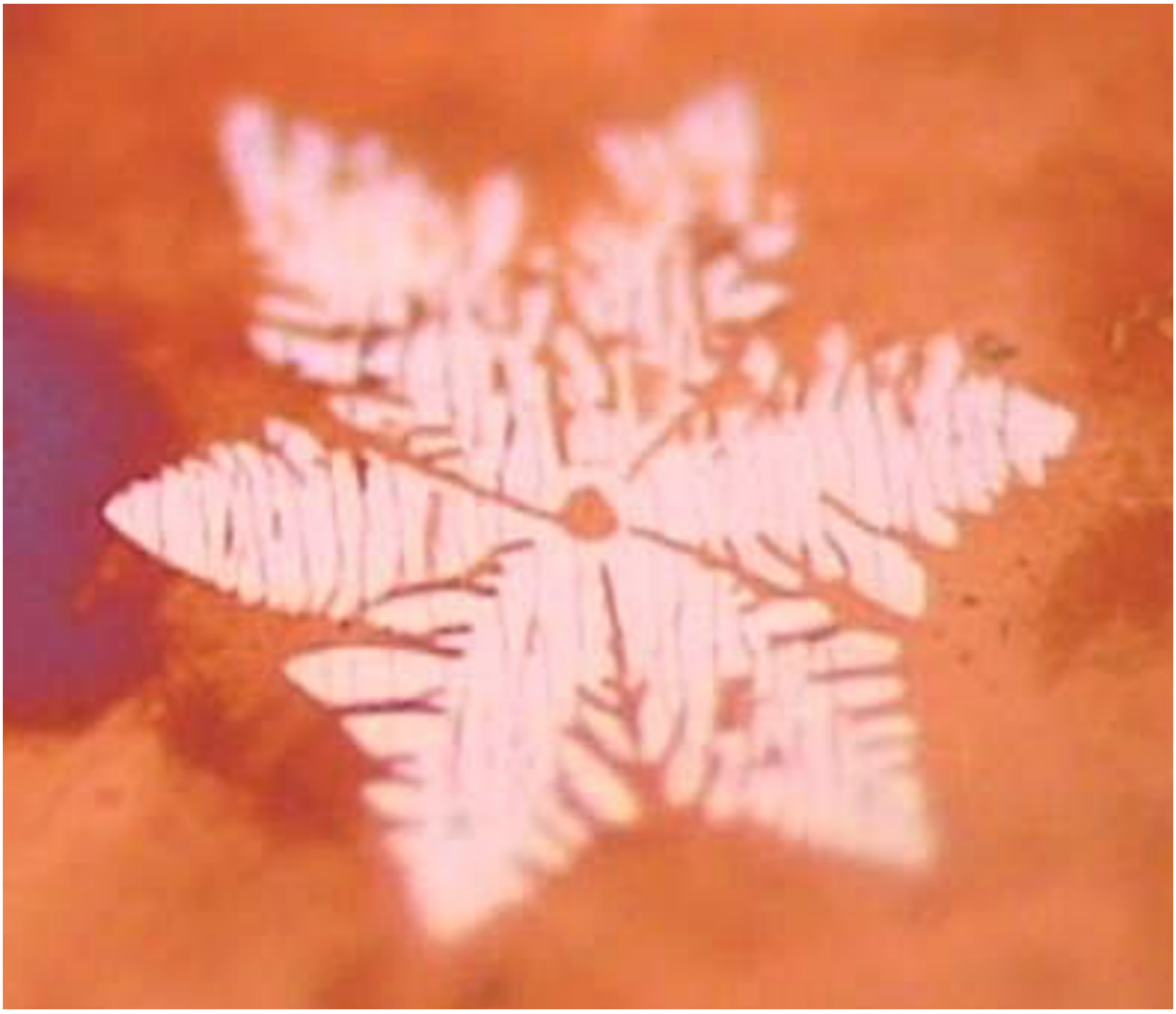

Figure 2.1: Single graphene crystal flower of 100 microns

2.1 Synthesis - Chemical Vapor deposition

Other than the mechanical exfoliation method, another possible route to synthesize monolayer graphene is by chemical vapor deposition. In organic chemsitry, the most common method used among oil industries to extract hydrogen gas from hydrocarbons is called as cracking or thermal decomposition. The reaction involves high temperature heating of the gas in a controlled

atmosphere in the presence of a metal catalyst. The carbon gets adsorbed or absorbed on the metal and the hydrogen is released from the metal surface. In this reaction, hydrogen is the main product whereas carbon is a by-product. Depending on the solubility of carbon in metal catalyst, one can control the allotrope of carbon obtained. High carbon soluble metals like Aluminium can help produce diamonds and less carbon soluble metals like Nickel can give several layers of graphitic carbon. Metal with no carbon solubility like Copper forms a single sheet of graphene on its surface. Copper allows very less absorption but mostly adsorption of carbon on the metal surface. This property of copper makes it an ideal candidate to allow surface passivisation with single layer of carbon after which the reaction becomes self-limiting. The nucleation of the first methane molecule becomes the centre point of each single crystal. Such nucleation occur mostly on copper defect sites. The density of defects

The simplest hydrocarbon that requires least thermal energy to dehydrogenate is methane that has 4 hydrogen atoms for every carbon. Each methane molecule nucleates itself to a hot metal copper surface as a methane CH_3^+ radical. Other methane molecules bind to the radical and begin to form a chain of carbon atoms. This chain grows in a hexagonal symmetry. Hence hexagonal shapes are observed on single graphene crystals. The nucleation of the first methane molecule occurs on the defect sites of the hot copper surface which then becomes the center point of it's single crystal. The grain sizes of the multi-granular graphene sheet would then depend on the nucleation density which in turn depends on the defect density. Granular graphene is not electronically preferable because of low electrical mobility. This requires a need to reduce the defect densities during the growth process. This could be possible by pushing the growth temperatures close to the melting point of copper which is 1080^oC. Such high temperatures around 1000^oC allows melting the copper surface and not the bulk. Larger copper grains are formed due to melting and re-crystallization only

on the surface. A molten copper surface allows floating of the methane radicals and reduces the nucleation density. This mechanism is not completely understood. Another way to reduce the nucleation density is by etching away nucleated methane radicals. This is achieved by increasing the hydrogen gas concentration ratio to methane. Methane gas is needed for graphene growth by de-hydrogenation of methane and hydrogen gas helps in graphene etch by re-hydrogenation of the nucleated methane radicals. The etching of these graphene crystals evolves in a fractal manner as shown in figure 2.2. With the increase in the H_2 : CH_4 ratio, we can observed the how the etching of carbon chains creeps into the single crystal like the veins of the leaf or splitting of blood vessels or shapes of lightning bolts. This is known as a branching fractal pattern.

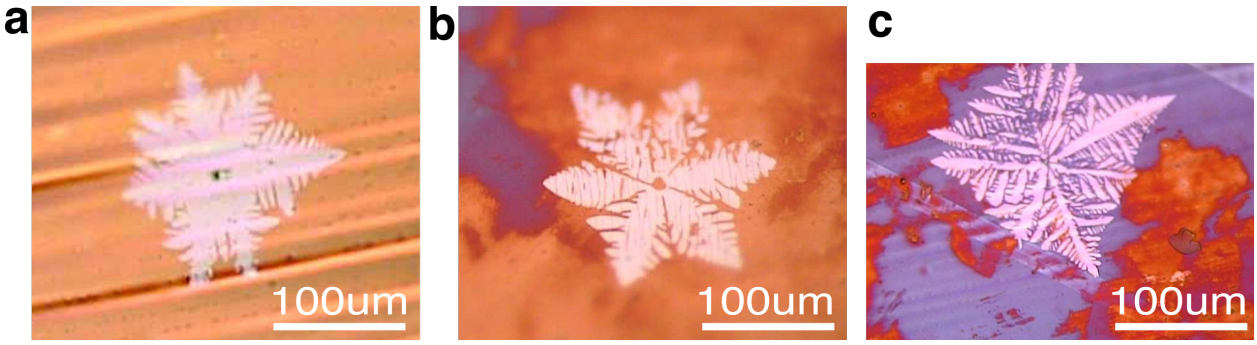

Figure 2.2: Fractal etching of single graphene crystal like veins of a leaf

A lot of industries since the late 2010's have developed that synthesize graphene on a large scale. Industrial graphene is granular with grain sizes of roughly 50 microns. There is a need for centimetre sized single crystal monolayer graphene in the market because minimizing defects to the point of large scale graphene growth is challenging. This invites the need to have a stable controlled atmosphere during growth. Such controlled atmosphere can by encouraged by using 'pocket' method. Larger crystals were observed on the inner side of Cu foil in comparison to the outer side. Penetration growth mode: C penetrated from one side to the other side of Cu foil and

formed another layer resulting in multiple layers. Low density of nuclei is due to the much lower partial pressure of methane and an "improved" environment during growth; that is, the Cu vapor is in static equilibrium, and there is potentially a much lower pressure of unwanted species. The differences in their growth can be seen from the following figure 2.3a and 2.3c. Etching these surfaces with hydrogen is shown in 2.3b and 2.3d.

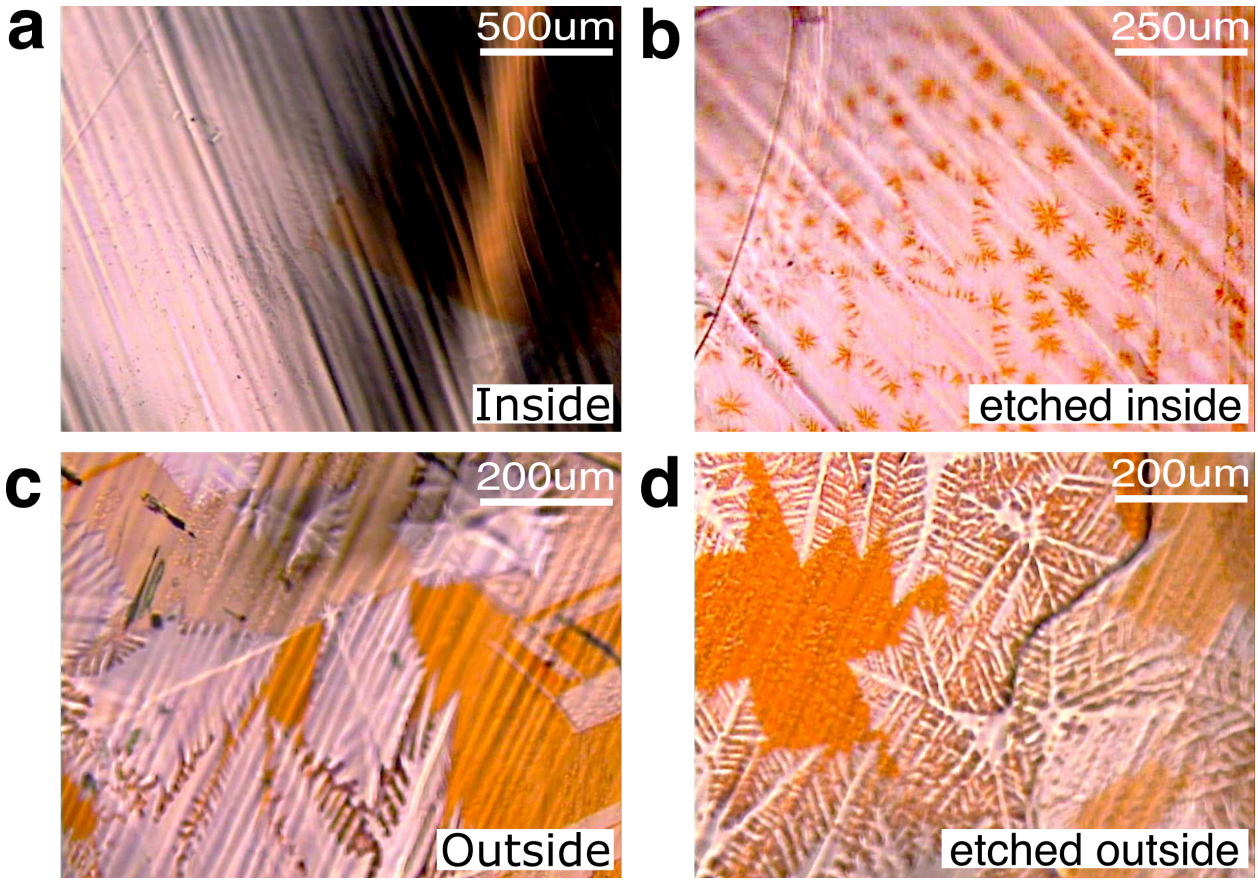

Figure 2.3: Fractal etching of graphene sheet

Another way to reduce the nucleation density is by using oxygen. Metal surface imperfections, such as step edges, defects, impurities, etc., can be active sites for graphene nucleation because of lower-coordination number which lead to strong binding to adsorbates like O or H. Introducing some oxygen before graphene growth oxidizes the defect sites. This reduces the nu-

cleation density and give rise to larger size grains of over millimetre.

2.2 Wet transfer

To be used in electronics devices, graphene deposited in a metal substrate has to be transfered to the desired substrate. Not only the growth process influences graphene quality, but also the transfer methods, since graphene quality can deteriorate during the transfer. This process involves the use of a support layer, such as PMMA or PDMS, leading to residue accumulation on the graphene layer.

PMMA is the most widely used polymer for CVD graphene transfer. PMMA covalently bounds to graphene, providing a better support for the carbon layer, leading to less cracking and rippling than PDMS. However, since the bounds between PMMA and graphene are stronger, it is more difficult to remove the polymer layer. First, PMMA is spin coated on to graphene grown in a metal (or in Si02). Polymer thickness can be adjusted with the spinning rate and the PMMA concentration. A similar procedure as also been carried out in HOPG (highly ordered pyrolytic graphite) flakes on Si02/Si. A baking step can be introduced to evaporate the solvent on the PMMA/graphene/metal stack. If the graphene layer is grown by CVD, both sides of the copper foil will have graphene on it. Therefore, a plasma etching step is required to remove the carbon layer in one of the metal sides, or else graphene residues may deteorate the graphene. To remove the metal layer, the stack is placed on a metal etchant like ammonium persulfate, and after the metal is fully etched, the PMMA/graphene is scooped out, placed on DI water and rinsed several times. After these cleaning steps, the PMMA/graphene stack is scooped out and transfered to the desired substrate (such as a SiO2/Si wafer). The excess water may be removed with using a nitrogen gun.

The stack may dry in air for a few hours, or it can be baked to evaporate the remaining water. To remove the remaining PMMA layer, the stack is placed in a acetone bath or it can be annealed in vacuum or in a N2, Ar, H2, or a combination of those atmosphere.

It has been assumed that they are caused by wrinkles and other defects that appeared in copper during the CVD growth process. A second PMMA layer approach has also been studied to reduce the breaking, rupturing and wrinkling of the graphene membrane. Improvements in transfer quality have been reported by adding an additional PMMA layer to dissolute the first one To improve the quality of the PMMA transfer and avoid degradation, various adjustments and optimization to the classic process have been carried. Graphene quality is also deteorated by PMMA residues that remained attached to the graphene after the acetone bath. These residues are difficult to remove since PMMA covalently bonded to graphene. Combined with breaking and wrinkling, these residues remarkably deteriorate the electrical and physical properties of graphene, decreasing carrier mobility. Graphene annealing has been used after the acetone bath to address this issue. Improvements have been reported with graphene annealing performed in UHV (ultra high vacuum) conditions and in vacuum furnace at 200oC. Using a lower molecular weigt PMMA has considerably reduced the amount of PMMA residues and given a optically clean sheet of graphene. An image of a wet transferred CVD graphene has been shown in following figure 2.4

This optical image allow us to evaluate the thickness uniformity and continuity of the film as well as residues, defects and broken region on the film in detail. Additionally, the image is also used to characterize the layer distribution of the few-layer graphene sheet on the wafer based on apparent color contrast of different regions. In figure 2.4, we observed the incomplete and partially grown graphene film made of many star-shaped (also known as lobe-shaped dendritic morphology) small domains. This suggests that growth time was not enough to form continuous graphene film

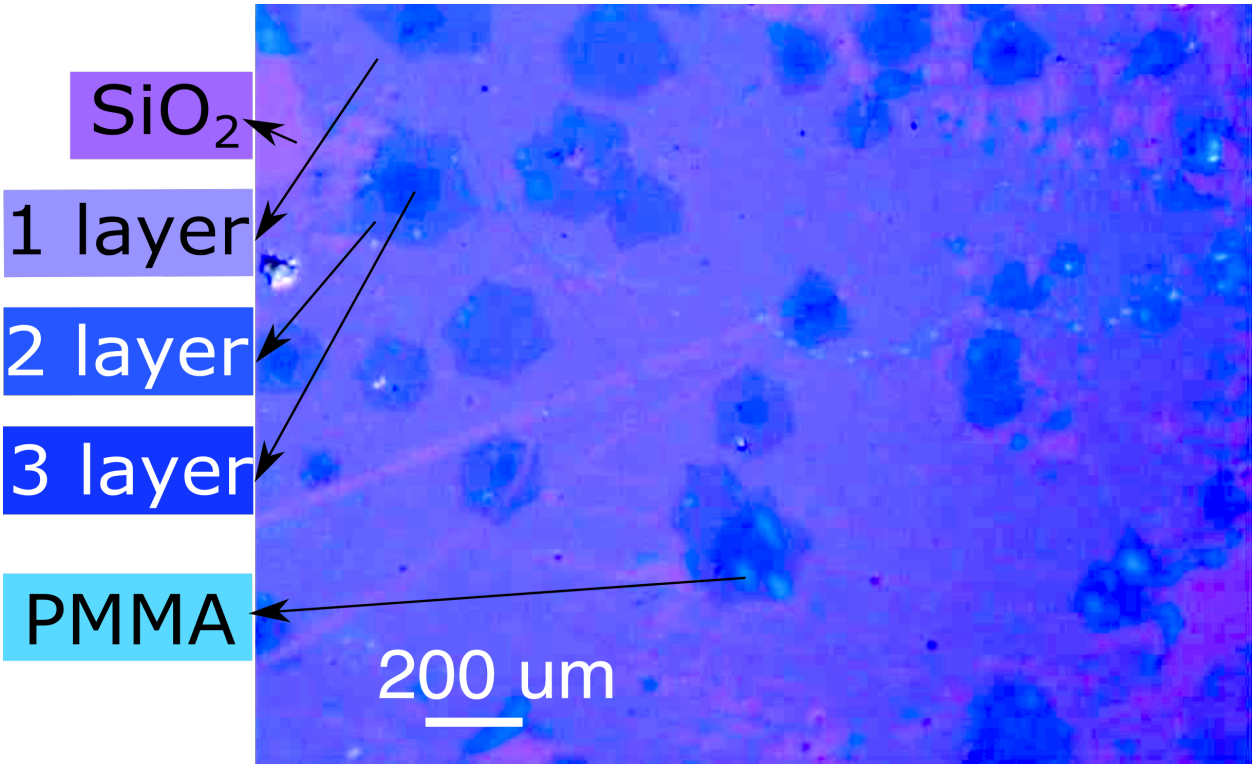

Figure 2.4: Optical image of wet transferred graphene on a 300 nm thick silicon dioxide on silicon substrate that shows the optical contrast of few layers of graphene and residues due to thin film interference

or the film had incomplete wet transfer. Even though it was clean and uniform over the whole region, polymer residues and wrinkles were still found in the film. The darker region corresponds to thicker layers. It is probable that the few layer regions help to stitch the monolayer regions, preventing disruption or breaking in the graphene.

2.3 Raman characterization

Raman spectroscopy is a powerful tool for characterizing 2D materials including graphene. It has been universally used to study the number of graphene layers, evaluate the presence of defects and doping or strain in graphene, and also the stacking order of bilayer graphene. As can

be seen in figure 2.5, the CVD-grown monolayer graphene film exhibits two most intensive Raman modes and another disorder-related peak: a doubly-degenerate in-plane sp2 C-C stretching mode (G band) at 1580 cm-1 which is first order Raman process, an in-plane breathing-like mode of hexagon ring consisting of six carbon atoms (2D band) at 2700 cm-1 which is also referred to as a second order Raman mode, the disorder-related mode (D band) at 1350 cm-1 (see figure 2.5), induced by the symmetry breaking in graphene lattice such as point defects, edges, grain boundaries or impurities. We could measure the deformation and strain from the width of G peak because the two-degenerate modes start to split into the G+ and G- band under deformation. The number of graphene layers could be determined through the 2D band, this peak can dissociate into several peaks when the graphene is not a single-layer. The Raman spectrum in figure 2.5 shows broad 2D peak comprised of several sharp peaks, which evidences the existence of multi-layer graphene.

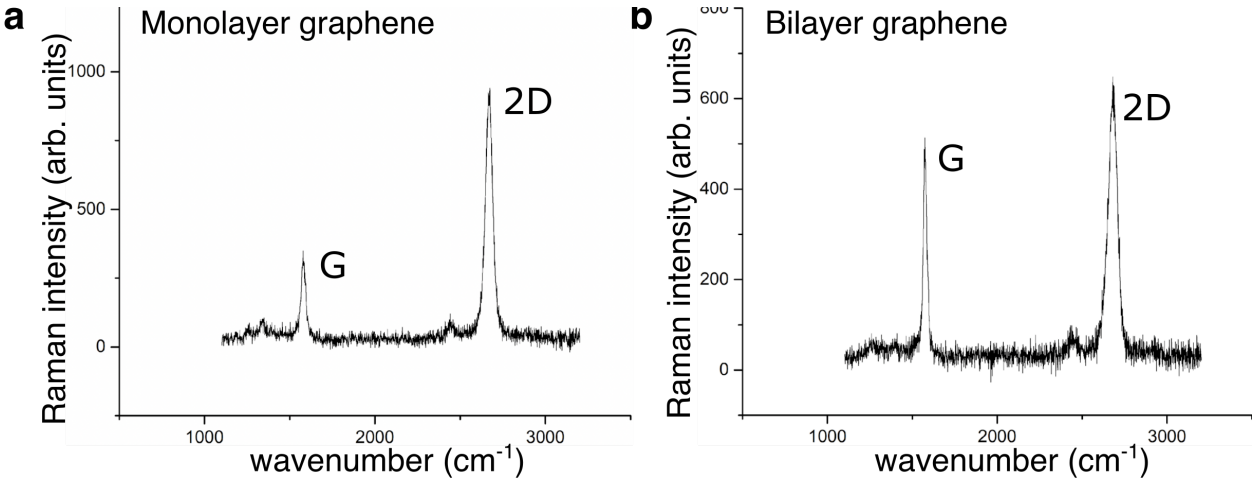

Figure 2.5: Raman spectra signatures for mono layer and bilayer graphene

Specifically, one sharp 2D peak becomes the superposed four sub-2D bands by the addition of the second layer, leading to the increase in the bandwidth. The ratio between the intensities

of the 2D and G bands (I2D/IG) can be indicative of the number of graphene layers as well, it has a tendency of decreasing as the number of layers increase. But, the intensity ratio is also linked to disorder and the doping so that the shape of 2D band is a more reliable estimation of the layer thickness. In the figure 2.5 (a), the confocal Raman spectra of our CVD-grown monolayer graphene showed relatively high I2D/IG and sharp 2D band, reflecting the fact that the region under examination is monolayer. The D peak suggest the presence of defects in the graphene. The multilayer graphene was also characterized by Raman and the spectra were shown in figure 2.5. It shows low I2D/IG intensity ratio and a broad 2D band. These suggest optimization on CVD-grown few-layer graphene is inevitable in the near future.

2.4 Device preparation

The most common way to pattern graphene is oxygen plasma etching that readily attacks and removes carbon. For dense patterns or smaller features where mask transfer accuracy is critical, a plasma technique with some ion bombardment level is necessary, such as commonly used reactive ion etching. If accuracy is not important then a hard mask stencil is an ideal defect-free etching method. When using dry etching methods, the patterning material, photoresist, must be considered carefully to ensure it sustains the etching process while being easily removed after patterning, leaving few residues on graphene. Several hall bar patterns have been made on graphene as shown in figure 2.6. Rectangular and bug patterns are some of the common hall bar designs. When using only photoresist on graphene, it leaves residues and get chemiadsorbed on the surface in figure 2.6b. On using a sacrificial layer of PMMA between photoresist and graphene, the graphene remains protected from photoresist while oxy-plasma etch process. Thicker PMMA

made the etching time longer which also affected the electrical contact between graphene and pads. Minimizing the etching time by reducing the PMMA thickness when diluted with chloro-benzene or anisole maintained the electrical contact. The origin of the contact issue lies with the transfer of graphene on pre-patterned gold pads on wafer. This can be avoided when contacts are evaporated onto graphene and not the other way around. If the pad features are not too small, then evaporating through hard mask stencil is the best option. Usage of resist based stencils leaves polymer residues. Electrical mobility can be calculated after patterning graphene in a van der pauw geometry. Patterns with a length to width aspect ratio is preferred over square van der pauw geometry. This allows the contacts to probe the transverse and longitudinal potentials along and across the length of the thin film. A current or potential map can be developed based on these numbers. Ideally if current is applied along the length, the transverse resistances should be zero and the longitudinal resistance should be dependent on the

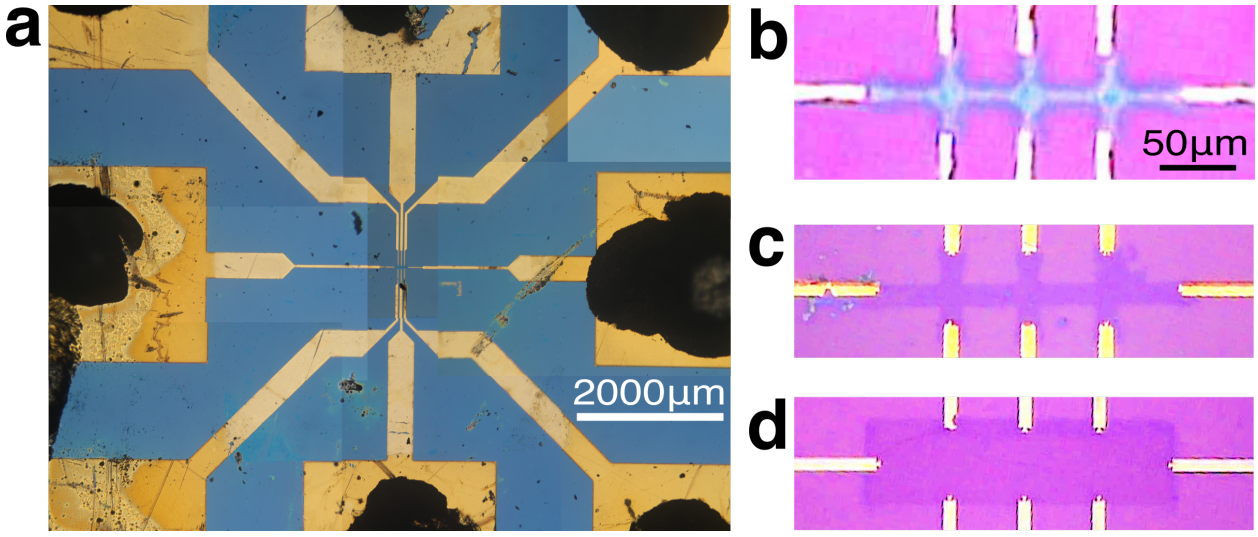

Figure 2.6: Bug pattern of gold pads on graphene etched into van der pauw geometries

If 1,2,3,4 are the contacts on the square, Longitudinal resistance(Rl) are R12=R23 98 Ohms

Sheet Resistance Rs= Rl pi/ln 2 = 444 Ohm/sq

Transverse resistances(Rt) are : R13=R24=9 Ohms without B R13 = 5 Ohms with 1000 Gauss R24=12 Ohms with 1000 Gauss

Hall coefficient, RH = avg of two ΔRT = (ΔR13 + ΔR24)/2 = 3.5 Ohms Calculating n from equation, RH=B/ne where B=1000 Gauss or 0.1 T gives n= $1.7x10^{13}/cm^2$

Calculating mobility (u) from equation, u = 1/neR_s = 828 cm^2/Vs

Various mobility numbers varying from 1000 to 3000 cm^2/Vs were obtained. These electronic mobility numbers went double at liquid nitrogen temperatures. The magnetic measurements were done by making a wooden block having slots for two permanent magnets on its sides aligned along the same axial direction.

2.5 Metal insulator transition

Helium ion microscope can be used to create focused ion beam lines on graphene surfaces to test metal insulator transition. These lines are of the doses 0.5,1,2,4,6 and 8 kilo-ions per nm on the 6 hall bars. Resistance measurements at room temperature and liquid nitrogen temperatures revealed that resistances across the 0.5 and 1 k-ions per nm doses went down indicating metallic behavior. Resistances across the doses 2 k-ions per nm and higher went upwards indicating insulating behavior. This experiment helps determine the amount of helium ion doses needed to drive the metal to insulator transition.

This was repeated again on another graphene hall bar device with doses from 2 - 12 kilo-ions per nm on the 6 hall bars. All the resistances across the doses went insulating at liquid nitrogen temperature therby indicating that 2 kilo-ions per nm is strong enough dose to break

carbon - carbon sp2 bonds.

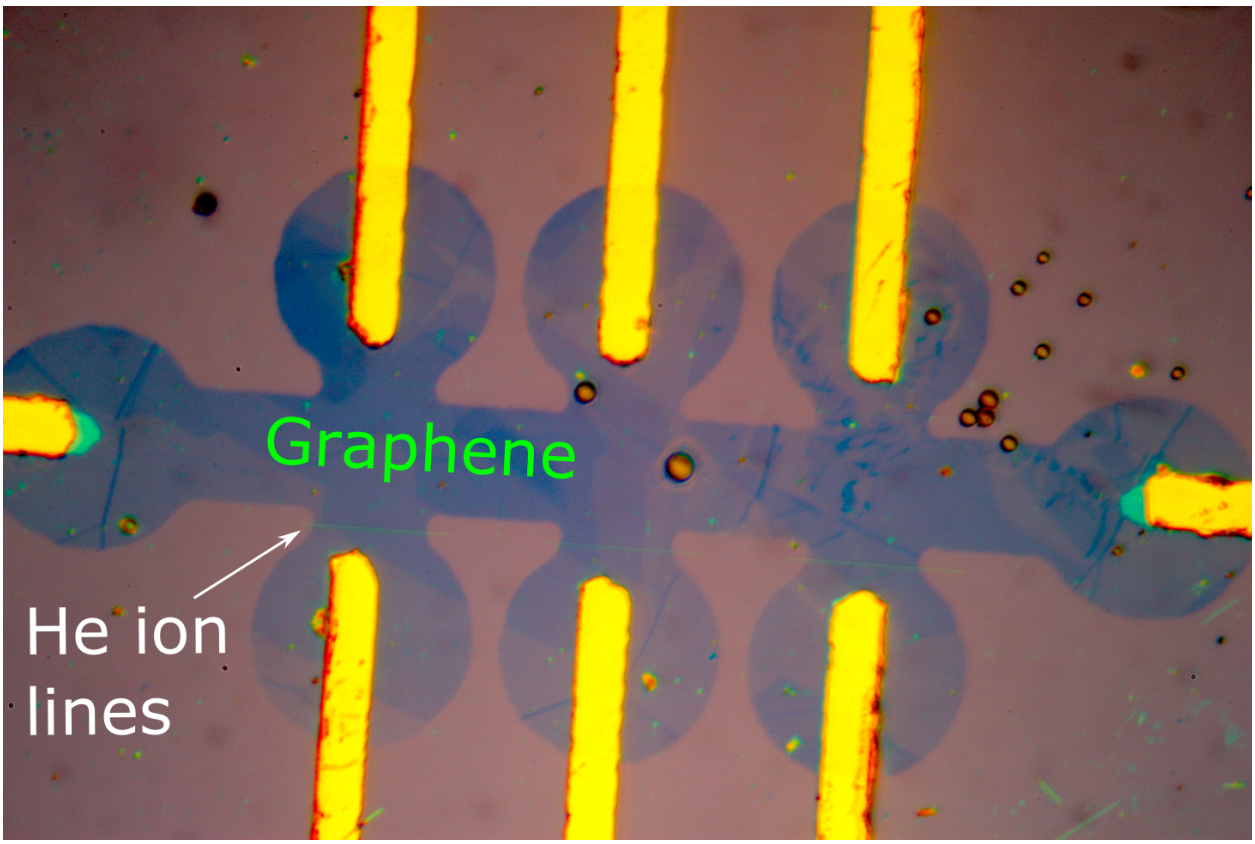

Figure 2.7: He ion damaged lines on graphene hall bars

2.6 Summary

Graphene is a single atomic sheet of carbon that needs care and precision to synthesize and fabricate devices out of it. The usage of metals and polymers have been fundamental in this process. Graphene can be grown as almost defect-free crystals but majority of the defects are developed during the wet transfer process. This can be avoided by growing graphene on substrates directly therby avoiding the transfer methods.

Chapter 3

Step edges

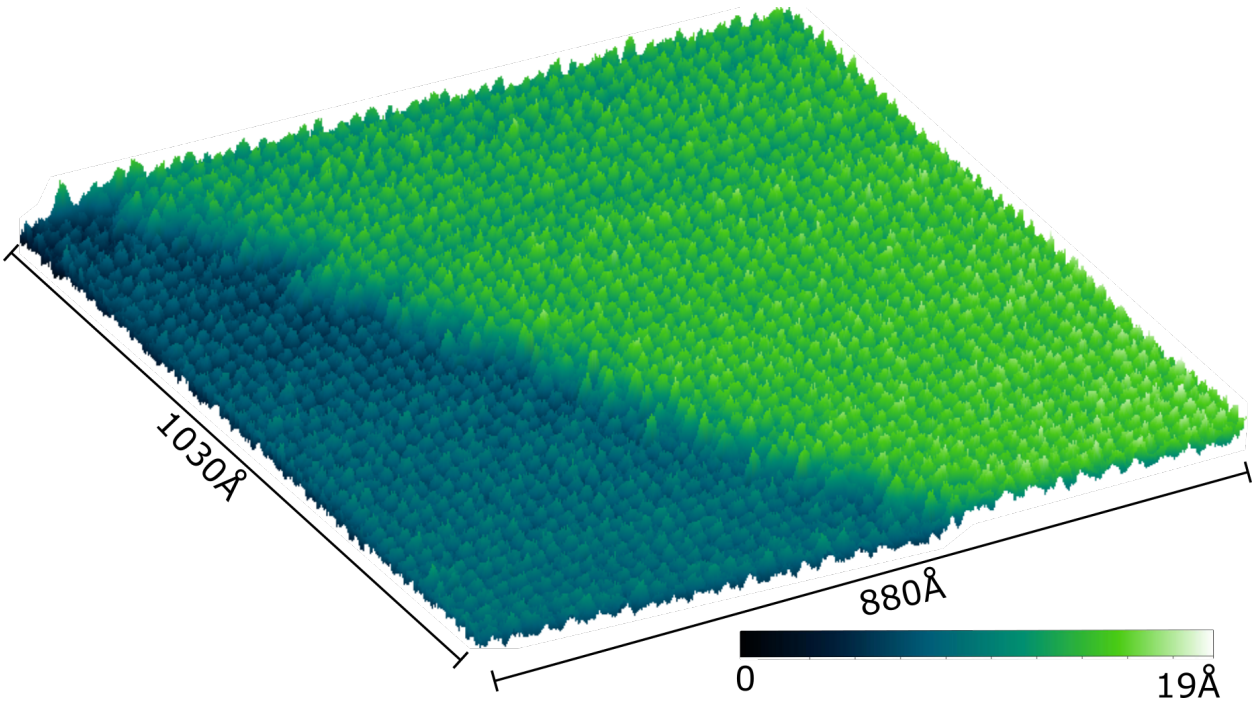

Figure 3.1: 3D image of a monatomic step height

Graphite or Highly oriented pyrolytic graphite (HoPG) has been extensively used in STM as calibration standard[1, 2] for height determination assuming definitive and delineated step heights

arising from a presumed atomic flatness and surface cleanliness[4–6].

3.1 Anomaly

However STM measurements show that on either side of a step, there is confusion about the flatness arising from atomic corrugation yielding amplitude enhancement[7–9]. For instance, while the measured atomic amplitudes on graphite surface are expected to be 0.2A from Local Density of States (LDoS) calculations[10–13], abnormally high atomic amplitudes have yet to be observed14-16. Such anomalies have been attributed to direct interaction of tip and surface inducing local elastic deformation of graphite surfaces particularly at small tip-surface separation[7, 14]. However, in our own investigations we have observed step heights to be constant in spite of the existence of large atomic corrugations on layers around the step edge. Consequently, the step height is an accurate calibration feature for STM with a constant topographic height irrespective of tunneling conditions.

However, large atomic corrugations could not be explained through models related to electronic state variations[10–13] on graphitic surface but were attributed14 to mechanical tip-induced surface deformations. Such local deformations [14] by sliding/shear between basal planes in the 2-D layered materials. To seek better understanding of such dual forces21, we compare atomic topographies on surfaces of distinct materials and observe that the anomaly related to large atomic amplitudes exists only on graphite surface but is suppressed on single-layer graphene (SLG) and $NbSe_2$. Consequently, the graphite surface may be deformed easily compared to surfaces of $NbSe_2$ and SLG and leads towards an explanation involving vdW bonding dictating their surface properties. To further test our idea, we choose surface features incorporating moiré patterns with spatially

variable inter-layer vdW bonding[4, 21–23]. We then demonstrate that the tip-induced deformation across the Moiré landscape reveals local vdW bonding variability.

3.2 Steps vs anomaly

Figure 3.2a shows a schematic related to tip-induced deformation/warp on surfaces of soft vs rigid materials at small gap distances (or higher tunneling currents). Monatomic steps on Graphite (in figure 3.2b) and $NbSe_2$ (in figure 3.2c) are subjected to different tunneling currents (corresponding to different tip-sample gaps) in figure 3.2d and 3.2e.

The measured atomic amplitudes of graphitic surfaces, $NbSe_2$ and SLG and their average is compared as a function of I_{tip} (in figure 3.3a at constant Vsample) and Vsample (in figure 3.3b at constant Itip). Monatomic step heights of graphite and $NbSe_2$ have also been estimated from figure 3.3d and 3.3e as indicated.

With the increase in Itip from 10nA to 90nA or an equivalent decrease in Vsample from 500mV to 50 mV (ref fig 3.3), we observe an anomalous increase in the atomic amplitudes of graphite from 1.5Å to 3.5Å (as also observed in[7, 9]) but the monatomic graphite step height remains relatively constant around 3Å. The spatial frequency of the oscillations in figure 1d is uniform and 2.5Å (shown in fig 3.3c middle inset). Despite the oscillation amplitudes in figure 3.2d being proportional to the LDOS contours20, the earlier models[10–13] of electronic tip-sample interaction could not explain such a large increase in the amplitudes. One explanation by Soler et al[7] posited the local elastic deformation of the 'soft' graphite surface by the tip as responsible. The compressive and expansion forces between tip and graphite were calculated on the basis of an interatomic potential interaction model[7, 9, 11, 15–17, 20] with a variable geometry of the

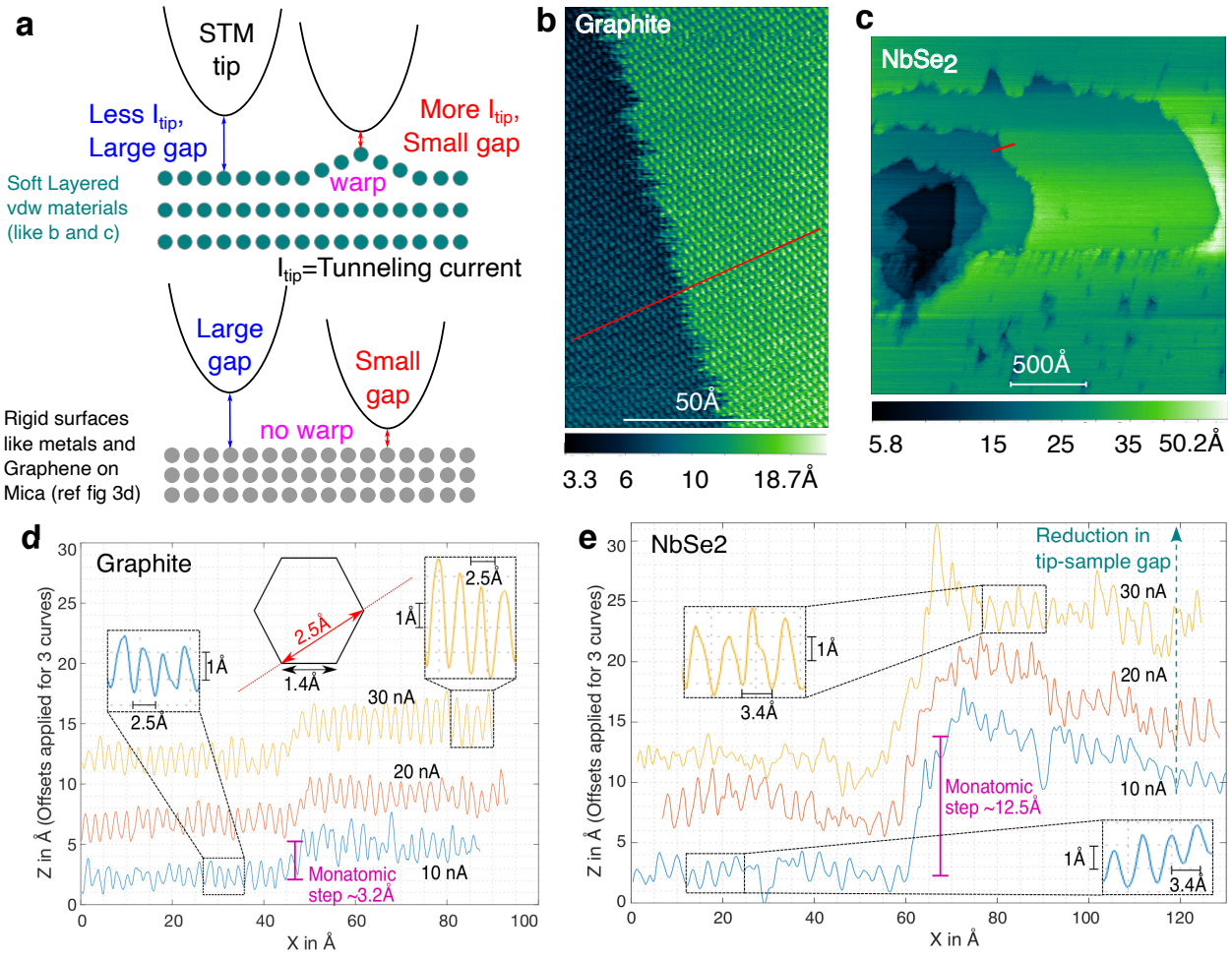

Figure 3.2: Atomic deformation across graphite and $NbSe_2$ steps as a function of gap distances/ tunneling currents. a, The expected response of rigid vs. soft materials to tip induced deformations at smaller gaps or higher tunneling currents). b,c, 2D topographic images of a monatomic step height on graphite surface (100Å x 145Å) in b and a series of monatomic step heights on the $NbSe_2$ surface (2300Å x 2300Å) in c. Both images have been measured at 30nA tunneling current (I_{tip}) and 100m sample bias (V_{sample}) where the color bar is the measured topographic height in angstroms (Å). d,e, Tunneling current dependence of atomic topography along the red line in b and c as shown in d and e. The oscillations in each curve correspond to individual atoms. The insets in d and e magnify curves at 10nA and 30nA respectively to show the increase in average oscillations amplitude from 1.5Å to 2.7Å for graphite in d and from 1.7Å to 2.4Å for $NbSe_2$ in e. The spatial frequency on either side of step height remains constant at 2.5Å for graphite in d and at 3.4Å for $NbSe_2$ in e. Graphite lattice constant of 2.5Å corresponds to the lattice spacing for HoPG in the a-b plane in the middle inset of d. The oscillation amplitudes and step heights estimated from d and e are plotted in figure 3.3 as a function of Itip and Vsample.

tip apex. We have used the same tip in our experiments to ensure the reproducible application of deformations on these 2D surfaces.

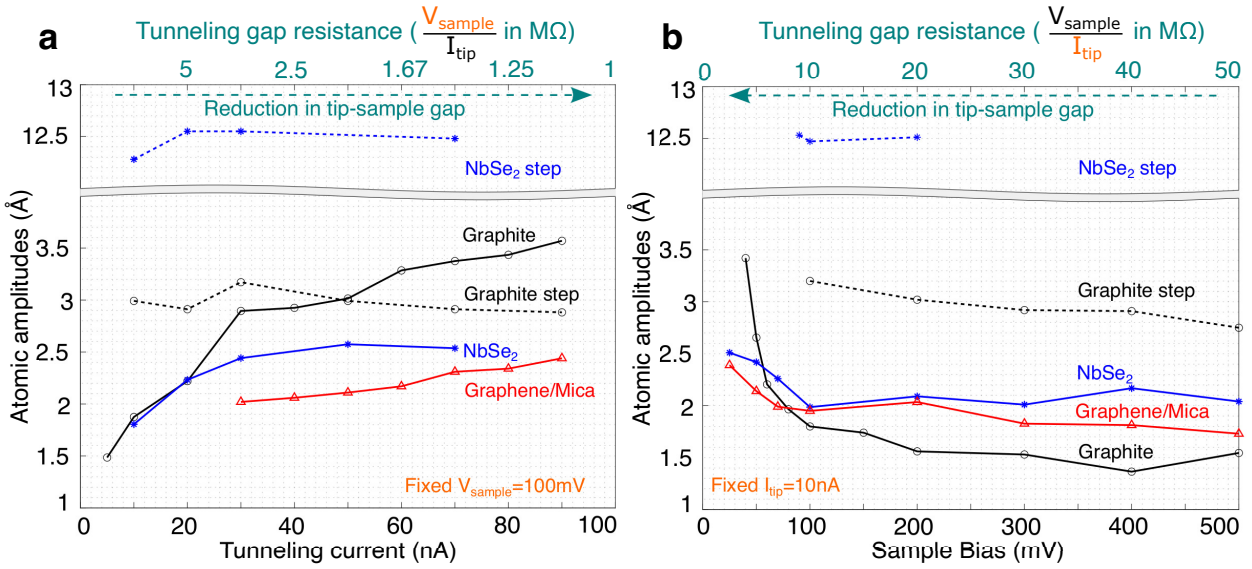

Figure 3.3: Atomic deformation of 2D surfaces. a,b, With the increase in tunneling current Itip in a or decrease in sample bias Vsample in b, measured atomic amplitudes increase more on the graphite surface compared to those observed on $NbSe_2$ and monolayer graphene surfaces. Monoatomic step heights of graphite and $NbSe_2$ measured from figure 3.2d and 3.2e remain constant around 3Å and 12.5Å respectively. The top horizontal axes in both the plots show the reduction in tunneling gap resistance(Vsample / Itip) or gap distance.

Compared to graphite, $NbSe_2$ shows a smaller enhancement in atomic amplitudes from 1.5Å to 2.5Å and SLG amplitudes are enhanced slightly as well, i.e., from 2Å to 2.5Å in figure 3.3 plots. Such enhancements through the variation in Itip and Vsample may be best understood from the change in tip-sample gap (shown by arrow on top of figure 3.3 plots). A reduction in tip-sample gap leads to a diminution in tunneling gap resistance.

3.3 Local deformation theory

It has been suggested[7, 14] that the attractive (/compressive) forces from the tip cause an outward (/inward) deformation of the 2D surfaces which would be opposed by the elastic shear forces along the basal planes – as (schematically indicated in fig 3.4a,b). The opposing shear force would then depend on the c-axis distance of the vDW bonding. The nearest vDW related bonding,

could be assigned to be 3 layers deep in $NbSe_2$ and one layer deep in graphite. The shear force along basal planes would be expected to be higher for thicker triatomic Se-Nb-Se sandwiches (of height 12.5Å each) compared to lighter monatomic sheets of graphite (of height 3.2Å each). This explains why the 'soft' graphite surface gets deformed more than 'rigid' $NbSe_2$ under the same tip-induced deformation.

It was previously reported[10, 11, 13, 17] that atomic corrugations on graphite were related to the tip-surface mediated electronic interactions. Since the top layer of graphite is nominally the same as SLG, a similar tip-surface electronic interaction yielding comparable deformation would be expected. However, from figure 3.3 plots we observe little enhancement of atomic amplitudes of SLG compared to much larger enhancement in the case of graphite. Each graphite layer is bonded by weaker VDWs but the SLG sheet is only bonded to an underlying mica substrate through Coulombic interactions30,31. This suggests that the anomalous corrugations of graphite surface are not just tip-surface electronic interactions but also involve the underlying bulk. The difference in amplitude variations also indicates that the bonding of SLG to the mica substrate is stronger than the vDW bonding between graphitic layers. From figure 3.3 plots, the same amount of deformation amplitudes (with Itip and Vsample) for $NbSe_2$ and SLG The similarity in deformation amplitudes of $NbSe_2$ and SLG in fig 3.3a and b indicates that the Coulomb interactions between graphene and mica substrate may be comparable to the bulk shear forces along Se-Nb-Se sandwiches.

Ideally in STM's constant current mode, the feedback circuit in a usual STM mode between the z piezo and the tunneling current causes reduction in tip-sample gap with increasing Itip or decreasing Vsample to maintain that constant current. From fig. 3.3 plots it seems that the atomic corrugations of these surfaces get enhanced as the tip scans these surfaces at smaller gap distances. Reduction in tip-sample gap can also be seen as reduction in tunneling gap resistance (scaled on

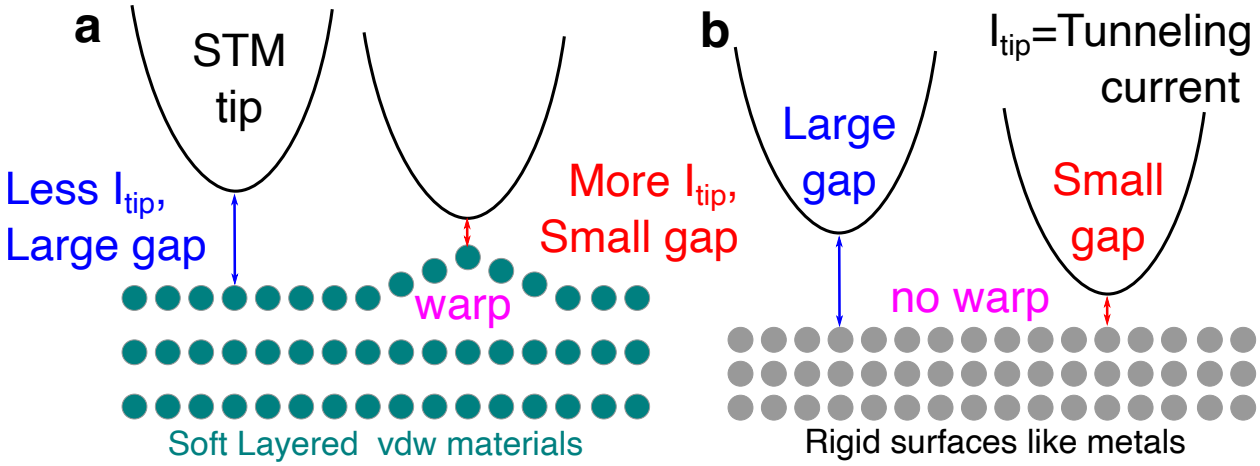

Figure 3.4: Structural anisotropy of 2D materials and their distinct exfoliation patterns. a-b, Graphite is made up of single-atom-thick carbon sheets stacked upon one another bonded by weak VDWs. Tip-induced local compression in a and expansion in b of graphite surface correspond to repulsive or attractive tip-surface interaction. Both deformations are opposed by shear forces(arrows) along basal planes. c, $NbSe_2$ unit cells are made up of a strongly bonded Se-Nb-Se sandwich stacked upon another by weak VDWs. Under the same tip induced deformative force, the local outward deformation of the triatomic $NbSe_2$ sandwiches are lesser than b. d, Single layer graphene (SLG) surface responds less to the tip induced deformation because of stronger coulomb interaction with it's mica substrate due to charge transfer [24, 25]. Mica substrate is chosen because it creates atomically flat cleaved surfaces.

top of fig. 3.3 plot axes). So variations in Itip and Vsample in figure 3.3 plots can be seen as a function of tunneling gap resistances as shown in supplementary figure 3.5 (looks same as figure 2b).

At large gap distances or above 10 MΩ (in fig 3.5 and 3.3b), measured atomic amplitudes of all materials become consistent. At small gap distances or under 10 MΩ (in fig 3.5, 3.3a and b), atomic corrugations become dominant. The atomic corrugations under 10 MΩ are more for graphite than others. The onset of this corrugation at 10 MΩ (also been observed in fig.3.5 of ref [1]) implies that the deformative forces of the tip become strong enough at smaller gap distances to overcome the shear bulk forces in these 2D surfaces. When calibrating z piezo of STM, the recommended tunneling gap resistance must be above 10 MΩ to avoid any deformative forces

interrupting the STM topographic measurements.

The coinciding curves for Itip and Vsample dependence of each sample exhibits the repeatability of the atomic corrugations amplitudes which is high for graphite and less for $NbSe_2$ and SLG. The enhancement in atomic amplitudes is caused by the reduction in tip-sample gap. Following a standard elastic model, an exponential increase in atomic amplitudes (seen in fig 3.5) should be caused by an exponential reduction in tip-sample gap. This exponential reduction in tunneling gap distance occurs with a linear reduction in tunneling gap resistance in figure 3.5. This is actually typical for STM and such a relationship has been studied on graphite [18, 26].

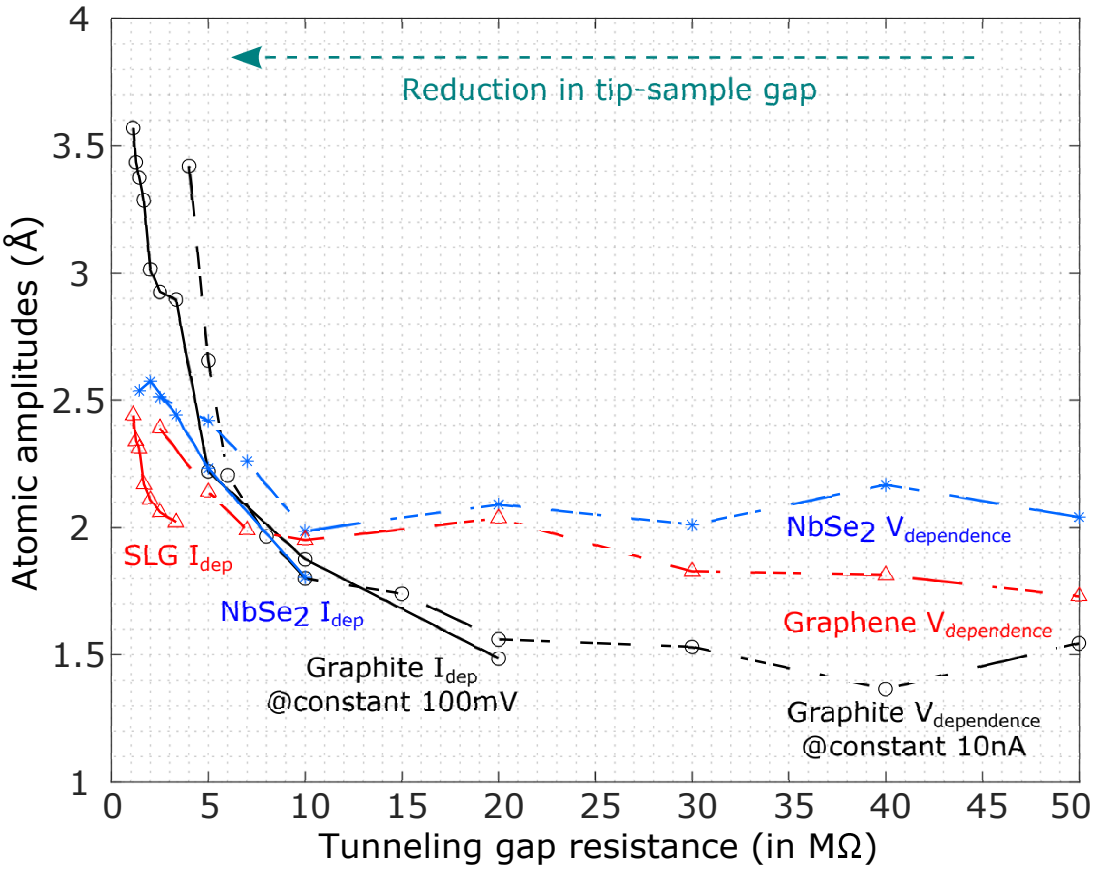

Figure 3.5: Standard deviation of local maximas and minimas of graphite atomic topographies in figure 3.8. Inset shows a portion of atomic topography at nA from fig 3.2d to exhibit the local minimas have lesser deviations than local maximas.

We further comment on the elastic interactions of the tip on 'soft' vDW layered surfaces in contrast to rigid metal surfaces. Ideally in a standard constant current STM mode[7, 18], the tip traces the potential contours over the rigid atomic surface without deforming it. However, as the graphite surface is soft, its surface may be more easily deformed. This is shown by expanding on the experimental atomic topography across the graphite monatomic step through the models in figure 3.6. In spite of the amplitude enhancement from 3 nA to 30 nA, the difference of the baseline of the corrugated layers on either side of the step differs by a fixed and constant step height. The topographic waveform at 30 nA appears as large as the step height.

Such large atomic corrugations cannot be explained purely based on electronic considerations alone but seem to imply considerable pulling outwards of the atoms. Such deformations (in fig. 3.6) occur predominantly at smaller gap distances with the hills (/valleys) corresponding to outward (/inward) atomic deformations. Following Soler's elastic theory14, there is expected an attractive force interaction when the tip pulls the atom outwards (labeled 2 in fig. 3.6 inset) and a repulsive force interaction when the tip pushes the atom inwards into the bulk (at position 1). It has been suggested14 that the inward atomic deformation into the bulk by the tip would be opposed by a stronger restoring repulsive force compared to the case of outward atomic deformation. The related difference was observed14 in terms of a preference towards stronger minima in the atomic topography of graphite (also see supplementary information 2).

These local atomic deformations are elastic over a large range of Itip or gaps as the atomic amplitudes in figure 3.3 plots remain consistent for a given tip.The influence of vDW bonds in these layered anisotropic 2D materials in determining their atomic deformation amplitudes and distinct exfoliation patterns can be extended to the case where the layers are slightly out of registry with respect to each other.

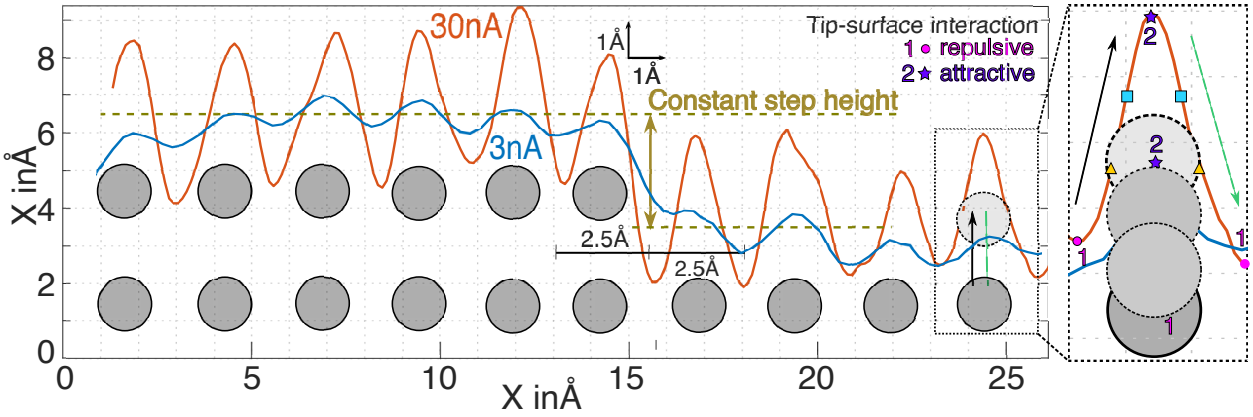

Figure 3.6: Atomic deformation across monatomic step. Schematic of plausible atomic topography across a monatomic step height (measured by the difference in mean of the two waveforms on either side of the step) enhanced at tunneling currents of 30 nA (red line) than at 3 nA (blue line), indicating anomalously high atomic corrugation amplitude. It is noted that the wavelength of 2.5Å and step height remains consistent at both currents. The right inset indicates the rationale for the anomaly through tip induced local deformation at an atom outwards and inwards related to attractive and repulsive tip-sample interactions. This allows for the indicated placement of the carbon atoms.

The structural anisotropy of graphite and $NbSe_2$ not only bring about varied responses to deformations but also their distinct exfoliation patterns. Monatomic graphite step edge (in fig. 3.7) look serrated by 10Å whereas the $NbSe_2$ step edge grooves are 100Å (shown in the inset middle of figure 3.7). Atomically resolved image in figure 3.7 reveals that graphite step edge look serrated with the related triangular edges following the crystal axes direction b and a (shown by red and blue arrows in fig. 3.7) and the step edge direction (labeled by a white arrow) is along the vector sum of a and b – related to the exfoliation direction. Thin monatomic sheets of carbon attached with weak VDW allows bonds tearing in a and/or b direction only. Since the exfoliation direction is aligned closer to b than a, more covalent bonds are broken along b than a.

In the case of $NbSe_2$, the exfoliation seems to follow an alternate pattern to graphite. Thicker Se-Nb-Se layers provide higher shear forces (compared to those nominally encountered in graphite) with a propensity for one-layer deep circular pits labeled as micron and nano pits in

figure 3.7b. The micron-scale pits diminish in size from the surface to the bottom.

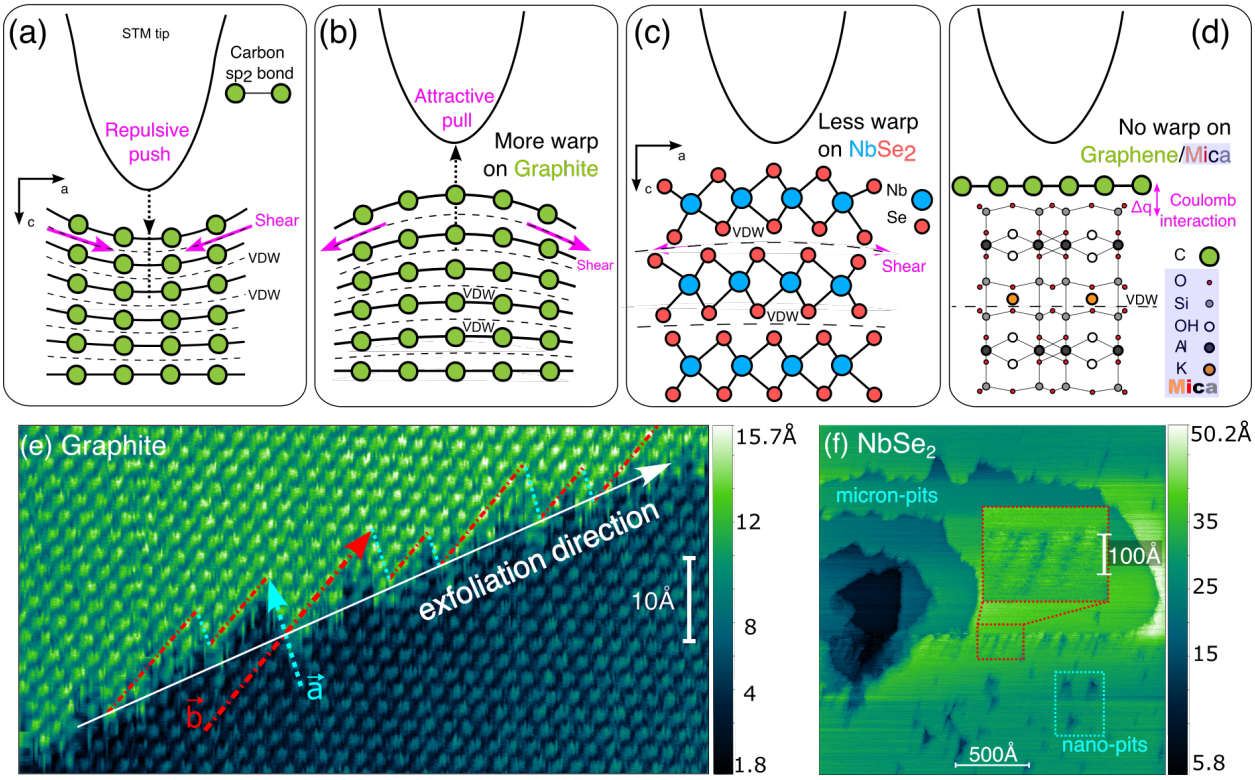

Figure 3.7: a, Atomically resolved topographic 2D image of the graphite monatomic step edge. Exfoliated graphite edges tear along crystal axes direction a (in blue) and b (in red) to create a sawtooth like step edge of height 10Å or less. b, 2D topographic image of a series of monatomic step heights on the $NbSe_2$ surface showing tears along the step edges of 100Å in inset. Shear forces in $NbSe_2$ compete with the external exfoliation force creating rounded exfoliated micron and nano sized pits.

3.4 Nature of the deformations

The local maximas and local minimas in atomic topography correspond to the outward/inward deformations of atoms. Outward pull of atoms into air should be different from the inward push of atoms into rigid bulk. Soler et al suggested that inward push of atoms into the bulk invokes a repulsive force interaction with tip and surface but the outward pull of atoms into air causes an attractive force interaction. Since these interactions follow the inter-atomic potentials at small gap

distances, the repulsive force is stronger than attractive force which is typical for interatomic potentials (like morse potential). This difference shows up in the features of local maximas vs local minimas.

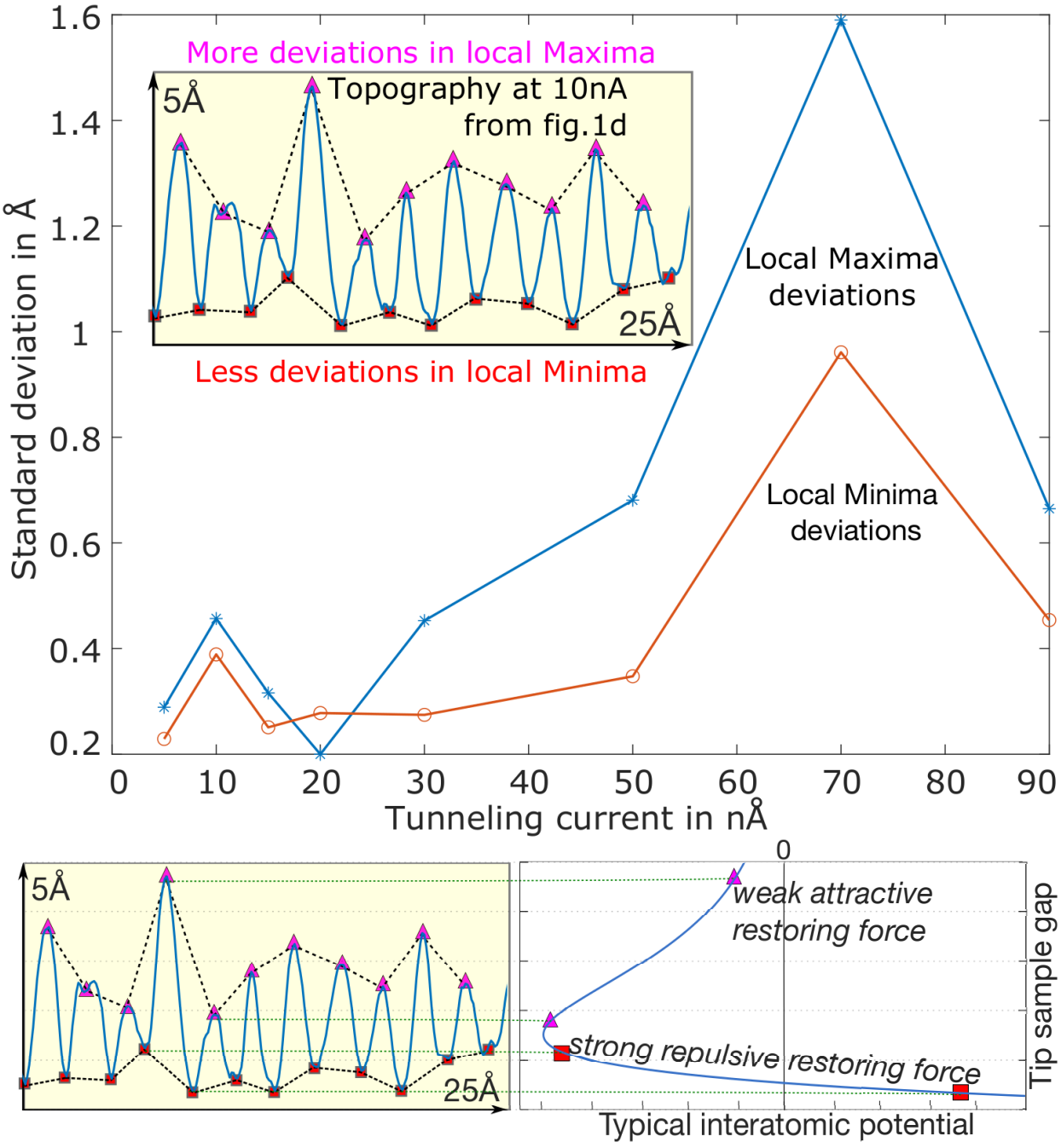

Figure 3.8: Standard deviation of local maximas and minimas of graphite atomic topographies in figure 3.8. Inset shows a portion of atomic topography at nA from fig 3.8 to exhibit the local minimas have lesser deviations than local maximas.

It has been shown in ref [3] that the corrugated atomic topographies at higher currents have more pronounced and regular local minimas than local maximas. To analyze and clarify this subtle difference in our measured topography curves in figure 3.2, a data set of all local maxima has been extracted from atomic topographies at different Itip. To study the variations in local maximas, standard deviation (SD) is calculated for each data set of local maximas at different Itip. Similarly, SD of local minimas are also calculated from atomic topographies at different Itip and graphed for comparison in figure 3.8.

Figure 3.8 shows SD for local maximas and local minimas as a function of Itip. Since the atomic corrugations amplify with increasing Itip, the standard deviations of both local maximas and minimas amplify too. Irrespective of Itip, local maximas have higher SD or more irregularity compared to local minimas. Such is the nature of the local deformations that the inward deformations have lesser SD (or less variations) when compared to outward deformation. This could be possible because the space below the surface is rigid but the space above the surface is free. The restoring force then becomes stronger for deformations into the bulk than into the air. This difference can also be seen from differences in the slope of interatomic potential energy curves corresponding to attractive or repulsive tip-sample interactions. The plot in figure 3.8 shows that upon closer approach to the surface, the tip is in the regime of the inter-atomic potentials. The repulsive atomic potential will be necessarily stronger upon close approach.

3.5 Summary

In summary, the weak tip-surface forces enhanced at small separations can be used to warp and probe the related elastic and electronic interactions in elemental and compound 2D material

systems. The corrugations of the atoms and atomic planes observed in the probing were rationalized as due to the tip-induced modulation of surface interatomic potential[7] and partly by high electric fields pulling the surfaces out of plane to maintain a constant current.

Chapter 3, in part is currently being prepared for submission for publication of the material, under the title "Atomic scale strain engineering of layered sheets on the surfaces of two-dimensional materials" by Sarkar, Nirjhar; Bandaru, Prabhakar R. and Dynes, Robert C.. The dissertation author was the primary investigator and author of this paper.

Chapter 4

Zigzag Grain Boundary

Grain boundaries have been viewed among the materials community as disordered one dimensional nano-structures that are sources of inelastic scattering transport electrically and thermally. Initial theoretical studies [19] have predicted the possibility of dispersion less electron transport across the grain boundaries if it is composed of a periodic array of dislocations. Their electronic character like metallicity would depend strongly on the topological arrangement of atoms similar to carbon nanotubes. In this paper we discuss the most common grain boundary found on graphite or graphene surface by Scanning Tunneling Microscopy(STM) studies.

4.1 Imaging grain boundaries

Grain boundaries on a hexagonal sheet of graphene or graphite have been shown clearly by TEM to be made up of pentagon-heptagon pairs in a zigzag arrangement with atomic resolution but the local electronic character of the GB can only be probed with STM. However STM imaging on such GB has been a major challenge because of the presence of site dependent and voltage

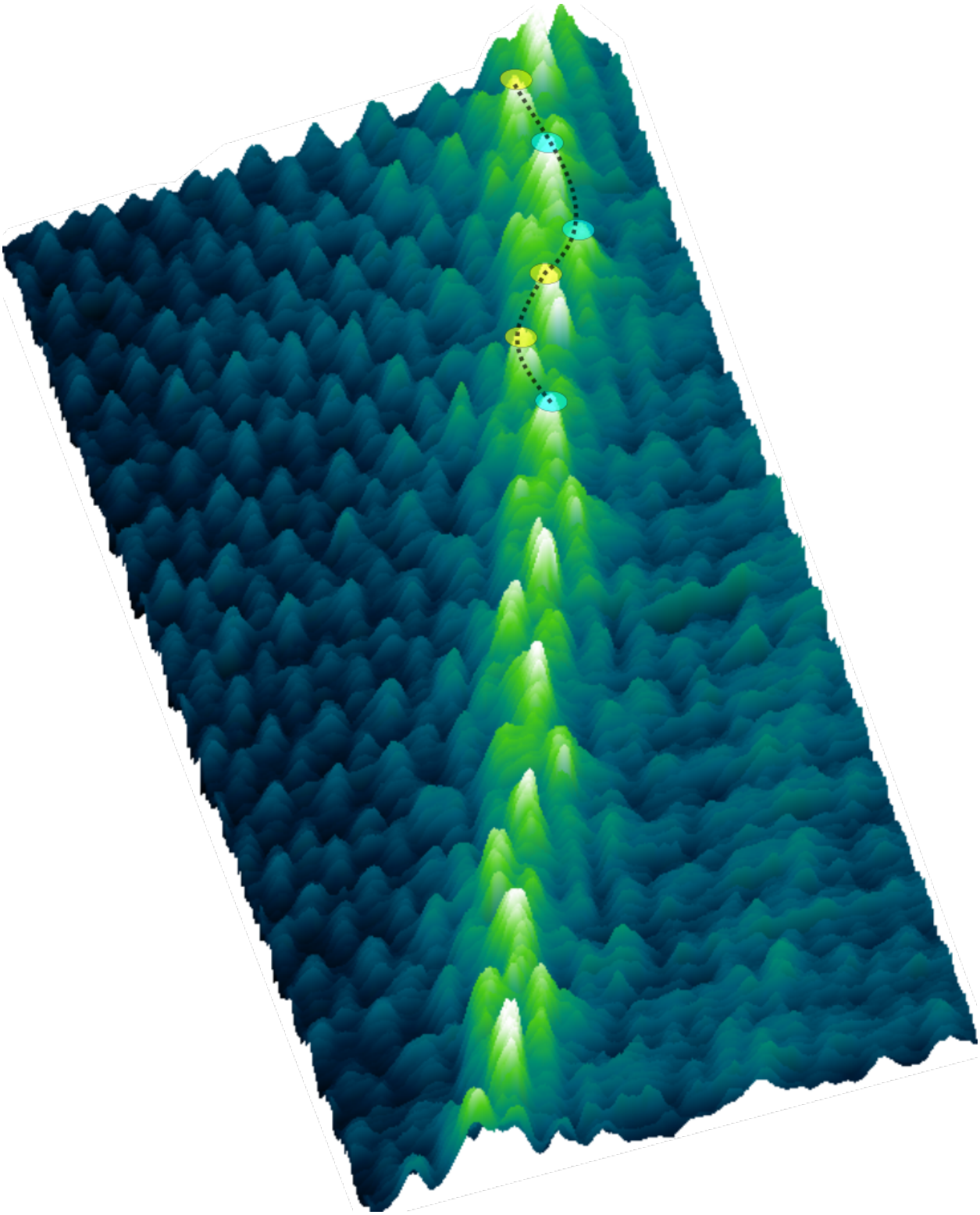

Figure 4.1: 3D image of a zigzag grain boundary

dependent dense localized states that mask the atomic resolution. Substrate doping and point defects further add complications to this challenge. Various STM studies on these grain boundaries have relied upon local density of states calculations to map out the localized states on the grain boundary sites in the experimental imaging. One of the calculated LDoS mapping of localized states on the zigzag grain boundary consistently calculated in [19] has been shown in figure 4.2. One can compare the zigzag pattern of localized states on both experimental topography (in figure 4.2a) with calculated LDoS (in figure 4.2c). Such 1D periodic grain boundaries have other unique distinct features like periodicity of 8.9 nm and rotation angle of 32.2 degrees for the case of zigzag GB shown experimentally in figure 4.2a and schematically in figure 4.2c. The rotation angle of the grain boundary is defined by θL and θR, which are the angles between the grain's crystallography (left and right respectively) and normal to the boundary. Similar to CNTs, zigzag grain boundary nomenclature of (3,1)/(1,3) is the minimum number of unit cells traversed in crystallographic directions along every periodic unit along GB.

Another approach towards understanding the localization of states on the grain boundary is by edge states. Previous experimentally verified[19] theoretical studies have shown the existence of denser localized states on zigzag edges than armchair edges as schematized in figure 4.2e. The edges contributing to the (1,3) GB can be revealed by de-stitching the GB from figure 4.2c to figure 4.2d. This exhibits that the left and right edges of every pentagon-heptagon pair is made up of alternating zigzag edges (with localized states) and armchair edges (with no localized states). On restitching the GB from figure 4.2d to figure 4.2c, the same zigzag pattern of localized states are obtained (that matches with LDoS simulated maps[19]). Grain boundaries have been viewed among the materials community as disordered one dimensional nano-structures that are sources of inelastic scattering transport electrically and thermally. Initial theoretical studies [19]

have predicted the possibility of dispersion less electron transport across the grain boundaries if it is composed of a periodic array of dislocations. Their electronic character like metallicity would depend strongly on the topological arrangement of atoms similar to CNTs. In this paper we discuss the most common grain boundary found on graphite or graphene surface by Scanning Tunneling Microscopy(STM) studies. Grain boundaries on a hexagonal sheet of graphene or graphite have been shown clearly by TEM to be made up of pentagon-heptagon pairs in a zigzag arrangement with atomic resolution but the local electronic character of the GB can only be probed with STM. However STM imaging on such GB has been a major challenge because of the presence of site dependent and voltage dependent dense localized states that mask the atomic resolution. Substrate doping and point defects further add complications to this challenge. Various STM studies on these grain boundaries have relied upon local density of states calculations to map out the localized states on the grain boundary sites in the experimental imaging. One of the calculated LDoS mapping of localized states on the zigzag grain boundary consistently calculated in [19] has been shown in figure 4.2c. One can compare the zigzag pattern of localized states on both experimental topography (in figure 4.2a-b) with calculated LDoS (in figure 4.2c). Such 1D periodic grain boundaries have other unique distinct features like periodicity of 8.9 nm and rotation angle of 32.2 degrees for the case of zigzag GB shown experimentally in figure 4.2a and schematically in figure 4.2c. The rotation angle of the grain boundary is defined by (θ)L and (θ)R, which are the angles between the grain's crystallography (left and right respectively) and normal to the boundary. Similar to CNTs, zigzag grain boundary nomenclature of (3,1)/(1,3) is the minimum number of unit cells traversed in crystallographic directions along every periodic unit along GB.

Another approach towards understanding the localization of states on the grain boundary is by edge states. Previous experimentally verified[19] theoretical studies have shown the existence

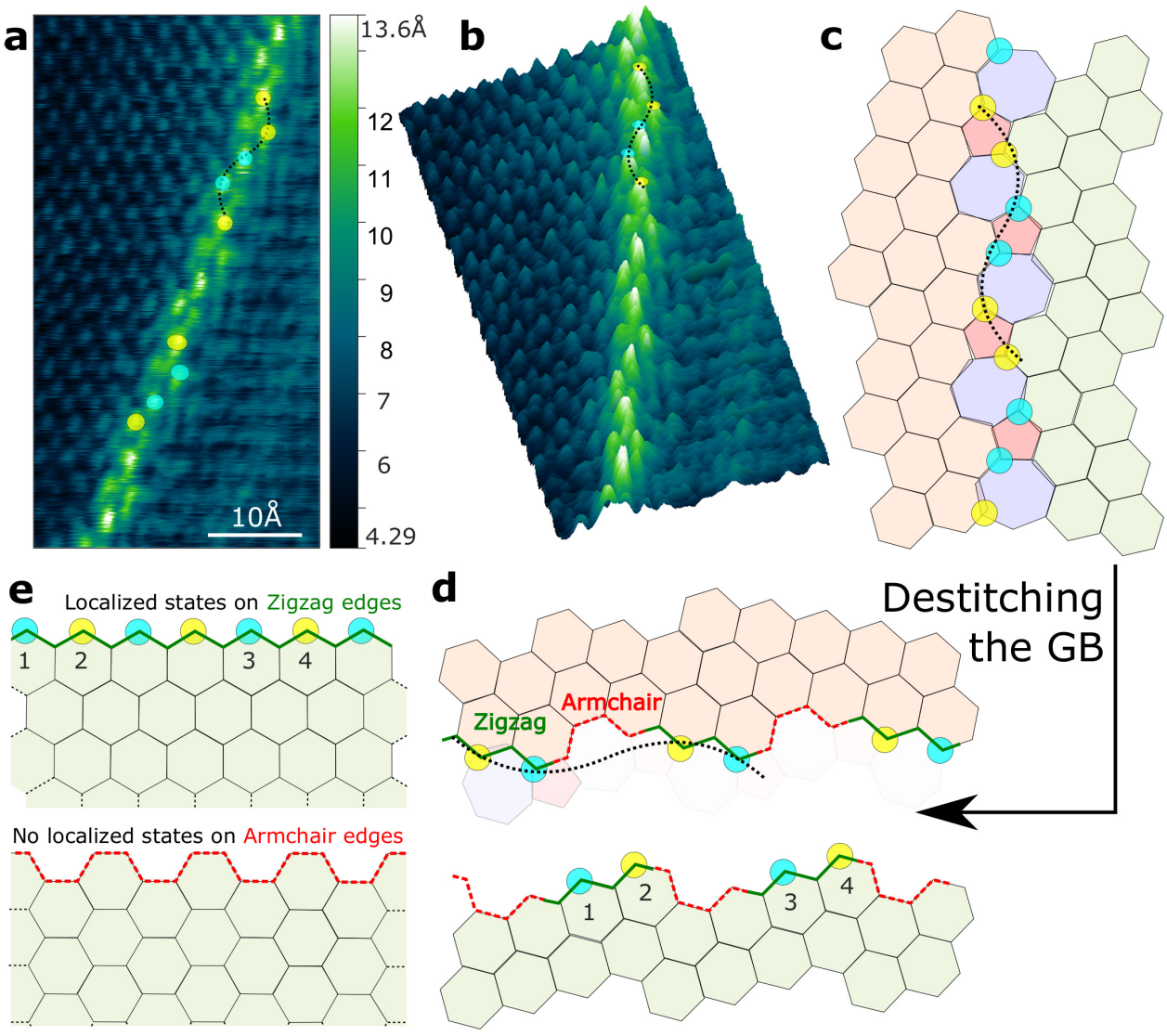

Figure 4.2: Zigzag grain boundary experimental STM image shows localized states due to zigzag edges

of denser localized states on zigzag edges than armchair edges as schematized in figure 4.2e. The edges contributing to the (1,3) GB can be revealed by de-stitching the GB from figure 4.2c to figure 4.2d. This exhibits that the left and right edges of every pentagon-heptagon pair is made up of alternating zigzag edges (with localized states) and armchair edges (with no localized states). On restitching the GB from figure 4.2d to figure 4.2c, the same zigzag pattern of localized states are obtained (that matches with LDoS simulated maps[19]).

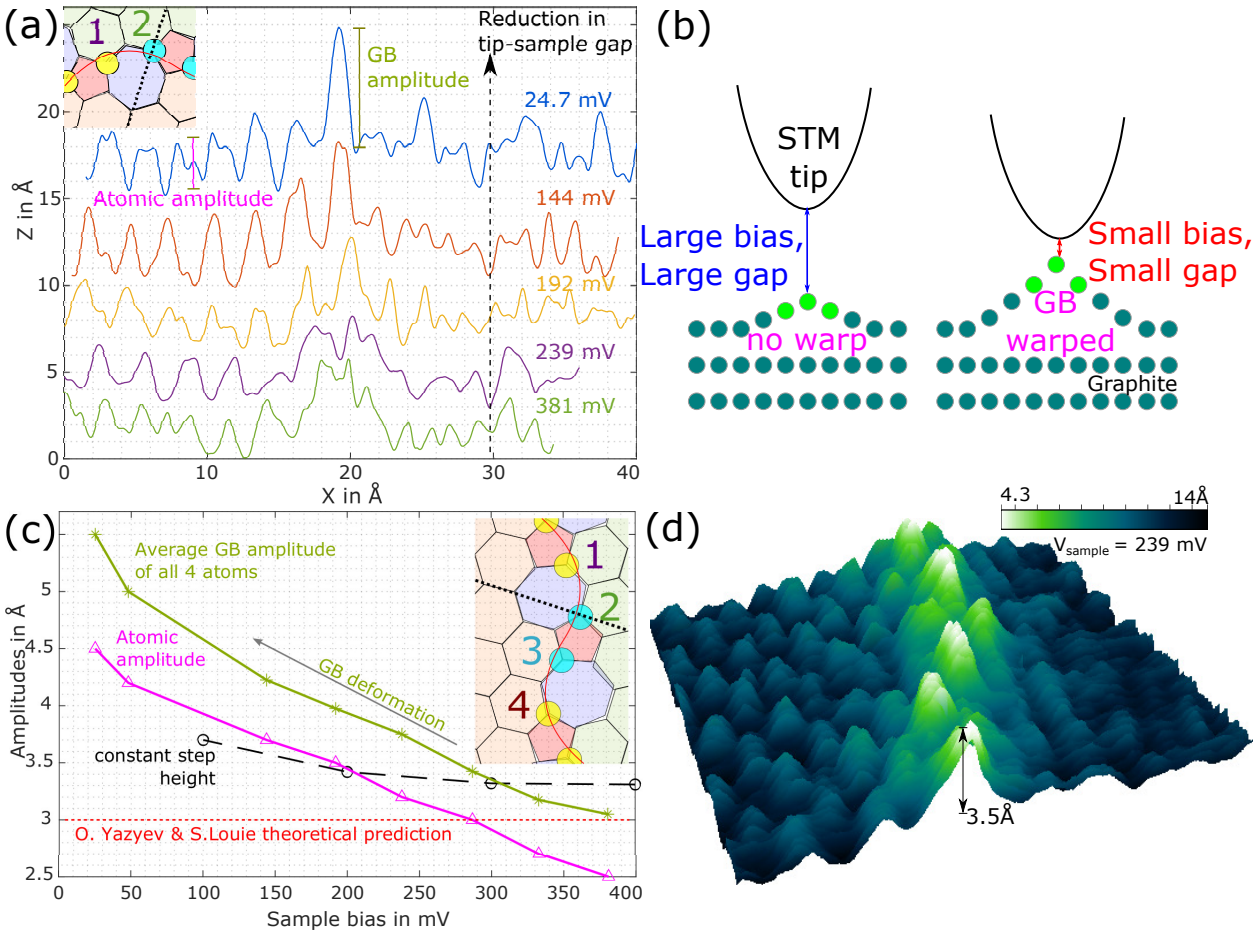

Figure 4.3: 2D and 3D topographic image of zigzag grain boundary with the schematic

4.2 Buckling

STM ability to probe localized states on the GB by topographic imaging can be a subtle art to deconstruct. Hence, the topography across the atom labeled 2 (in figure 4.3 inset) is compared as a function of sample biases in figure 4.3c that shows the grain boundary is elevated out of plane from the grains (known as 'buckling'). This buckling amount of all 4 atoms (shown in figure 4.3c inset) is measured in 4.4. The average buckling of the GB along with the grain's atomic amplitudes is plotted in figure 4.3c as a function of sample bias. The increase in amplitudes with reduction in

sample bias (or gap distance) is due to outward local deformation induced by the tip at small gaps as schematized in figure 4.3b. At higher biases or larger gaps from figure 4.3c, the tip induced forces become weaker and the GB amplitude approaches its intrinsic buckled amount of 3A as theoretically predicted by Yazyev and Louie.

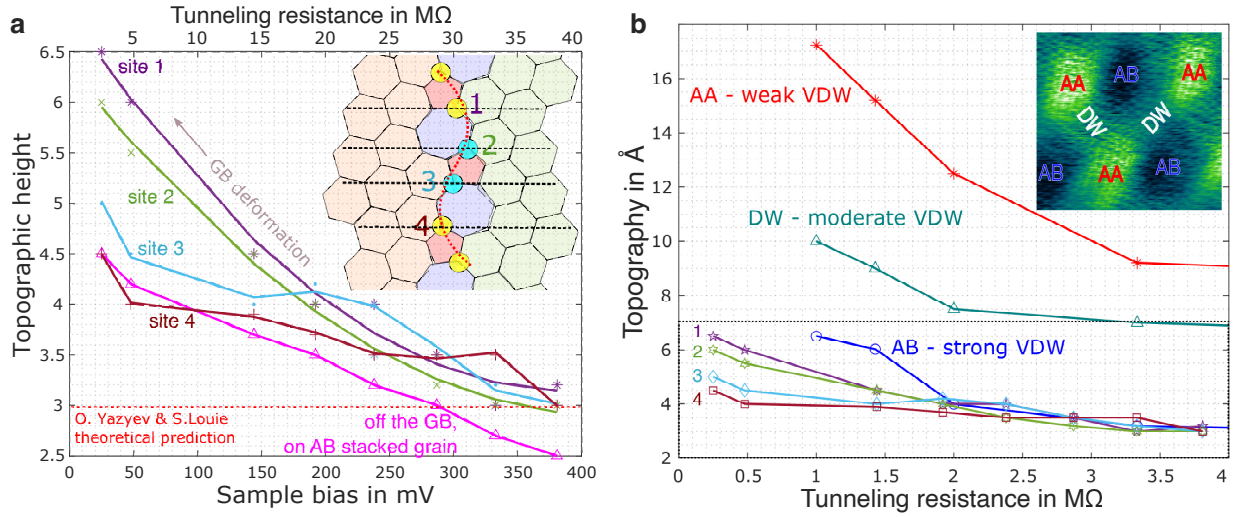

Figure 4.4: Sample Bias dependent topography across the GB. Topography across all 4 atoms has been averaged

Buckling in the third dimension is an efficient mechanism to relieve in-plane compressive elastic energy in exchange for bending energy [19]. Figure 4.2a or 4.3d exhibits a zigzag arrangement of distorted atoms which makes the grain boundary mechanically stable by minimizing the interaction between the dislocation dipoles [19]. The variation in response of all 4 atoms to tip-induced deformation (labeled in figure 4.3c inset) reveals its interlayer vDW strength.

The amount of buckling in these grain boundaries has been theoretically calculated and experimentally measured to be reaching 3A as shown in plot 4.3c and figure 4.3d. Topographies in figure 4.3a reveal that the grain boundary amplitudes and the atomic amplitudes are increasing with the decrease in sample bias (or tunneling gap reduction). These amplitudes have been plotted as a function of sample bias (or gap resistance) in figure 4.3b. GB amplitude remains consistent

around 3.5A above 240 mV. This suggests that the GB is intrinsically buckled as schematized in figure 4.3b. On further reduction in Vsample under 240mV (or gap reduction), the amplitude enhancement (of 4A from 3A to 7A) is caused by the local elastic deformation of the graphite surface by the tip at very small gaps as schematized in figure 4.3b. Deformation amplitudes of individual GB atoms have been shown in supplementary information 1. Our previous experimental studies about tip-induced local deformation of graphite features (like steps, moire domains, atomic topography, etc) has revealed their relative interlayer vDW bonding strength to its underlying layer. Using these results, it can be determined that the interlayer vDW bonding of (1,3)|(3,1) GB is as strong as AB stacked graphite.

4.3 Tunneling spectroscopy

Significant evidence has accumulated by now that the GBs strongly affect electrical transport and represent the limiting scattering mechanism of the electronic mobility. Less research is known on how the electronic and transport properties of GBs are modified at nonzero electron densities (i.e., away from the Dirac point). Indeed, due to filling of quasi-bound states residing on them by electrons from the bulk, the GBs transform into charged lines. Note that a local self-doping of individual GBs (i.e., transfer of electrons from the bulk to the states at GBs in a nominally neutral sample) has been recently observed by means of scanning tunneling microscopy (STM) measurements; it has also been argued that by doping by electrons from the bulk, the GBs can act as quasi-dimensional metallic wires.

4.3.1 Low bias peaks

The dI/dV curves and maps were acquired using a lock-in pre-amplifier, with a typical sinusoidal modulation of 5 mV (rms) at 6kHz. All the spectroscopy curves in figure 4.5 are done on the grain boundary and on the neighbouring hexagons. Spectroscopy on neighbouring hexagons reveal the presence of dual low bias peaks centered around 150 mV. These low bias peaks disappear on the grain boundary and also 1 nm off the grain boundary. Such peaks have also been reported in [27] and attributed to the phonon-mediated inelastic mechanism proposed by reference [27]. However, such mechanism described in Zhang et al comes out of indirect inference. My spectroscopy studies on graphene on mica substrate did not show the existence of such gapped feature in spectroscopy. A possible explanation for the occurrence of the low bias VHS peaks could be the same as the origin of low bias peaks on moire patterns. In a moire pattern, the dirac cones of the two twisted grains come closer at low angles to hybridize into a pair of flat bands around charge neutrality that looks similar to the low bias peaks in figure 3.4. However this explanation should imply that the VHS peaks should be strongest on the grain boundary which is not the case. Another possible explanation for the occurrence of low bias peaks on the neighbouring hexagons (and not on the GB) is the zero bias flat bands on zigzag edges. From figure 4.5, one can observe that every septagon-pentagon pair is made up of zigzag edge on one side and armchair edge on other side. Zigzag edges are the source of localized electronic states corresponding to the zero bias flat band. These zigzag edges contribute to the zero bias peak that we observe in figure 4.5.

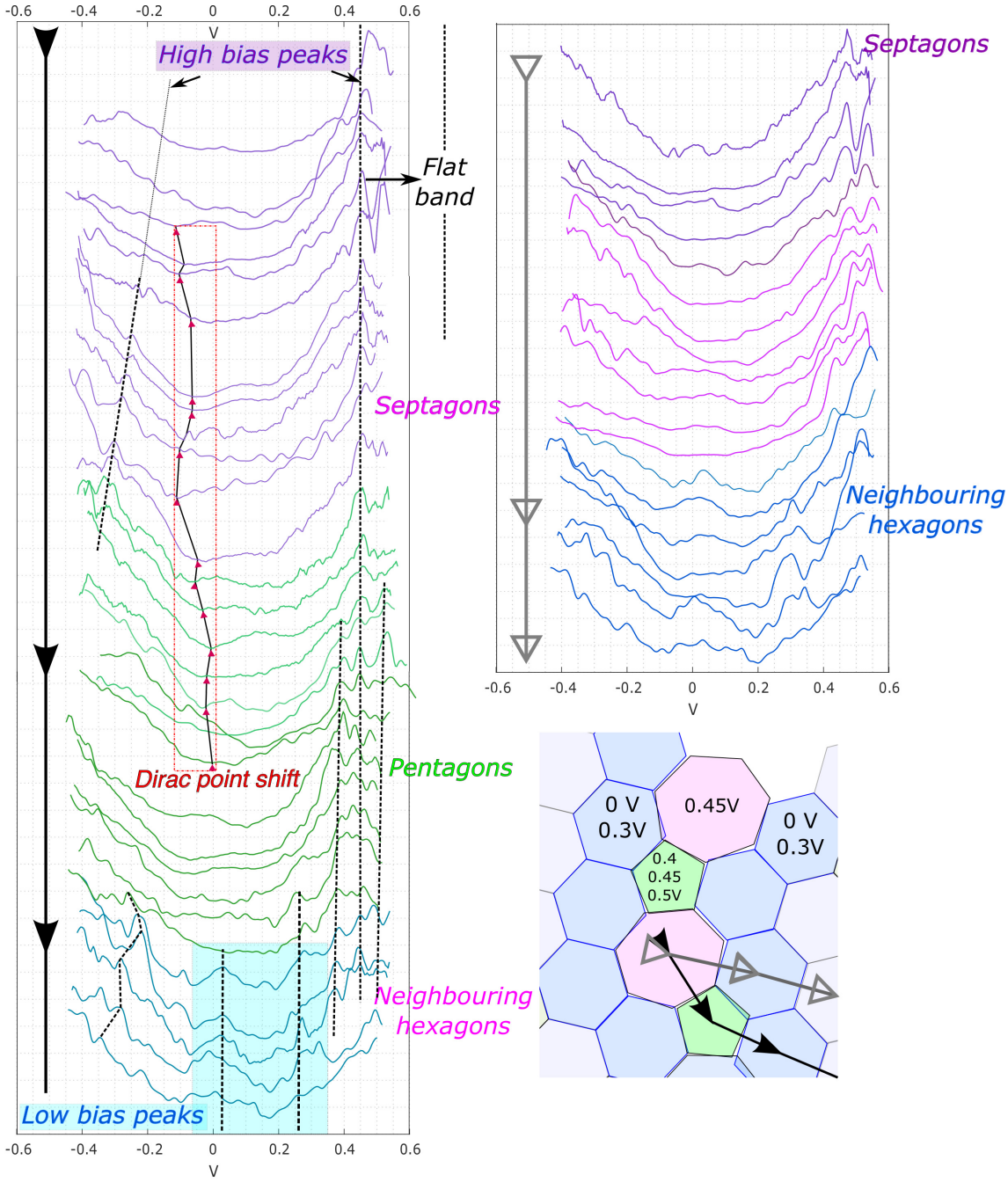

Figure 4.5: Local spectroscopy or LDoS on individual units of the periodic grain boundary: Pentagons and Septagons and also including the neighbouring hexagons

4.3.2 Dirac point

Ideally for a neutral sheet of graphene its dirac point should be on zero bias. However, experimental spectroscopy have shown the existence of dirac point on either positive or negative

side implying p-doping or n-doping behaviour of the graphene sheet. This could be substrate induced, adsorbent induced, gate voltage induced or defects induced as well. Presence of localized defects in 0D or 1D can cause intrinsic local charge transfer within the sheet of graphene. It has already been experimentally observed that wide non-periodic grain boundaries have higher conductance than the grains. This is brought into effect by self doping mechanism involved in the grain boundary. It has been theoretically predicted that the topological arrangement of the ordered grain boundaries can bring about localized periodic charge transfer depending on their topology.

Dirac point can be positioned by the finding the global minima of the spectroscopy curves. The presence of peaks in the curves often masks the accurate location of the dirac points. So the best spectroscopy curves to locate these dirac points would be the curves that have no peaks near the dirac point i.e. curves at the top of figure 4.5. All the dirac points have been pointed with small red triangle and put inside a red dotted box. Dirac point seems to be varying roughly from -120mV on septagons to -20mV on pentagons. This shows that the septagons are negatively charged with respect to pentagons. According to the position of the localized states in figure 4.2c, it is not clear where inside the pentagon or septagon all these spectroscopy have measured. Such an accuracy is difficult to achieve.

4.3.3 High bias peaks

High bias peaks here refer to the peaks around +/- 400mV. The existence of VHS have been theoretically or experimentally seen around the same bias voltages. These have been labeled as high bias peaks or flat bands on the top of figure 4.5. It can be noticed that the positive peaks are stronger than the negative peaks. A possible explanation for this can be explained by the gate

voltage dependent moire peaks. Positively charging the top moire layer with respect to its bottom causes stronger positive peaks and weaker negative peaks. Vice versa is observed on negatively biasing the top layer. Our spectroscopy reveals stronger positive peaks than negative peaks which suggests that the top layer of the graphite is positively charged. Such positive biasing of the top surface has been previously reported experimentally caused due to interaction with moisture or oxidizing atmosphere.

Higher the LDoS peaks, flatter the bands. Irrespective of pentagon or septagon, the flat band exists at all the locations on the grain boundary. These flat band correspond to localized states on the grain boundary in figure 4.6. When the sample bias is increased to 0.4V (where the flat band lies) all the localized regions on the grain boundary gets charged up and make the STM imaging of the zigzag grain boundary blurry as shown in figure 4.6. When the sample bias is reduced to voltages below the flat band regions @250mV, the STM imaging becomes clear and the zigzag pattern can be observed on the zigzag grain boundary as seen in figure in 4.6 and in figure 4.6.

These localized states act as channels of high density of electronic states waiting to be filled and they exist only at certain voltages that is distinct for a grain boundary with distinct topological arrangement. This opens up the possibility of other moderately high density of states that can also contribute to weak localization of states on the grain boundary. Such an evolution of distinct voltage dependent channels/states as a function of sample bias has been shown in figure 4.6

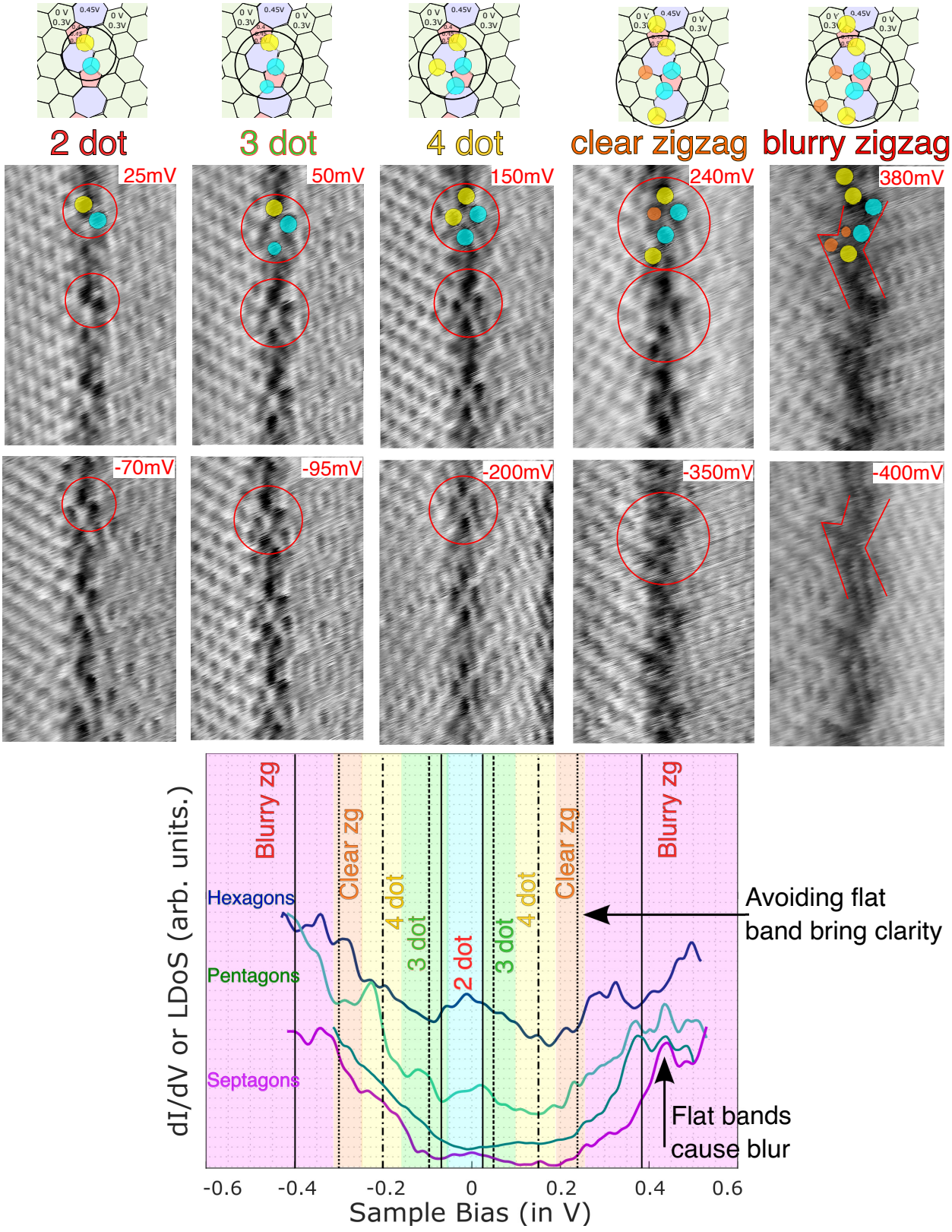

Figure 4.6: Voltage evolution of localized electronic states on grain boundary

4.3.4 Voltage dependence

Imaging with a tunneling microscope involves biasing a sample surface with respect to a virtually grounded tip that allow electrical tunneling of electrons between tip and surface. The tunneling electrons depart from /arrive to all the electronic states involved from zero till the sample bias. For instance, when the sample bias is at 400 mV, all the states from 400 mV to 0 mV on sample surface participate in the tunneling process that includes the flat bands and is responsible for making the STM imaging blurry on grain boundary. However, one can avoid these flat bands by reducing the sample bias from sample bias to 250 mV which no longer includes the flat band.

Figure 4.6 shows how the spatially dependent and voltage dependent localized states on the grain boundary getting charged up as a function of sample bias. The most clear distinction of the evolution of charged GB is observed between images at 25mV, 250 mV and 400 mV in figure 4.6. One can observe gradual discharging/disappearance of these localized states from 250 mV to 25 mV. The zigzag structure slowly disappears to a 4 dot, 3 dot and 1 dot structure.

This voltage evolution behaviour exists not only on the positive side of sample bias but also on the negative side. The gradual evolution of states appears to be symmetric around the dirac point (near zero bias) and transitions with increasing voltage (on both positive or negative side) to 3 dot, 4 dot, clear zigzag and blurry zigzag structure at +/- 400mV. Since the peaks are stronger or state localization are denser on the positive bias, clear changes in the images are observed on the positive biases than on the negative side.

4.4 Summary

The voltage evolution shows that the accessibility of localized states/channels allows attraction of electrons/holes on these local regions of the grain boundary. Such a process opens up the possibility of studying electron localization of defect states on the graphite surface and visually interpreting how can electron transport be affected by such a distinct topological arrangement of defects.

Chapter 4, in part is currently being prepared for submission for publication of the material, under the title “Coherent Zigazag Grain Boundary in graphite” by Sarkar, Nirjhar; Bandaru, Prabhakar R. and Dynes, Robert C.. The dissertation author was the primary investigator and author of this paper.

Chapter 5

Moiré

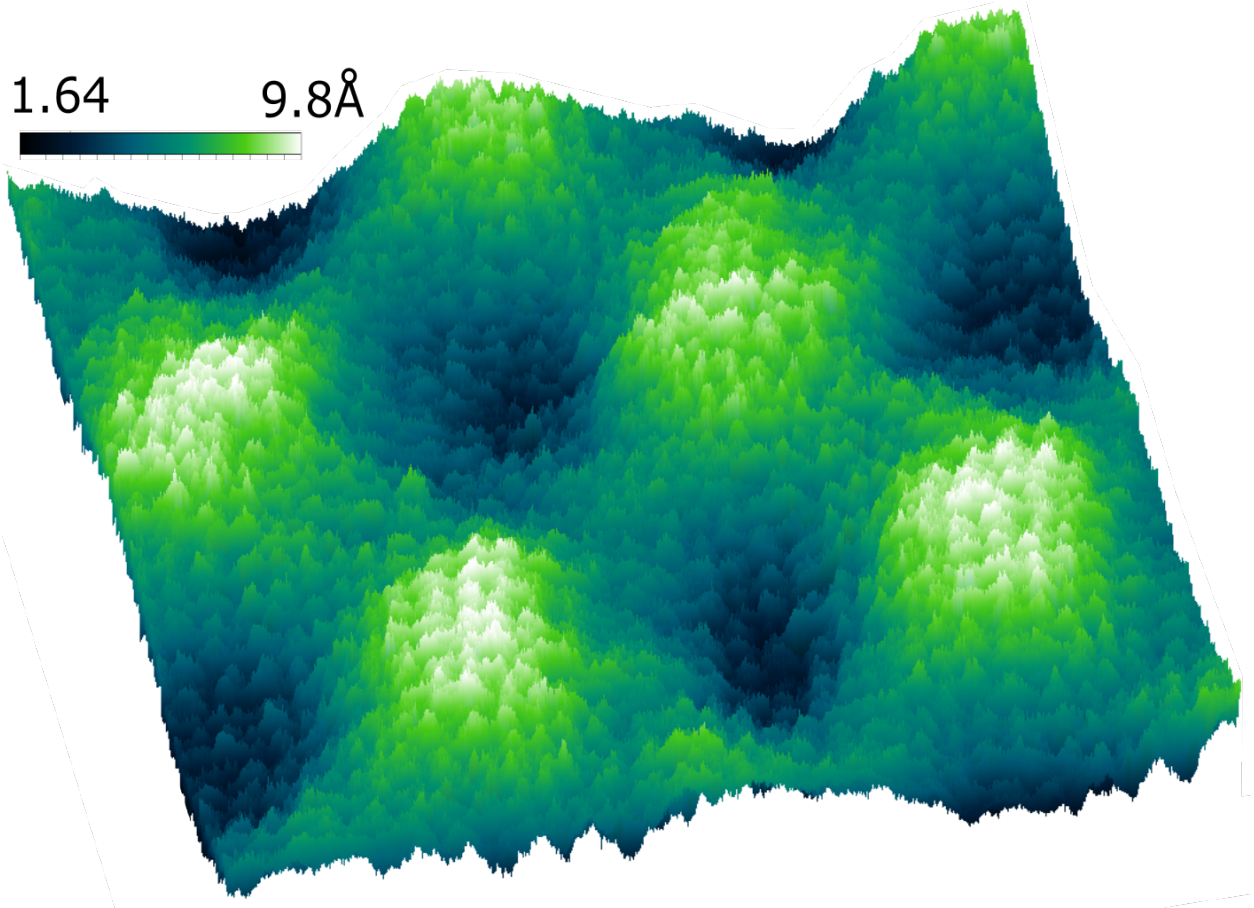

Figure 5.1: 3D image of 4.2^o twist angle moiré pattern

In this section we study how moire patterns commonly found on graphite surfaces respond to tip-induced deformations topographically in figure 5.2 and electronically in figure 5.3. Moire patterns are an ideal platform for this study because a twist of the top monolayer with the underlying graphite creates a periodic pattern of different domains with different inter-layer VDW or coupling strengths [28–30] giving rise to varying topography with different elastic and electronic properties. This makes moiré patterns suitable for testing our idea of interlayer VDW strength dictating the amplitude of local surface deformations and what impact it creates on their local electronic character. Figure 5.2 shows an example 4.2 degrees twist angle being subjected to imaging at varying tip-sample gaps by changing current conditions from 10 nA to 100 nA at fixed sample bias of 100mV. The topographies across the moiré domains are compared as a function of Itip as described in figure 5.2 caption.

AA stacking is the most unstable configuration with strong repulsion between hexagons of both twisted layers directly on top of each other and AB/BA stacking(or Bernal stacking) is the most stable configuration that has each top layer atom occupying the hollows of the lower layer hexagons or vice versa. DW look like bridges connecting all AA regions and act as boundaries between the dark AB/BA regions. DW have also gained unique interest in twistronics (because of their topological nature [31], soliton-like behavior [32] and polarizability [30]). The moire topography is expected to follow the interlayer potential [21–23].

The deformation amplitudes of different domains have been calculated from figure 5.2 plots and shown in figure 5.3a as a function of tunneling current and gap resistance. Figure 5.3a shows that with the reduction in tip-sample gap, AA regions get bulged out the most by 11A owing to its most unstable stacking whereas AB regions get deformed the least by 3A as it is the most stable stacking configuration in graphite [21–23]. DW or domain walls are transition lines or slip

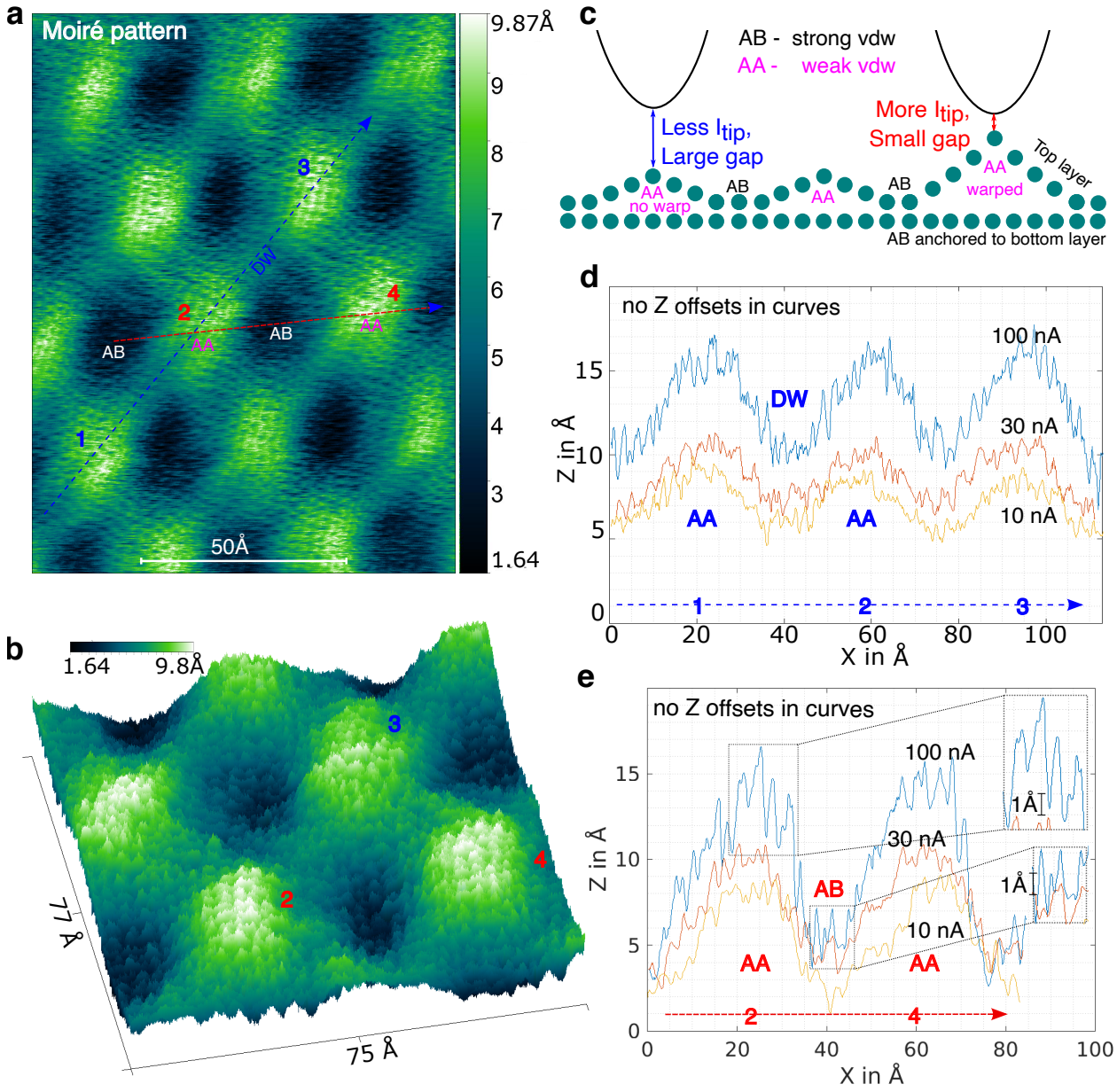

Figure 5.2: (a) and (b) 2D and 3D topographic image of a moiré pattern with a 4.2^o twist angle of the top layer with bottom. A pattern of bright (named 'AA') and dark bands (named 'AB') joined by bridges (named as 'DW') can be observed. The small dots across the moiré landscape correspond to individual atoms. All the numbered labels are on AA domains. A blue line is drawn along AA and DW. A red line is drawn across AA and AB. Topography at different currents is measured along the blue line (c) and red line (e). The three curves of (c) and (e) are not offset but are measurements and indicate surfaces being pulled out of plane. AA regions are deformed outwards the most and AB regions are more anchored to it's bottom layer whereas the DW show intermediate deformation schematized in (d) and calculated in fig 5.3a.

lines between AB/BA domains that show intermediate deformation. This shows how each domain with weaker interlayer VDW bond strength (based on their stacking) responds strongly to the tip-induced deformative forces. In other words, figure 5.3a reveals the relative strength of inter-layer VDW bonding of the moiré domains. Hence a topographic map of the moiré pattern (in figure 5.2a and b) can be imagined as a map of van der Waals strength.

Despite AA domains having the most unstable stacking configuration, their original topography remains intact at all currents. In Figure 5.2 plots, the spatial periodicity and amplitudes also remain intact. Figure 5.3a inset exhibits that the deformed AA regions at 100 nA have higher individual atomic amplitudes than less deformed AB regions. This indicates that the inter-atomic potential is different for deformed graphite surface (like AA) than less deformed graphite surfaces (like AB). In other words, a deformed graphite surface is less rigid than a non-deformed graphite surface.

To study the effect of tip induced deformations on the local electronic character of moiré domains, a low twist angle moire of 0.8 degrees is chosen because of the occurrences of flat bands near charge neutrality. Figure 5.3b shows a large peak around zero bias that corresponds to higher local density of states (also known as 'flat band'). Higher the LDoS, flatter the band. Spectroscopy measurements on AA domains at different tip-sample gaps (or gap resistances) in figure 5.3b reveals that peaks are getting sharper with gap reduction or the flat bands are becoming flatter with tip-induced local deformations (as shown by their full width half maximum, FWHM). The flattening and fattening of this band with gap distance is repeatable and exhibits a novel pathway for in-situ local tuning of flat band characteristics by tip-induced deformation.

The existence of the moiré peak ('flat band' in figure 5.3b) even after deformation indicates that the top layer has not decoupled or detached from its underlying layer. This suggests that

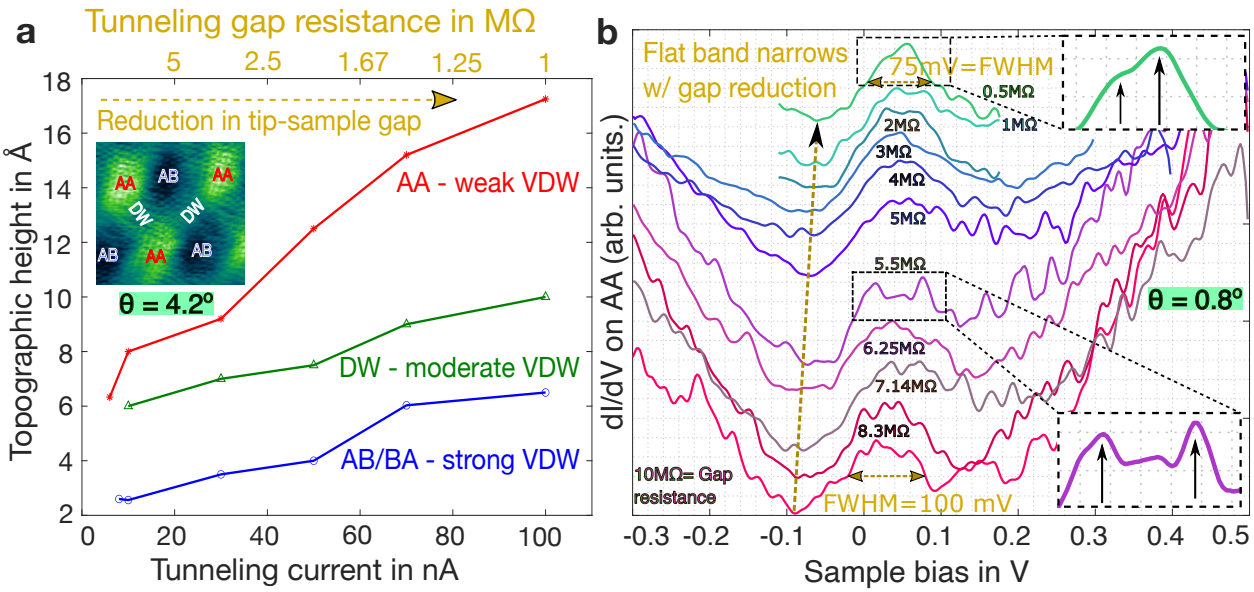

Figure 5.3: Topographic and electronic response of moire to tip-induced deformations. (a) Deformation amplitudes of moire domains calculated from figure 5.2 shows that the weakly VDW-bonded AA domains get deformed easily than AB that is strongly anchored to its underlying layer while DW shows intermediate response as a function of tunneling current or gap resistance(from 1M Ω to 10 M Ω). (b) dI/dV spectroscopy on AA domains of small 0.8^o twist angle shows how the flat bands corresponding to zero bias peak become narrower as shown by their full width half maximum(FWHM) with the reduction in gap distance or gap resistance (from 0.5MΩ to 10 MΩ). Measurements are described in supplementary info. 3). Flatter bands corresponding to higher density of states induce stronger correlation effects which could be desirable in twistronics.

several layers of graphite are being deformed to maintain the inter-layer coupling as schematized more appropriately in figure 3.7a,b than in figure 5.2c.

A widely believed earlier model[9, 14, 15] for atomic corrugation was a contamination-mediated process where there is possibly a layer of 'dirt' or oxide layer squeezed between the tip and surface acting as a compressible elastic spring. Dirt-mediated interaction would also imply that AA and AB domains deform by the same amount but we observe a different behavior in figure 5.3a. It is surprising that any atomically resolved images could be obtained with a dirty tip or surface. Also, dirt-mediated interaction would imply that tip-sample interaction with multi-layer graphite and single-layer graphene should be the same but we observe a contrasting behavior in

figure 3.3.

5.1 The Domain wall way

Domain walls are walls between two domains. For twisted bi-layer graphene the domain walls are between AB and BA. For twisted multi layer moire like moire on graphite surface, the domain walls are between Bernal (BAB) and Rhombohedral (CAB). These domain walls are being shown by white dotted lines in figure 5.4. They connect all the AA bright circular regions on the moire surface.

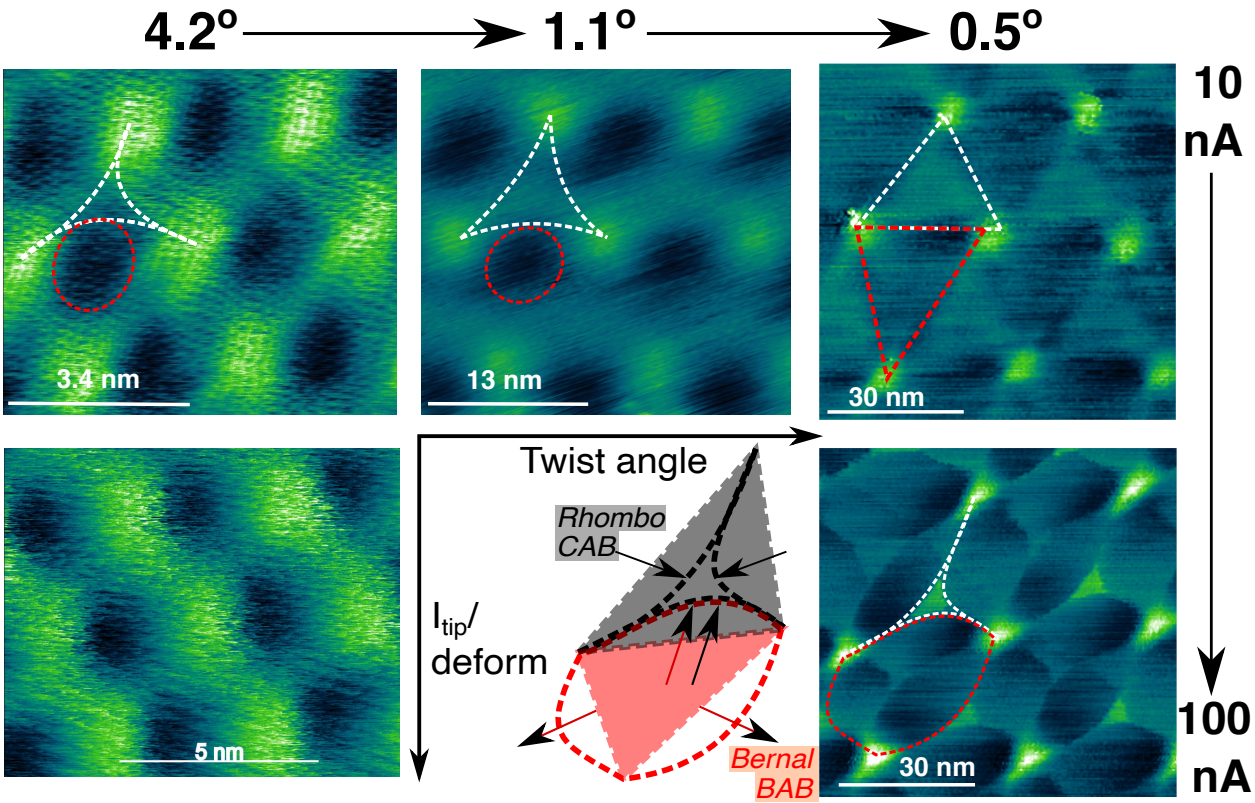

Figure 5.4: Competition between Bernal (BAB) and Rhombohedral (CAB) stacking on moire surfaces as a function of twist angle along x and tip-induced deformation/Itip along y axis. White dotted lines represent the domain walls

5.1.1 Along x axis

From figure 5.4 with the decrease in twist angle, the moire periodicity increases because of it's $1/\theta$ dependence. In other words, AA regions (connected by DWs) with the decrease in twist angle move outwards. Such outward stretch of DWs (connecting AAs) is accompanied by the stretching of the domain walls. This is shown by the change in the shape of dotted lines from a concave shape to a straight line.

5.1.2 Along y axis

With the increase in tunneling current, the tip gets closer to the surface. This brings forth outward deformation of the moire surface. The impact of such a deformation creates strain on the moire landscape. The moire surface responds to strain by configuring itself to a more stable configuration to release the strain. On moire, there is competition between 2 domains: Bernal (BAB - most stable) and Rhombohedral (CAB - less stable). AA domains are the most unstable regions. The domain walls are slip lines or transition lines between Bernal and Rhombohedral domains. These lines are elastic, interconnected via AAs and can float around on the surface [ref TEM]. With the strain, the domain walls are squeezed inwards thereby reducing the rhombohedral area and increasing the Bernal stacked area. On a 2D moire surface, Domain walls are the only 1D features confined that have attracted unique interest in their mechanical and electronic capabilities.

A detailed imaging analysis of the deformations above magic angle (at 4.2 degrees) in figure 5.5 and below magic angle (at 0.5 degrees) in figure 5.6 has been done.

Figure 5.5 shows that there is not much significant change to shape of moire surface in

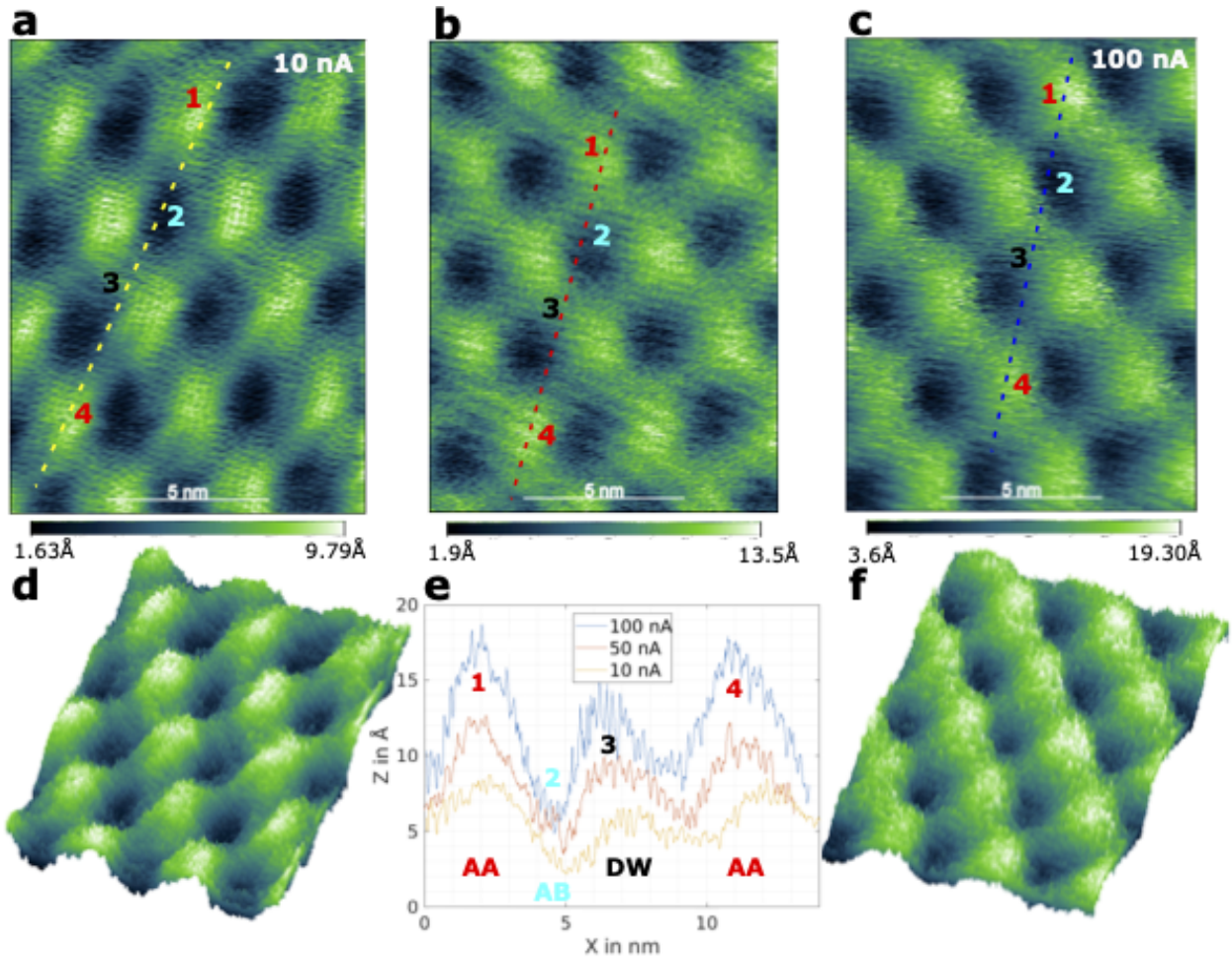

Figure 5.5: Deformation study by imaging and topography of moire angle 4.2 degrees as a function of tunneling currents or gap distances. Different moire domains are labeled in e.

terms of domain walls. The domain wall maintain their concave shape which could be their stable configuration even after deformation. Figure 5.6 shows that there is a significant change to shape of moire surface in terms of domain walls. The domain wall changes its concave shape (from figure 5.5) to straight lines in figure 5.6a and then under strain goes back to it's concave shape in figure (5.6b,c).

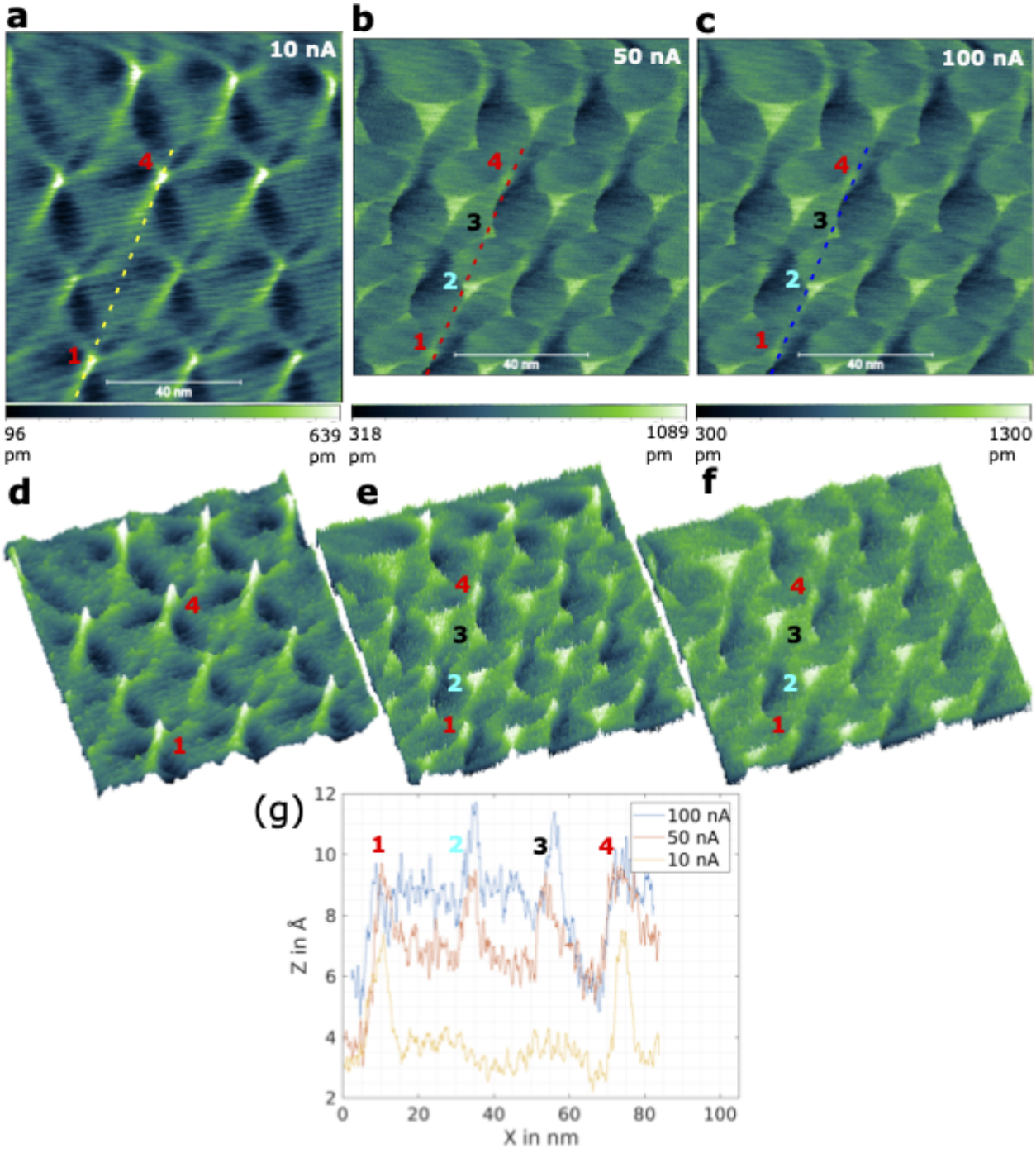

Figure 5.6: Deformation study by imaging and topography of moire angle 0.5 degrees as a function of tunneling currents or gap distances. Different moire domains are labeled in g.

5.2 Mercedes effect

Graphite is the only material known capable of forming moire patterns by itself. These are created during exfoliation on surface. The top layer during exfoliation sometimes is unable to

settle down to its nominal stacked order thereby forcing itself to twist on its underlying layer. The top layer could have the option of forming a wrinkle and correcting its twist angle but that does not happen. Moire patterns are formed on surface for microns of distances. It could be possible that the energy cost of forming a wrinkle is more than forming a moire pattern. In other words, moire patterns are one of low energy configuration with a stable structure. The process described above in moire formations would be affected by the presence point/line defects. This has been shown in figure 5.7a,b. A step edge becomes a pinning region to change twist angles of the moire and emanating multiple moire angles. Hence we observe slightly different twist angles that is sensitive to their moire periodicity.

Within the same scanning frame, the possibility of viewing several twist angles allows to observe the response of these moire patterns to the same tip-induced deformations. This has been shown in the bottom row of figure 5.7. A black dotted box on figure 5.7a has been expanded and put under strain to observe the pinching of the rhombohedral regions and expanding of the Bernal stacked regions as discussed in figure 5.7. One can observe the 'Mercedes' symbol on the rhombohedral domains but this happens only on low twist angles: 0.43, 0.61,0.77 and not on 1.33 degrees. This observation is being labeled by me as 'Mercedes' effect which happens only at low twist angles. The mercedes symbol is highlighted by the moire bumps (AA domains) joined by domain walls (DWs). The question remains whether the mercedes effects sees its onset from the magic angle 1.1 degrees.

It is also unclear as why we observe a mercedes symbol inside a bernal domain. Its origin might be electronic.

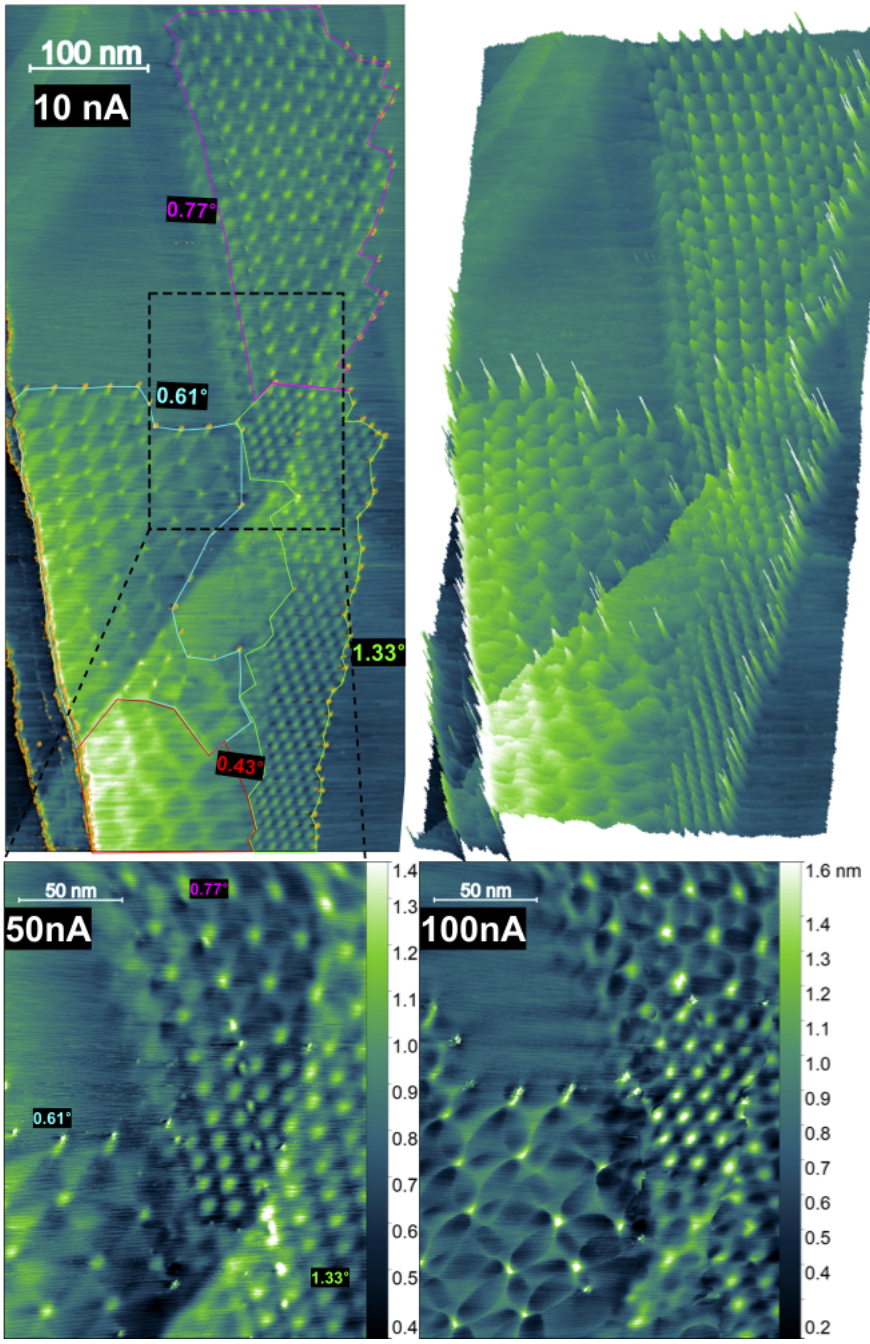

Figure 5.7: Existence of multiple angled moire patterns on line defects. These patterns change shape under tip-induced deformation.

5.3 Spectroscopy

Different moire domains are not only topographically different but also electronically different. Spectroscopy is done on graphite moire pattern of 1.1 degrees. This angle is referred to as

the magic angle because of the presence of flat bands all over the moire. However that's the case only in twisted bilayer graphene and does not seem to be the case in twisted multilayer graphite from our spectroscopy measurements in figure 5.8. The difference between graphene moire and

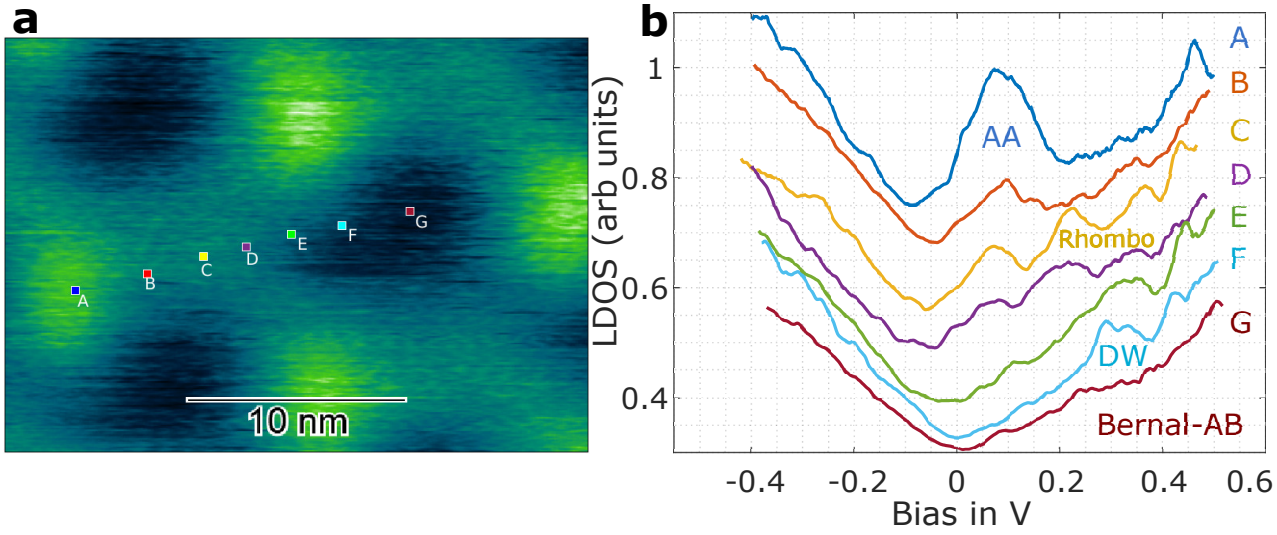

Figure 5.8: Spectroscopy of moire domains

graphite moire is that graphene moire has the alternating domains: AB and BA (apart from AAs) but graphite moire has the alternating domains: BAB (bernal) and CAB (rhombohedral). Moire surfaces are always under strain from their domain arrangement. Hence, they are looking for more possible low-energy configurations. Instead of bilayer, a trilayer or multilayer opens the possibility of having another metastable stacking configuration like rhombohedral. This changes their topographic/electronic behavior is contrast to twisted bi-layers for a given twist angle.

Ideally graphite with AB stacking or Bernal stacking have no peaks in their density of states which is what is expected and observed in spectroscopy of AB domains in figure 5.8 (at location 'G'). There is a flat band on AA domains shown by a zero bias peak (on location 'A') whose intensity get reduced as LDoS is measured away from the AA domains (on location 'B'). Spectroscopy

of the domains walls (at location F) has one strong peak at 0.3V. Spectroscopy locations on rhombohedral domains are labeled by 'C' and 'D'. They have remnant peak from AA domains at zero bias and remnant peak from domain walls at 0.4 V. Location C spectroscopy reveals a strong peak at 0.2V unique to this domain. Another way to imagine the spectroscopic transition on moire patterns is in terms of electronic bands traveling in k space getting flatter at local regions (like AA domains) and becoming not-so-flat at other domains.

5.4 Conclusion

Moire patterns are formed by an strain energy balance between two domains: Bernal and Rhombohedral. The balance tips its scale towards the competitor that has more stable configuration (i.e. Bernal) when the surface is strained by tip induced forces or change in twist angle. Tip-induced surface deformations add strain energy to this balance in a way that it acts in favor of Bernal. Hence, Bernal domains grow in size while the rhombohedral domains get shrinked inwards giving the shape of a Mercedes symbol. I call this 'Merecedes effect'.

Lets imagine the possibility of applying more strain to this surfaces to push it beyond the elastic limit. When moire strain is applied, the rhombohedral domains will shrink to a point that the whole twisted top layer will get detached/decoupled from its underlying layer and the moire pattern ceases to exist at this point. The three strained domain walls will shrink to a point that they will annihilate themselves as also shown in reference [30]. Until the point of such collapse, domain walls behave like stretchable elastic strings.

Chapter 6

Future work

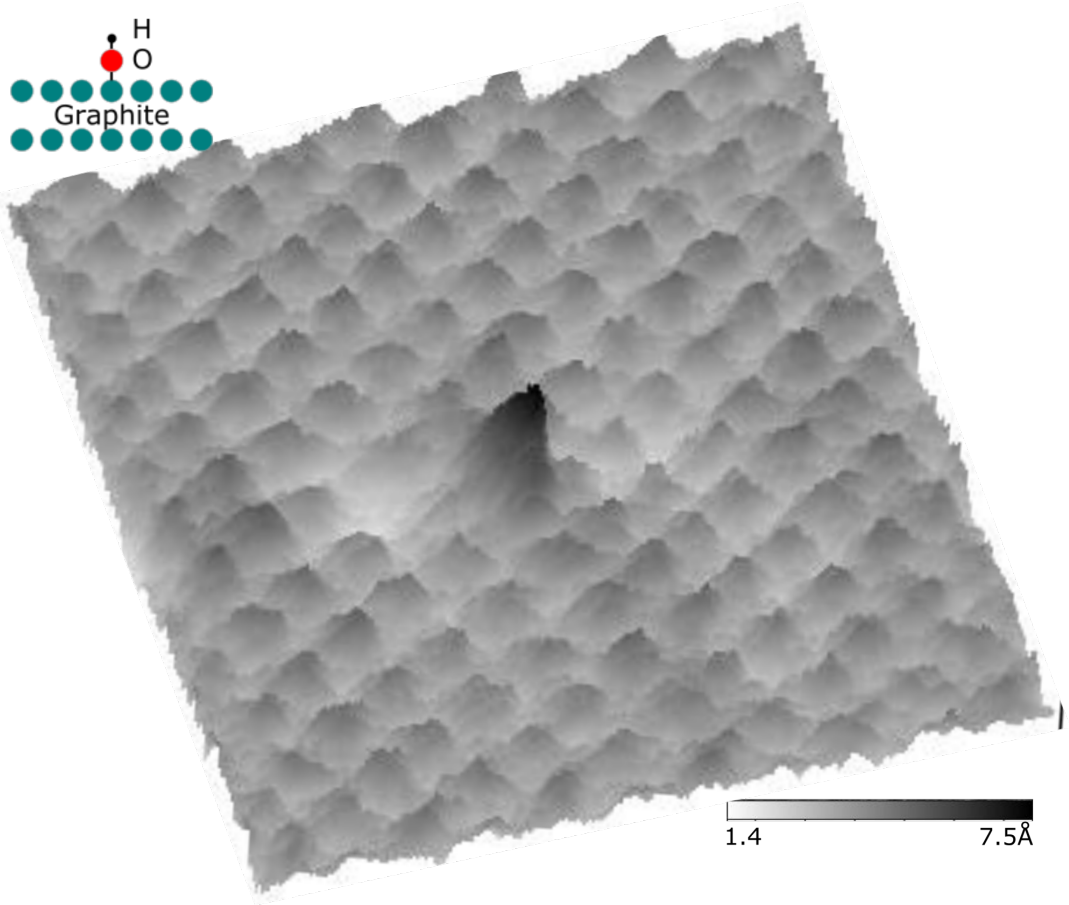

Figure 6.1: 3D image of a single hydroxyl ion

6.1 Single OH- ion manipulation

Surface adsorbed atoms or adatoms are weakly bonded to the surface and can be moved on the surface easily using an STM tip. Such efforts have been established before and is called as atomic manipulation. Don Eigler graduated from Physics, UC San Diego in STM related work and went to IBM where he wrote IBM using Xenon atoms on nickel surface. This put Don on the map in the world of atomic manipulations. Don, Crommie and Lutz later arranged 48 iron atoms on copper surface to exhibit the electronic wavefunction popularly known as Quantum corrals. These atomic manipulations were carefully done at low temperatures. Here, I showcase the capability of manipulating hydroxyl ions at room temperature. 3D and 2D plots of one hydroxyl ion on graphite surface in figure 6.1 and 6.2 that I imaged while the 300C hot graphite was cooling down in atmosphere and slowly absorbing moisture on the surface. The topographic height of the OH

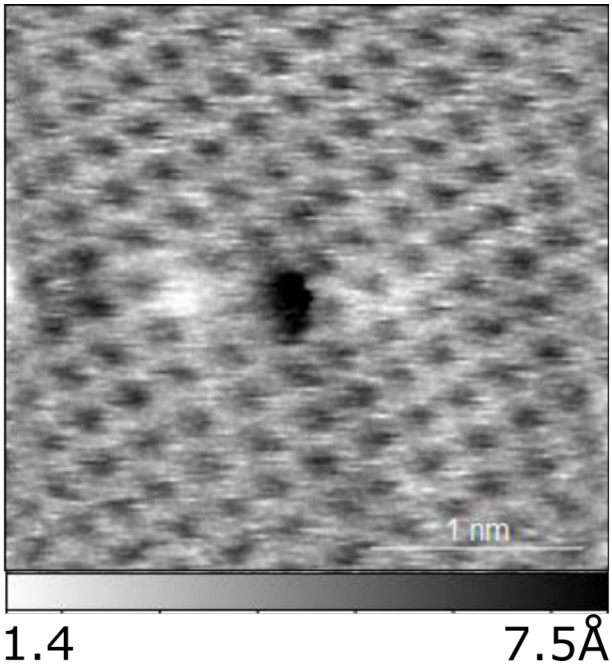

Figure 6.2: 2D image of a single hydroxyl ion

bond standing upright on the C surface looks close to reality. Multiple OH- ions were located while scanning a hot graphite surface. While imaging the graphite surface at small gap distances, one of the OH- ion moved to the bottom of the scanning area. Such atomic manipulation was done

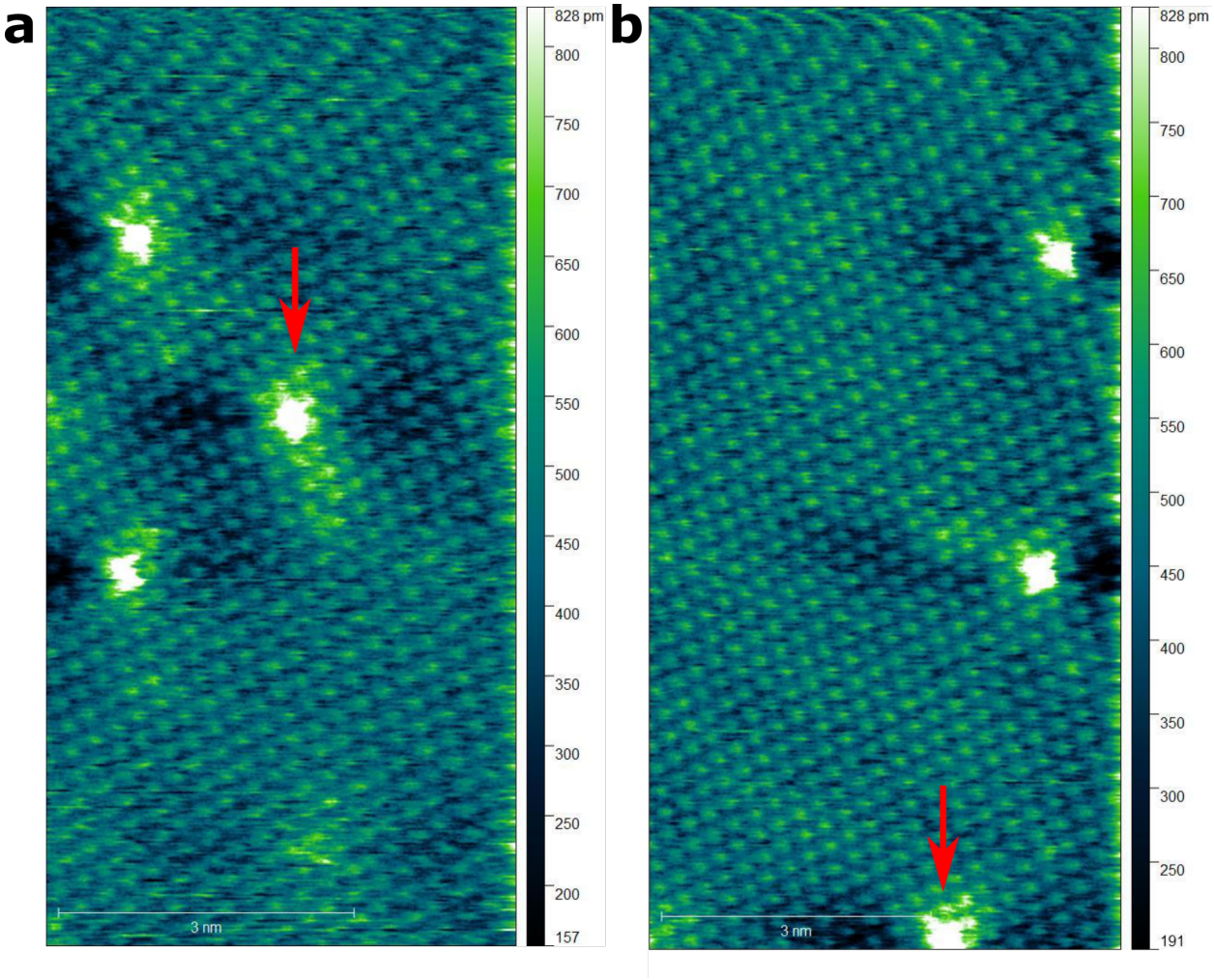

Figure 6.3: Atomic manipulation of OH- ions shown by red arrows on graphite surface

at room temperature and atmospheric pressure on graphite surface. Ideally, this is done at cold temperatures to ease the movement of adatoms with accuracy and less tip based interference. This shows the capability of graphite surface to hold adatoms and move them on the surface and this capability can be exploited to design interesting experiments with adatoms arrangement.

6.2 Flipping flakes

Graphite is made up of single-atom-thick carbon sheets stacked upon one another bonded by weak VDWs. Tip-induced local compression(a) and expansion(b) of graphite surface correspond to repulsive/attractive tip-surface interaction. Both deformations are opposed by shear forces (arrows) along basal planes. A graphite surface can be locally exfoliated in a systematic manner

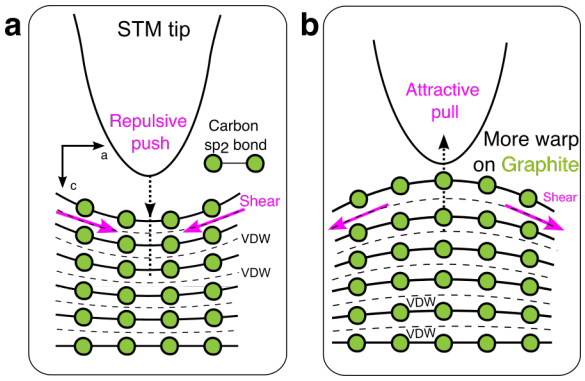

Figure 6.4: Compression and expansion with the tip induced forces on bonds and atoms

by applying an electrostatic force with a STM tip at the edge of a terrace. Point-like compression-expansion deformations can be induced by a vibrating STM tip when in contact with graphite. The periodically touched area becomes a point source for pressure waves which can propagate along the layer. For large and perfect layers, local deformations are damped at long distances. The pressure waves propagate in all directions with decreasing amplitudes until they have completely decayed. Such unperturbed waves have probably no destructive effect on the layers because the transmitted excitation energy spreads over a large region. However, when lattice discontinuities in form of steps or point defects are present, a wave can be scattered, interfering with other waves. Interference lines can form, where the amplitude of the wave is largely enhanced. This can lead

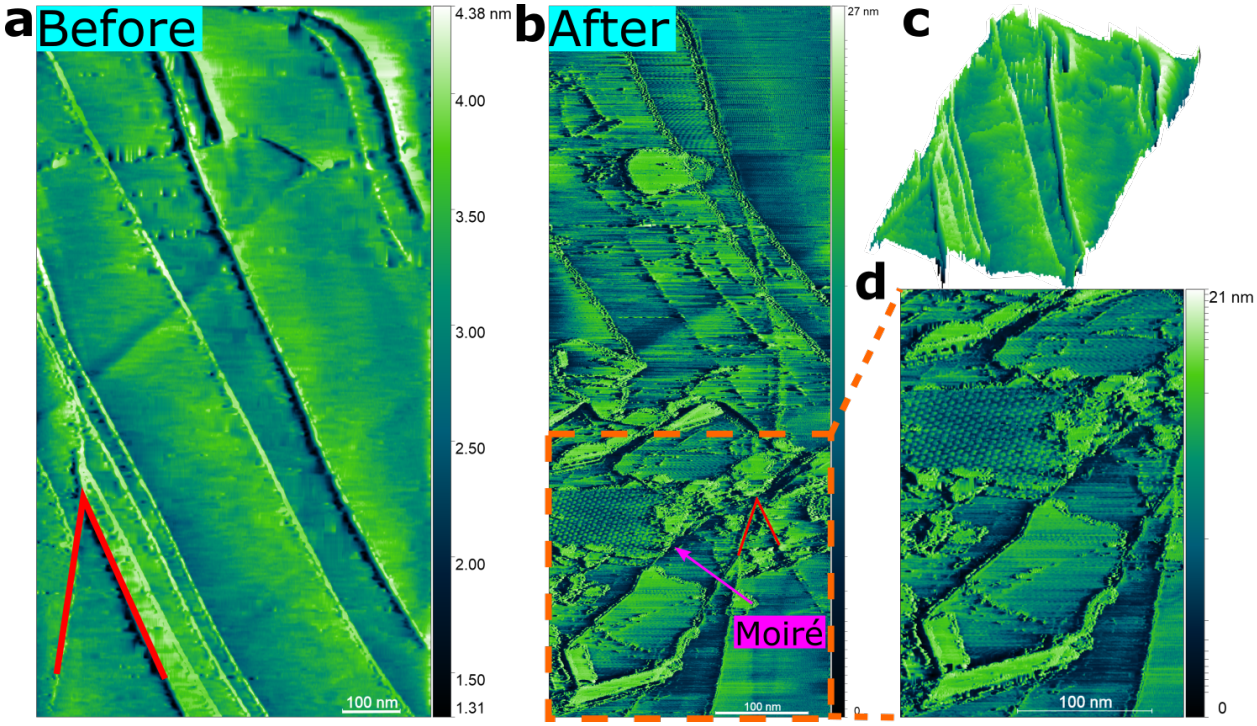

Figure 6.5: Modulating tip heights with high amplitudes obliterates the graphite surface by turning over several flakes around and creating a moire pattern.

to cuts of covalent bonds along the line of constructive interference. It facilitates the separation of the vibrating sheet from the support. Subsequently the oscillating sheet may flip over and fold, coming to lay in a new position

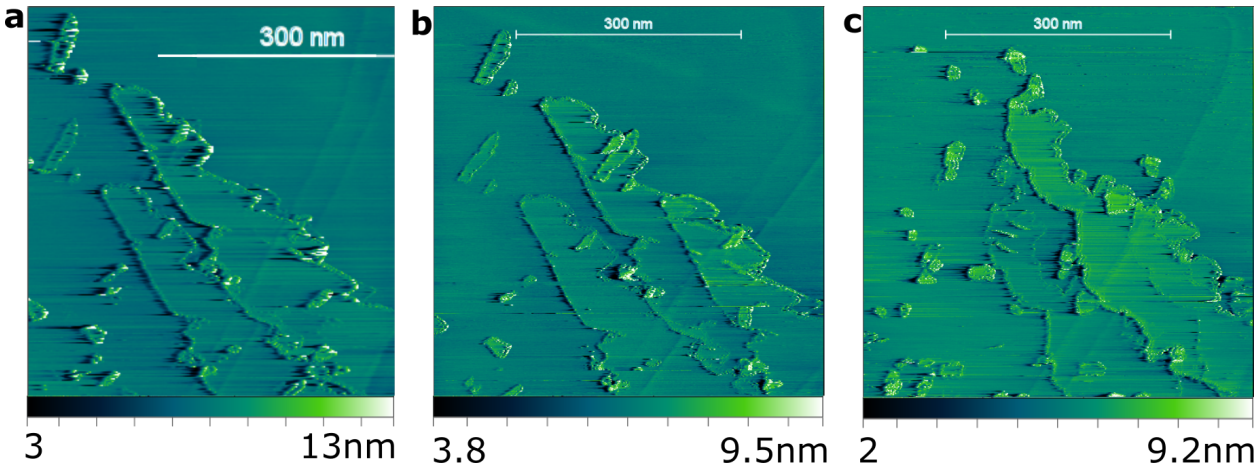

Figure 6.6: A failed attempt in trying to turn over a wide flake ending up in chipping its edges

The sequence of images shown in Fig. 6.5 were obtained from tip-induced events which occurred without our intent while taking STM images. This shows a failed attempt in trying to turn over a flake. It resulted in chipping the edge sites of graphite step heights. The flakes come off the step edges and settle either on the top of the step edge or get carried away by the tip to different locations.

6.3 Discovery of magnetism in GB

Here we report an experimental observation of magnetism in HOPG detected specifically at defect structures that are periodic and coherent. The measurements are done by wounding a current carrying copper foil around the tip. With a gaussmeter, an increase in magnetic field of 3 Gauss was measured with the current. On reversing the current direction, a decrease in magnetic field of 3 Gauss was measured on the edge of the Pt/Ir tip. In our experiments, we first found the grain boundary with the non-magnetized tip in figure 6.7. On turning on the current and consequential electromagnetism, the grain boundary responded to the magnetic fields. There could be some spin-filtering mechanism involved with the localized high density of electrons on the flat bands of the grain boundary. On reversing the currents, the image did not go back to the original condition implying that some hysteresis could be involved. The observed high temperature ferromagnetism in HOPG have been shown before but it has its possible origin in magnetic impurities. However the periodic coherent grain boundaries with no broken bonds would attract lesser metal impurities. Only zigzag edges are expected to give rise to the magnetic ordering due to the existence of the edge state. This has been observed theoretically and experimentally. This could be the possible origin of magentism in these GBs.

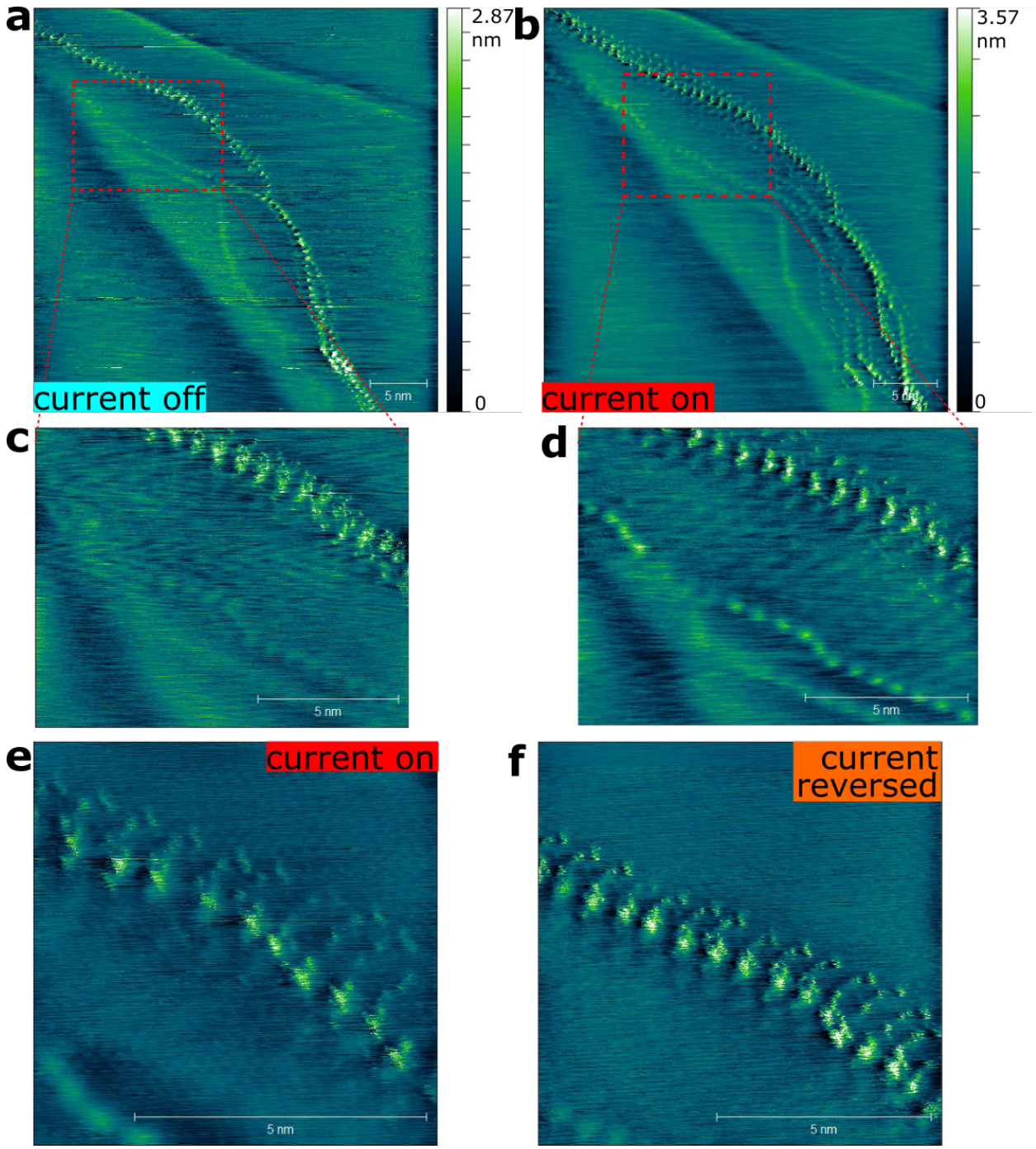

Figure 6.7: Magnetism in grain boundaries

Chapter 7

Conclusions

Weak interactions between tip and the surface have been exploited to drag adatoms on the surface to study electronic wave-functions but in this thesis we come up with a novel pathway to induce strain on the surface which is by removing the adatom and bringing the tip closer to the surface. The surface will get deformed less because the the forces involved are weak but that depends on the type of surface. 3D bulk rigid metals won't get deformed but the 2D materials get deformed relatively more. This has been proved by deforming surfaces of a single component 2D material (like graphite) and double component 2D material like $NbSe_2$.

This experiment showed that the tip-induced deformations depend on the strength of the vDW bonds in the underlying bulk. Many theories have been proposed on the enhance atomic topographies at smaller gaps including electronic states induced corrugation or dirt mediated interaction. Enhanced atomic topographies across monatomic step heights have revealed that the atomic corrugations only rely on elastic carbon bonds being compressed and expanded and not on open ended step edges. A step height is the difference between amplitudes on step up grain and step down grain. When both layer get corrugated, the step height remains constant nevertheless. Such

vDW theory gets further supported by deforming different moire domains having varying interlayer vDW strengths. This theory also resolves a long standing anomaly noticed by Soler-Rohrer on anomalous atomic corrugation on graphite.

This work offers to the straintronics and twistronics community, a new pathway of deforming individual atoms on surface controllably by tip-induced forces and probe in-situ the mechanical and electronic properties on surface under strain which can be exploited for innumerable applications.

We exhibit the observance of flat bands or Van Hove Singularities (VHS) on grain boundaries and moire hills (or AAs). Their origin lies from the zigzag edges that also exist on a edge of a step height. The flat bands correspond to high density of electronic states localized on the grain boundary. They must be avoided for good imaging and to avoid charging effects on any topological defect.

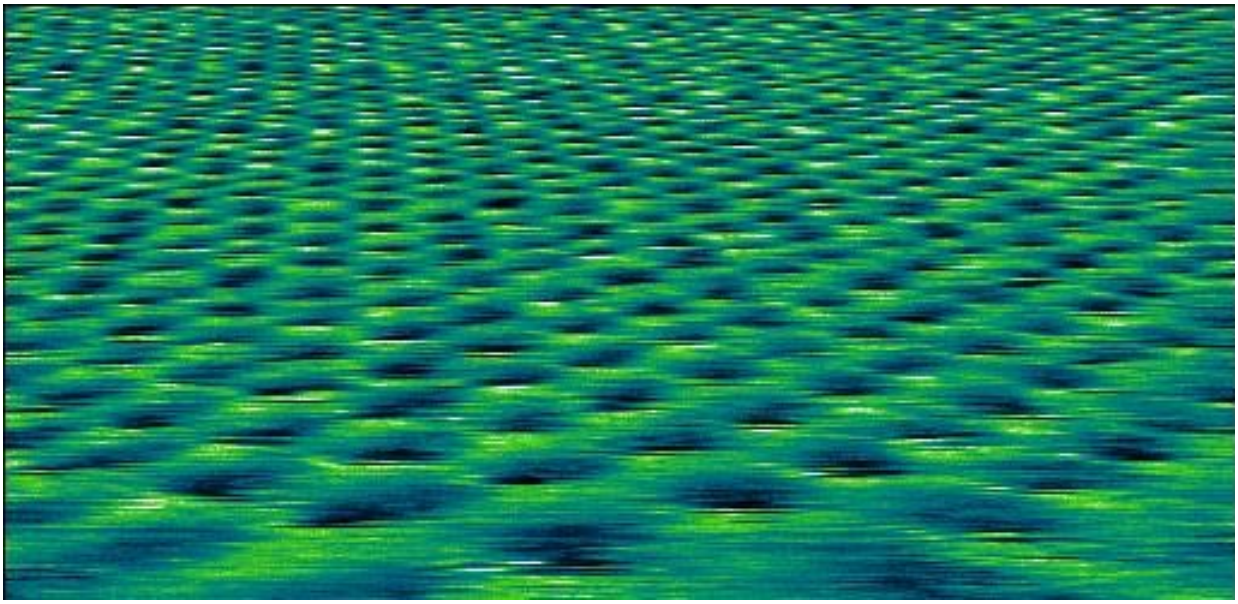

Figure 7.1: This is a 2D plot of graphite landscape in which the scan area was gradually reduced when the x raster scan frame reached from top to bottom to give a 3D effect. This image is one of a kind because the angle of graphite in the scan area has to be perfect.

References

[1]R. Tatar and S. Rabii, "Electronic properties of graphite: a unified theoretical study", Physical Review B **25**, 4126 (1982).

[2]I. P. Batra, N. Garcia, H. Rohrer, H. Salemink, E. Stoll, and S. Ciraci, "A study of graphite surface with stm and electronic structure calculations", Surface Science **181**, 126 (1987).

[3]F. Miao, S.-J. Liang, and B. Cheng, "Straintronics with van der waals materials", npj Quantum Materials **6**, 1 (2021).

[4]H. S. Wong, C. Durkan, and N. Chandrasekhar, "Tailoring the local interaction between graphene layers in graphite at the atomic scale and above using scanning tunneling microscopy", ACS nano **3**, 3455 (2009).

[5]J. C. Meyer, A. Geim, M. Katsnelson, K. Novoselov, D. Obergfell, S. Roth, C. Girit, and A. Zettl, "On the roughness of single-and bi-layer graphene membranes", Solid State Communications **143**, 101 (2007).

[6]R. Colton, S. Baker, R. Driscoll, M. Youngquist, J. Baldeschwieler, and W. Kaiser, "Imaging graphite in air by scanning tunneling microscopy: role of the tip", Journal of Vacuum Science & Technology A: Vacuum, Surfaces, and Films **6**, 349 (1988).

[7]J. Soler, A. Baro, N. Garcia, and H. Rohrer, "Interatomic forces in scanning tunneling microscopy: giant corrugations of the graphite surface", Physical review letters **57**, 444 (1986).

[8]G. Binnig, H. Fuchs, C. Gerber, H. Rohrer, E. Stoll, and E. Tosatti, "Energy-dependent state-density corrugation of a graphite surface as seen by scanning tunneling microscopy", EPL (Europhysics Letters) **1**, 31 (1986).

[9]H. J. Mamin, E. Ganz, D. W. Abraham, R. E. Thomson, and J. Clarke, "Contamination-mediated deformation of graphite by the scanning tunneling microscope", Physical Review B **34**, 9015 (1986).

[10]J. Tersoff, "Anomalous corrugations in scanning tunneling microscopy: imaging of individual states", in *Scanning tunneling microscopy* (Springer, 1986), pp. 176–179.

[11]J. Tersoff and D. R. Hamann, "Theory of the scanning tunneling microscope", Physical Review B **31**, 805 (1985).

[12]A. Selloni, P. Carnevali, E. Tosatti, and C. Chen, "Voltage-dependent scanning-tunneling microscopy of a crystal surface: graphite", in *Scanning tunneling microscopy* (Springer, 1985), pp. 168–171.

[13]E. Tekman and S. Ciraci, "Atomic theory of scanning tunneling microscopy", Physical Review B **40**, 10286 (1989).

[14]J. Pethica, "Comment on "interatomic forces in scanning tunneling microscopy: giant corrugations of the graphite surface"", Physical review letters **57**, 3235 (1986).

[15]S. Tang, J. Bokor, and R. Storz, "Direct force measurement in scanning tunneling microscopy", Applied physics letters **52**, 188 (1988).

[16]D. Smith, G. Binnig, and C. Quate, "Atomic point-contact imaging", Applied physics letters **49**, 1166 (1986).

[17]S. Ciraci and I. P. Batra, "Scanning-tunneling microscopy at small tip-to-surface distances", Physical Review B **36**, 6194 (1987).

[18]W. Jie, Z. Yang, F. Zhang, G. Bai, C. W. Leung, and J. Hao, "Observation of room-temperature magnetoresistance in monolayer mos2 by ferromagnetic gating", ACS nano **11**, 6950 (2017).

[19]O. V. Yazyev and S. G. Louie, "Topological defects in graphene: dislocations and grain boundaries", Physical Review B **81**, 195420 (2010).

[20]M. Olsen, M. Hummelgård, and H. Olin, "Surface modifications by field induced diffusion", PLoS One **7**, e30106 (2012).

[21]L. Gong, R. J. Young, I. A. Kinloch, S. J. Haigh, J. H. Warner, J. A. Hinks, Z. Xu, L. Li, F. Ding, and I. Riaz, "Reversible loss of bernal stacking during the deformation of few-layer graphene in nanocomposites", Acs Nano **7**, 7287 (2013).

[22]M. Koshino and E. McCann, "Multilayer graphenes with mixed stacking structure: interplay of bernal and rhombohedral stacking", Physical Review B **87**, 045420 (2013).

[23]T. Latychevskaia, S.-K. Son, Y. Yang, D. Chancellor, M. Brown, S. Ozdemir, I. Madan, G. Berruto, F. Carbone, and A. Mishchenko, "Stacking transition in rhombohedral graphite", Frontiers of Physics **14**, 1 (2019).

[24]J. Shim, C. H. Lui, T. Y. Ko, Y.-J. Yu, P. Kim, T. F. Heinz, and S. Ryu, "Water-gated charge doping of graphene induced by mica substrates", Nano letters **12**, 648 (2012).

[25]P. Bampoulis, K. Sotthewes, M. H. Siekman, H. J. Zandvliet, and B. Poelsema, "Graphene visualizes the ion distribution on air-cleaved mica", Scientific reports **7**, 1 (2017).

[26]E. Snider, N. Dasenbrock-Gammon, R. McBride, M. Debessai, H. Vindana, K. Vencatasamy, K. V. Lawler, A. Salamat, and R. P. Dias, "Room-temperature superconductivity in a carbonaceous sulfur hydride", Nature **586**, 373 (2020).

[27]Y. Zhang, V. W. Brar, F. Wang, C. Girit, Y. Yayon, M. Panlasigui, A. Zettl, and M. F. Crommie, "Giant phonon-induced conductance in scanning tunnelling spectroscopy of gate-tunable graphene", Nature Physics **4**, 627 (2008).

[28]R. Bistritzer and A. H. MacDonald, "Moiré bands in twisted double-layer graphene", Proceedings of the National Academy of Sciences **108**, 12233 (2011).

[29]H.-Q. Song, Z. Liu, and D.-B. Zhang, "Interlayer vibration of twisted bilayer graphene: a first-principles study", Physics Letters A **383**, 2628 (2019).

[30]J. S. Alden, A. W. Tsen, P. Y. Huang, R. Hovden, L. Brown, J. Park, D. A. Muller, and P. L. McEuen, "Strain solitons and topological defects in bilayer graphene", Proceedings of the National Academy of Sciences **110**, 11256 (2013).

[31]S. Huang, K. Kim, D. K. Efimkin, T. Lovorn, T. Taniguchi, K. Watanabe, A. H. MacDonald, E. Tutuc, and B. J. LeRoy, "Topologically protected helical states in minimally twisted bilayer graphene", Physical review letters **121**, 037702 (2018).

[32]L. J. McGilly, A. Kerelsky, N. R. Finney, K. Shapovalov, E.-M. Shih, A. Ghiotto, Y. Zeng, S. L. Moore, W. Wu, and Y. Bai, "Visualization of moiré superlattices", Nature Nanotechnology **15**, 580 (2020).